Wavelets in processing of neurophysiological data related to ambiguous images perception

Chapter · January 2018

CITATIONS
0

READS
117

6 authors, including:

Alexander N Pisarchik
Universidad Politécnica de Madrid
242 PUBLICATIONS **2,719** CITATIONS
SEE PROFILE

Alexey Pavlov
Saratov State University
204 PUBLICATIONS **1,251** CITATIONS
SEE PROFILE

A. E. Hramov
Innopolis University
586 PUBLICATIONS **3,734** CITATIONS
SEE PROFILE

Vladimir Maksimenko
Innopolis University
95 PUBLICATIONS **463** CITATIONS
SEE PROFILE

THEORETICAL AND APPLIED MATHEMATICS

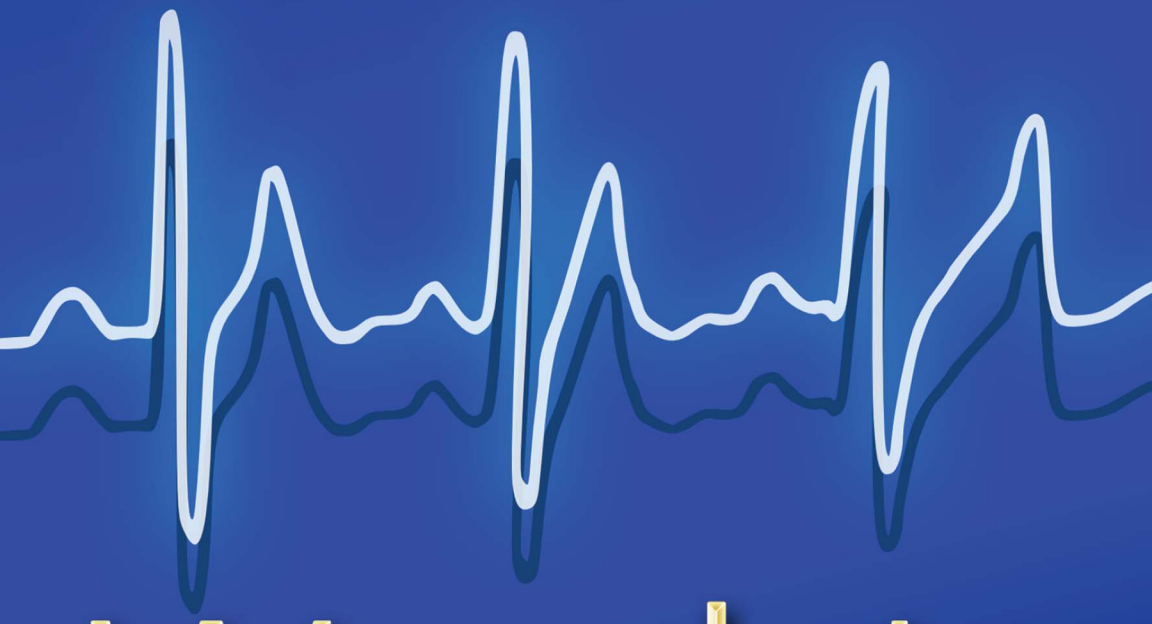

Wavelets

Principles, Analysis and Applications

Joseph Burgess
EDITOR

NOVA

THEORETICAL AND APPLIED MATHEMATICS

WAVELETS

PRINCIPLES, ANALYSIS AND APPLICATIONS

THEORETICAL AND APPLIED MATHEMATICS

Additional books in this series can be found on Nova's website under the Series tab.

Additional e-books in this series can be found on Nova's website under the e-book tab.

THEORETICAL AND APPLIED MATHEMATICS

WAVELETS

PRINCIPLES, ANALYSIS AND APPLICATIONS

JOSEPH BURGESS
EDITOR

nova
science publishers
New York

Library of Congress Cataloging-in-Publication Data

ISBN 978-1-53613-375-2 (eBook)

Published by Nova Science Publishers, Inc. †New York

CONTENTS

Preface		**vii**
Chapter 1	Wavelet Approach in Physics Education *S. Magazù and M. T. Caccamo*	**1**
Chapter 2	Int-HWT: Interval Extensions and Optimizations to Increase Performance and Accuracy of Haar Wavelet Transforms *Vinícius R. dos Santos, Renata H. S. Reiser, Maurício Pilla and Alice J. Kozakevicius*	**21**
Chapter 3	Wavelet Analysis as a Tool for Characterizing Trends in Climatic Data *F. Colombo, S. Magazù and M. T. Caccamo*	**55**
Chapter 4	Applications of Wavelet Analyses on Spectroscopic Experiments *M. T. Caccamo and S. Magazù*	**77**
Chapter 5	The "à trous" Transform with Wavelet Extrapolated Boundary Extensions for Data Analysis *Alice J. Kozakevicius and Alex A. Schmidt*	**91**

Chapter 6 Wavelets in Processing of Neurophysiological Data Related to Ambiguous Images Perception **125**
A. N. Pisarchik, A. N. Pavlov, A. E. Hramov, V. A. Maksimenko, A. E. Runnova and M. O. Zhuravlev

Index **147**

PREFACE

In this book, the authors report the results obtained by the application of wavelet analysis to two physics experiments: the motion of variable mass pendulum and the motion of variable length pendulum. These two motions, which furnish non stationary signals for their motions, are analyzed by means of a comparative Fourier Transform and Wavelet Transform. Afterwards, interval arithmetic extensions for the standard algorithms for the decimated and undecimated unidimensional Haar wavelet transform, as well as the standard and non-standard formulations for the two-dimensional HWT, are presented. In one chapter, wavelet analysis and other statistical tools are employed in order to analyse different aspects of Sicily temperature data. Sicily represents one of the hot spots for studying climate change in the Mediterranean area because of its vulnerability to desertification processes. The authors aim to highlight how wavelet transform can be employed to extract information from experimental results obtained by spectroscopic techniques, such as InfraRed, light and neutron scattering spectroscopies. In particular, this book shows how it is possible to characterize the registered spectral profiles by means of Wavelet Cross Correlation to evaluate spectra and the degree of similarity between images. Later, an iterative à trous coarsening algorithm combined with a wavelet extrapolation procedure is presented and analyzed to filter and identify the mean trend of simulated 1D data with non-trivial boundary conditions. Results show that the wavelet extrapolation based algorithm considered for the data-driven analysis is robust and reliable, allowing for an increased confidence region of the wavelet transform. In the concluding chapter, the authors aim to show that the wavelet transform has several advantages and benefits over classical methods of spectral analysis and other approaches.

Chapter 1 - It is well known that Mathematics and Physics are two distinguished disciplines that in the meantime are often strictly interconnected for teaching purposes. Mathematics furnishes useful tools for Physics and, on the other hand, Physics, together with its laboratory activities, can facilitate the clarification of Mathematics concepts, especially when they do not have a straightforward meaning. For this reason, in teaching wavelet analysis it is often advantageous to adopt an integrated mathematical and physical approach. The authors report the results obtained by the application of a wavelet analysis on two Physics experiments, i.e., the motion of a variable mass pendulum and the motion of a variable length pendulum. These two motions, which furnish non stationary signals, are analyzed by means of comparative Fourier Transform (FT) and Wavelet Transform (WT) approaches. Through these two laboratory experiments it is shown how, contrarily to FT that furnishes only an average frequency value for the non stationary signal, WT allows to get information on the time evolution of the frequencies content, i.e., it allows a joint time-frequency analysis.

Chapter 2 – This chapter presents interval arithmetic extensions for the standard algorithms for the decimated and undecimated unidimensional Haar wavelet transform (HWT), and the standard and non-standard formulations for the two-dimensional HWT. The proposed algebraic optimizations for the algorithms are derived specifically for the formulation of the HWT in the interval arithmetic context, being part of the already under development Int-HWT library, which is implemented using C-XSC library for interval arithmetic. This work is the first step to the development of the Int-DWTs library that will provide interval results for several Discrete Wavelet Transforms. The interval results show that the proposed formulations for the different standard algorithms for the HWT provide more exact values, with an increase of 20% in performance for the decimated HWT formulation. As an application, the interval optimizations for image filtering procedures based on the Hard and Soft thresholding of the wavelet coefficients are also presented, providing results more accurate than the standard algorithms with punctual values.

Chapter 3 - Wavelet transform is an effective mathematical tool able to provide a time–frequency representation of signals defined in the time domain. So far this innovative multiscale analysis has been successfully applied in various fields of science, such as, for example, geophysics, astrophysics, telecommunications and climatology. In this chapter the wavelet analysis is employed to analyse Sicily temperature data. Sicily represents one of the hot spot for the study of climate change in the Mediterranean area, because of its

vulnerability to desertification processes. Precipitations and temperature trends forecasted for the XXI century by Regional Climate Models (RCM) show an increasing temperature trend and a non-clear precipitation trend. To better characterize the temperature trend, the 1865-2016 temperature time series of Palermo and the 1962-2014 time series of four Sicilian localities have been analysed by means of Continue and Discrete Wavelet Transforms. Such analyses allow to identify the fast and slow events contained in the time series and to identify the major features of the Sicilian climate dynamics.

Chapter 4 - Wavelet transform is an innovative and powerful tool for analyzing complex data such as those obtained by spectroscopic techniques. In particular, it allows to locally resolve a non-stationary signal by means of functions called mother wavelets so producing a time-scale view of the signal. In addition, thanks to the wavelet multiscaling properties it is possible to get information both on a global and on a local view, to characterize transitory signal characteristics, trends, drifts, spectra abrupt changes and to perform signal denoising. The aim of this chapter is to highlight how wavelet transform can be effectively employed to extract precious information from experimental results obtained by spectroscopic techniques, such as InfraRed, light and neutron scattering spectroscopies.In particular, it will be shown how it is possible to characterize, following different approaches, the registered spectral profiles as well as, by means of Wavelet Cross Correlation, to evaluate spectra and images similarity degree.

Chapter 5 - An iterative *à trous* coarsening algorithm combined with a wavelet extrapolation procedure is presented and analyzed to filter and identify the mean trend of simulated 1D data with non-trivial boundary conditions. Results show that the wavelet extrapolation based algorithm considered for the data-driven analysis is robust and reliable, enabling the increase of the confidence region of the wavelet transform. Relative errors for the simulations were found to be in the order of 0.2% or less for each simulated 1D data set, independent of noise intensity, decomposition level or coarsest signal shape near data boundaries, confirming the contribution of the wavelet extrapolation to the non-linear analysis scheme. The intrinsic interpolatory property of the wavelet transform, combined with the *à trous* coarsening algorithm, also allowed the proposal of an automatic local curve approximation procedure for regions where strong localized influences are present and need to be removed in order to diminish distortions in the mean signal pattern. The proposed procedure avoids the necessity of model fitting for the regions to be treated. Numerical simulations for the analysis of noisy data are also presented and

discussed, highlighting the potential of the proposed scheme to be considered for a wide range of applications.

Chapter 6 - Noninvasive brain research is extensively used in modern neuroscience for studying human cognitive behavior and intellection mechanisms. One of the important technologies for recording brain dynamics is the electroencephalography (EEG). This method is very convenient for monitoring brain activity in a wide frequency range with a relatively high spatial resolution. The EEG data of psychophysiological experiments are usually processed for detecting characteristic patterns associated with various cognitive functions, as well as for other types of brain activity. In this chapter, the authors show that the wavelet transform has several advantages and benefits over classical methods of spectral analysis and other approaches. We demonstrates the success of wavelet processing on the example of psychophysiological data registered in the experiment with visual perception of ambiguous objects. Nowadays, ambiguous images are extensively explored for studying visual perception and decision making. However, despite high efforts of many researchers, the main mechanisms of image interpretation are not yet well understood. Although it is known that perception is a result of nonlinear processes in a distributed neural network of occipital, pariental and frontal regions of brain cortex, further detailed investigation of these processes is required.

In: Wavelets: Principles, Analysis and Applications ISBN: 978-1-53613-374-5
Editor: Joseph Burgess

Chapter 1

WAVELET APPROACH IN PHYSICS EDUCATION

S. Magazù [*] ***and M. T. Caccamo***
Dipartimento di Scienze Matematiche e Informatiche, Scienze Fisiche
e Scienze della Terra, Università di Messina, Messina, Italy
Istituto Nazionale di Alta Matematica "F. Severi" – INDAM,
Gruppo Nazionale per la Fisica Matematica – GNFM, Rome, Italy

Abstract

It is well known that Mathematics and Physics are two distinguished disciplines that in the meantime are often strictly interconnected for teaching purposes. Mathematics furnishes useful tools for Physics and, on the other hand, Physics, together with its laboratory activities, can facilitate the clarification of Mathematics concepts, especially when they do not have a straightforward meaning. For this reason, in teaching wavelet analysis it is often advantageous to adopt an integrated mathematical and physical approach. In this chapter, we report the results obtained by the application of a wavelet analysis on two Physics experiments, i.e., the motion of a variable mass pendulum and the motion of a variable length pendulum. These two motions, which furnish non stationary signals, are analyzed by means of comparative Fourier Transform (FT) and Wavelet Transform (WT) approaches. Through these two laboratory experiments it is shown how, contrarily to FT that furnishes only an average frequency value for the non

[*] Corresponding Author Email: smagazu@unime.it.

stationary signal, WT allows to get information on the time evolution of the frequencies content, i.e., it allows a joint time-frequency analysis.

Keywords: wavelet transform, Fourier transform, physics education

Introduction

It is well known that an integrated approach of Mathematics, Physics and laboratory activities can substantially increase the student learning processes, especially for Mathematics concepts which do not have a direct meaning (see Figure 1). This can be attributed to the fact that a lot of students find more effective to deal with Mathematics topics on the basis of practical experiences instead of dealing merely with mathematical descriptions.

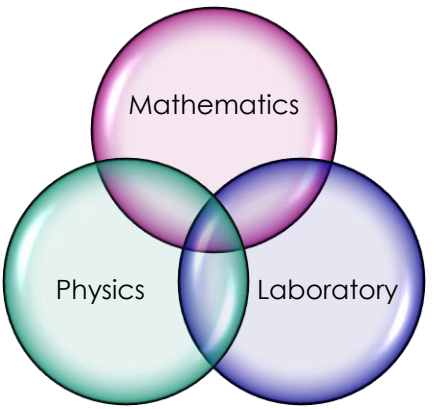

Figure 1. Mathematics concepts which do not have a straightforward meaning, as wavelets, are often considered hard to students. For this reason, in many cases it is often advantageous to adopt an integrated approach where Mathematics, Physics and Laboratory activities can furnish to notions concrete meanings and can highlight the usefulness, the advantages and the benefits of their applications.

Signal processing techniques have become increasingly important in many Physics, Mathematics and Engineering curricula, as well as in many other fields of applications, such as biology, neutron scattering, economy, medicine, meteorology, also because of the significant increase in computational power [1-7]. In particular, Fourier Transform (FT) and, very recently, Wavelet

Transform (WT) are largely applied to detect information on the periodicities which are present in stationary and non-stationary signals respectively.

In particular, WT provides a more detailed information because it works over a continuous range of scales and hence is more suited for studying both stationary and non-stationary phenomena [8-14].

In the present chapter the FT and WT analyses are presented dealing with the specific case of time dependent mechanical oscillations. It should be stressed that in such cases a generalization of the Newton's second law, to include the mass variation effect, is to be taken into account; furthermore in such cases the analytic approach alone is not able to easily solve the systems dynamics. It will be shown that for these systems, since FT analysis is not able to furnish information on the time dependence of the frequencies content, the WT approach is to be preferred.

Fourier and Wavelet Transforms – Historical Background

The idea of expanding periodic (non-periodic) functions in a sum (integral) of sine and cosine functions was introduced in 1822, in the treatise "Theorie Analytique de la Chaleur", by the French mathematician and physicist Joseph Fourier with the intention to solve the heat conduction equation.

FT analysis decomposes a signal, and then reconstructs it without loss of information, although being localized only in frequency and not in time; for this reason it allows to effectively analyse only stationary signals [15].

To overcome such a limitation a "window" function of given amplitude which slides along the time axis was introduced to execute a "time-localized" FT, i.e., the so called Short Time Fourier Transform (STFT); this procedure was introduced in 1946 in the paper titled "Theory of communication" by the Hungarian mathematician Dennis Gabor. D. Gabor chose a Gaussian function as window but, although he solved the problem of time localization, his approach furnished an equal resolution in time for all the frequencies, while window function width was kept constant [16].

Later, in the mid-1970s, the French geophysics Jean Morlet, working for an oil company, studying the acoustic echoes sent into the soil for identifying oil reservoirs on the Earth's crest, introduced the method of

scaling while shifting the STFT. In order to better analyse the acoustic echoes, Morlet changed the width of the window by a dilatation or compression procedure [17]. His approach led to the term "ondelette" introduced by J. Morlet and Alex Grossmann in 1984. The French term was translated in English as wavelet, which stands for wave (onde) and let (petite).

Fourier Series and Fourier Transform

It is well known that a periodic function $f(t+T)= f(t)$, with period $T = \frac{2\pi}{\omega}$,ω being a frequency, by means of the Fourier analysis can be expressed as a sum of sine or cosine functions [18-19]:

$$f(t) = \sum_{n=0}^{\infty}[A_n \cos(n\omega t) + B_n \sin(n\omega t)] \quad (1)$$

where A_n and B_n are the Fourier coefficients.

For n=0,$B_0 \sin(n\omega t) = 0$ and hence it is:

$$\int_0^T f(t)dt = \int_0^T A_0 dt = A_0 T \quad (2)$$

$$A_0 = \frac{1}{T}\int_0^T f(t)dt \quad (3)$$

Concerning the other A_n terms, let us multiply eqn. 1 for $\cos(m\omega t)$, and then integrate over T:

$$\int_0^T f(t)\cos(m\omega t)\,dt = \int_0^T \cos(m\omega t)\,\{\sum_{n=0}^{\infty}[A_n \cos(n\omega t) + B_n \sin(n\omega t)]\}dt \quad (4)$$

Where due to the Werner equations only the term $\cos(m\omega t)$ with $m = n$ is different from zero:

Therefore, being $\int_0^T f(t)\cos^2(m\omega t)\,dt = \frac{T}{2}$ it is:

$$A_n = \frac{2}{T}\int_0^T f(t)\cos(n\omega t)\,dt; \quad (5)$$

Following the same procedure, it results:

$$B_n = \frac{2}{T}\int_0^T f(t)\sin(n\omega t)\,dt; \tag{6}$$

The quantities A_n and B_n indicate the amplitude of the $\cos(n\omega t)$ and $\sin(n\omega t)$ and are called the harmonic components of function $f(t)$.

From an intuitive point of view, one can think to a color mixing, see Figure 2. In particular, assuming that, in general, light is a continuous spectrum of electromagnetic waves, since the eyes of humans, and of other species, normally contains three types of color receptors (trichromats), the additive primaries colors, i.e., red, green, and blue, are able to generate, by mixing, the largest range of visible colors. As shown in figure, additive mixing of red and green light, produces shades of yellow or orange depending on the different values of the mixing proportions (in the analogy different values of the coefficients A_n and B_n). Mixing green and blue produces shades of cyan, and mixing red and blue produces shades of purple and magenta; mixing equal proportions of the additive primaries results in shades of grey; when all three colors are fully saturated, the result is white.

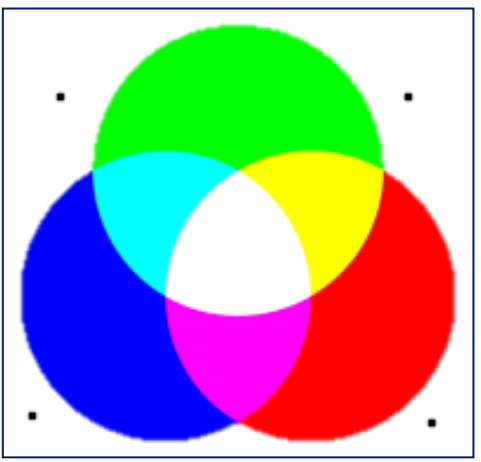

Figure 2. Additive mixing of the green, red and blue primaries colors generate the other visible colors. For example, red and green produce shades of yellow or orange depending on the mixing proportions (corresponding to different values of the Fourier coefficients A_n and B_n); green and blue produce shades of cyan; red and blue produce shades of purple and magenta; mixing equal proportions of the additive primaries results in shades of grey while when the three colors are saturated the result is white.

It should be noticed that different functions having the same period have the same fundamental harmonic component. The passage from the function $f(t)$ to the sequence of the Fourier coefficients $\{A_0, A_n, B_n\}$ is interpreted as an *analysis* process whereas the inverse operation that leads from the coefficients of Fourier to function $f(t)$ is interpreted as a *synthesis* process. The $\{A_0, A_n, B_n\}$ coefficients are called the spectrum of the function $f(t)$.

As a rule, by increasing the index n the n^{th} Fourier coefficient becomes smaller and smaller and therefore, in practical cases, the sum in eqn. 1 can be truncated at a given stage.

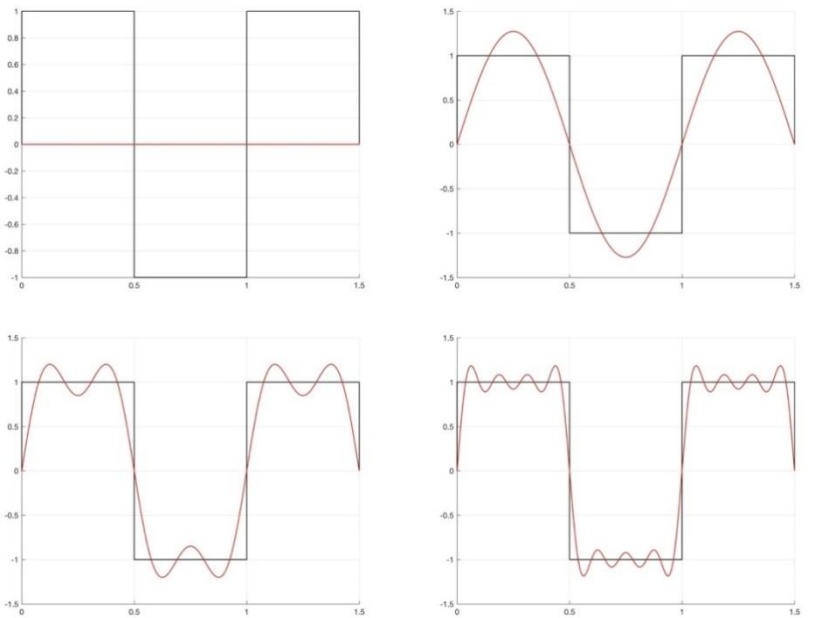

Figure 3. First Partial sums of the Fourier series for a square wave.

Figure 3 shows, as an example, the partial sums of the Fourier series for a square wave where it is:

$$A_0 = \frac{1}{2\pi}\int_0^{2\pi} f(t)dt = 0 \tag{7}$$

$$A_n = \frac{1}{\pi}\int_0^{2\pi} f(t)dx\cos(nt) = 0 \tag{8}$$

$$B_n = \frac{1}{\pi}\int_0^{2\pi} f(t)dt \sin(nt) = \begin{cases} \frac{1}{\pi n} \text{ if } n \text{ is odd} \\ 0 \text{ if } n \text{ is even} \end{cases} \quad (9)$$

The Fourier integral or Fourier transform is an extension of the Fourier series for non-periodic functions; it is an operator which associates to a function of the single variable t, $f(t)$, a function of a single variable υ (conjugate to *t*), $\hat{\mathrm{F}}(\upsilon)$. FT decomposes $f(t)$ into a set of sine (or cosine) waves and where frequency ω changes continuously:

$$\hat{\mathrm{F}}(\upsilon) = \int_{-\infty}^{+\infty} f(t)e^{-i2\pi\upsilon t}dt =$$
$$= \int_{-\infty}^{+\infty} f(t)\cos(2\pi\upsilon t)dt - i\int_{-\infty}^{+\infty} f(t)\sin(2\pi\upsilon t)dt \quad (10)$$

Eqn. 10 can be interpreted as a representation of the time signal $f(t)$ in the frequency domain through the function $\hat{\mathrm{F}}(\upsilon)$, obtained through a comparison between the signal $f(t)$ and a set of "template" functions $\cos(2\pi\upsilon t)$ and $\sin(2\pi\upsilon t)$. One can introduce the convolution operator, $\otimes$, see eqn. 3 and eqn. 4, which applies to two functions $f(t)$ and $\psi(t)$ and produces a third function obtained by the integral of the pointwise multiplication of the first function $f(t)$ and of the conjugate $\psi^*(t)$ of the second function $\psi(t)$ when this latter is translated. The convolution is similar to cross-correlation, *, see eqn. 13, differing only in a time reversal in one of the signals; finally for $f(t)$=$\psi(t)$ the cross-correlation becomes an autocorrelation function, see eqn. 14.

$$f(t)\otimes\psi(t) = \int_{-\infty}^{+\infty} f(\tau)\psi^*(t-\tau)d\tau \quad (11)$$

In the case of the Fourier integral, it is $\psi(t) = e^{i2\pi\upsilon t}$:

$$\hat{\mathrm{F}}(\upsilon) = f(t)\otimes\psi(t) = \int_{-\infty}^{+\infty} f(\tau)\psi^*(t-\tau)d\tau \quad (12)$$

Eqn. 4 indicates that the Fourier transform is essentially a convolution between the time function $f(t)$ and the sine and cosine functions that can be viewed as template functions. The operation measures the similarity between $f(t)$ and the template functions, and expresses the average frequency information during the entire period of the signal analyzed.

$$f(t) * \psi(t) = \int_{-\infty}^{+\infty} f(\tau)\psi^*(t+\tau)d\tau \quad (13)$$

$$f(t) * f(t) = \int_{-\infty}^{+\infty} f(\tau)f^*(t+\tau)d\tau \quad (14)$$

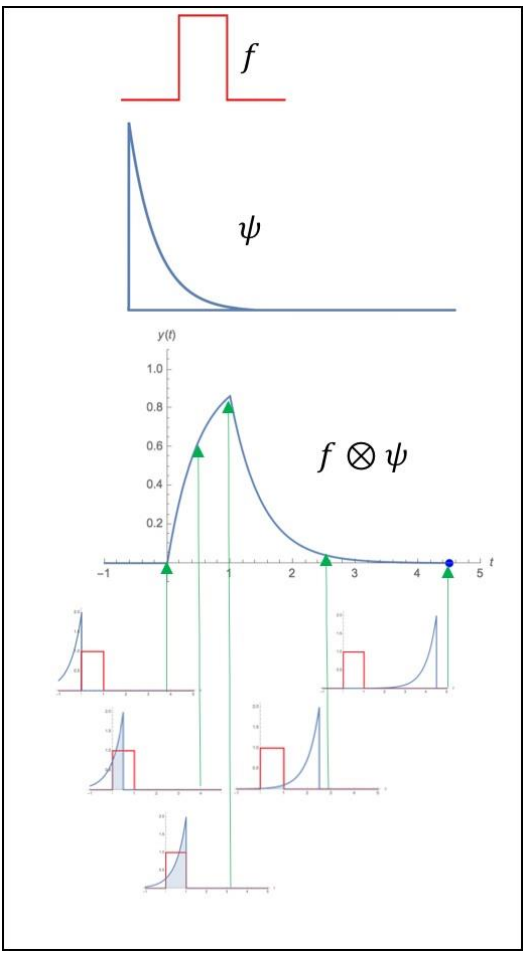

Figure 4. The convolution operator $\otimes$ applies to the two functions $f(t)$ and $\psi(t)$ and produces a third function obtained by the integral of the pointwise multiplication of the first function $f(t)$ and of the conjugate $\psi^*(t)$ of the second function ψ when this latter is translated.

To overcome the limitations of the Fourier transform a "time-localized" short-time Fourier Transform, STFT, was introduced by D. Gabor which can

also be viewed as a measure of "similarity" between the signal and the time-shifted and frequency-modulated Gaussian window function. Over the past decades, various types of window functions have been developed [20], each of them being specifically tailored toward a particular type of application. To cite a few examples, the Gaussian window was designed for analyzing transient signals; the Hamming and Hann windows were introduced for narrow bands, random signals the Kaiser-Bessel window was introduced in order to separate two signal components with frequencies very close to each other but with widely differing amplitudes.

The choice of the window function affects the time and frequency resolutions of the analysis. A high resolution provides a better separation of the signal components; however, the time and frequency resolutions of the STFT technique cannot be chosen arbitrarily at the same time, according to the uncertainty principle.

WT is an operator which associates to a function of the single variable t, $f(t)$, a function of the two variables a, τ, $W(a,\tau)$, where the parameter $a > 0$ denotes the scale, who sw value is the inverse of the frequency, while the parameter τ represents a time shift along the time axis. WT decomposes $f(t)$ into a set of wavelets components $\frac{1}{\sqrt{a}}\psi\left(\frac{t-\tau}{a}\right)$, that can be chosen according to the similarity degree with $f(t)$, as it follows:

$$W(a,\tau) = \frac{1}{\sqrt{a}}\int_{-\infty}^{+\infty} f(t)\psi^*\left(\frac{t-\tau}{a}\right)dt \tag{15}$$

where ψ^* denotes the conjugate complex of the function ψ. Similarly to FT, WT realizes a comparison of the function $f(t)$ with the set of the wavelets template functions, obtained from the scaling, i.e., dilation and contraction, and shift, i.e., translation along the time axis, looking for their similarities, that is, the degree of closeness between the two functions. The more similar they are the larger the $W(a,\tau)$ value will be. In this case, however the template functions are not necessarily the sine and cosine functions but can be arbitrarily chosen, provided that some conditions are satisfied.

Differently from FT, which shows only which signal frequencies are present, WT, in addition, also shows where, or at what scale they are [21-25]. Furthermore, while FT allows to decompose the signal only in cosine and sine component functions, the WT takes into account several wavelet mother functions, that can be chosen according to the similarity degree of the mother functions with the investigated signal [26-33].

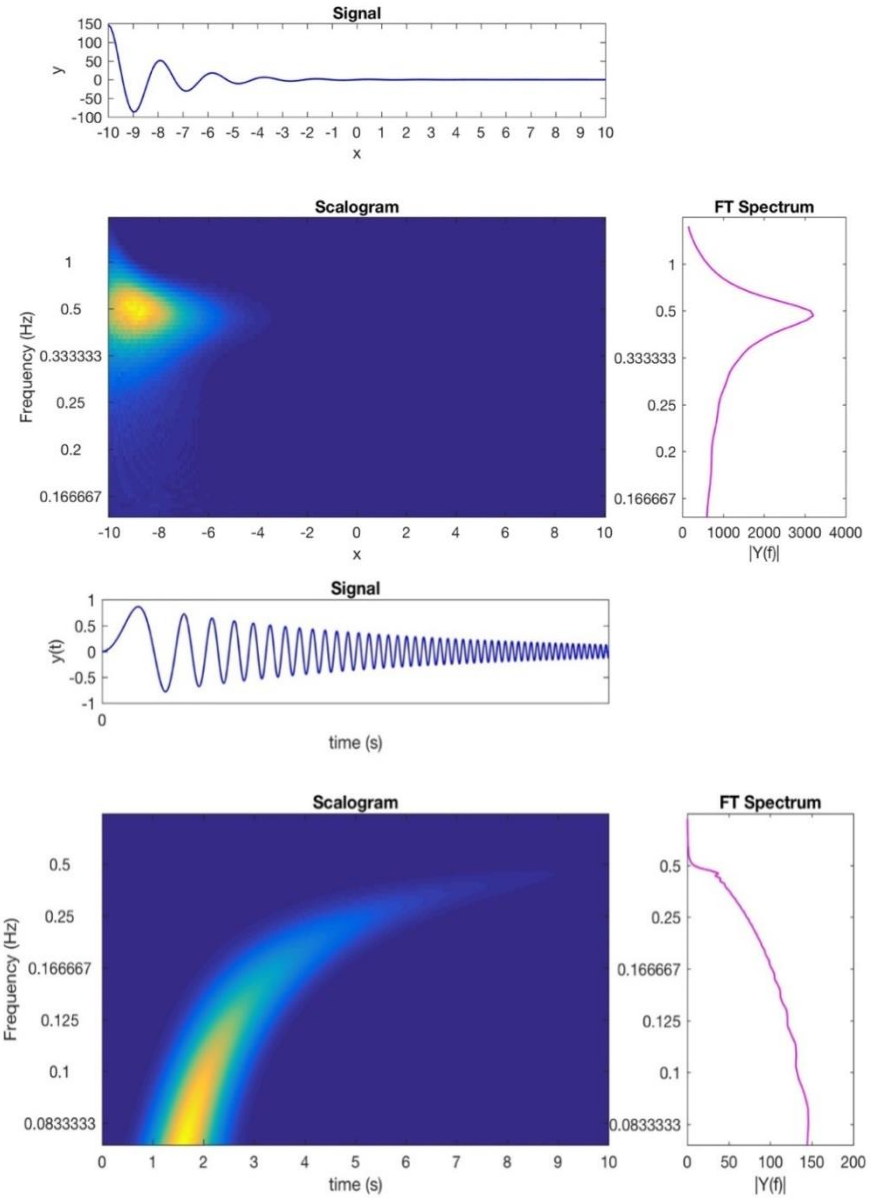

Figure 5. Comparison between the results of an FT and the WT spectral analysis obtained for a damped time oscillation (a) and for a chipir function (b). In the case of the chipir function it is evident that FT furnishes only an average frequency value while WT furnishes information on the time evolution of the frequencies content.

In this chapter, the wavelet Morlet mother function is used:

$$\psi(t) = \frac{1}{\sqrt{\pi F_b}} e^{(2i\pi F_c t)} e^{-\frac{t^2}{F_b}} \tag{8}$$

Here, F_b and F_c provide the wavelet bandwidth, which is connected with the duration of the time window, and the center pseudo-frequency position. It should be noted that no information about time dependence is obtained in case of a very long time window; in other words, in the case in which the wavelet mother is $\psi(t) = e^{-2\pi i t}$ the WT transform reduces to the FT. Therefore, the parameters of the "Morlet" mother function are to be adjusted to the dealt specific case [34-37].

Figure 5 shows a comparison between the results of the FT and the WT spectral analysis for a damped time oscillation (a) and a chipir function (b). As it can be seen in the case of the chipir function, contrarily to what occurs for FT which furnishes only an average frequency value, WT allows to get information on the time evolution of the frequencies content, namely WT allows a joint time-frequency analysis.

Variable Length Pendulum

Let us analyze a pendulum of length $\ell(t)$ and mass μ, in the absence of frictions. The second law of Dynamics is:

$$\mu\vec{a} = \vec{F} \tag{16}$$

where $\vec{a}$ is the linear acceleration, $\vec{F}$ the total force. In this case it is:

$$\mu\ddot{s} = -\mu g \sin\varphi \tag{17}$$

where φ angular deviation from the equilibrium position; $s=\ell(t)\varphi(t)$ is the length spanned by the oscillator, $\ddot{s} = \frac{d^2 s}{dt^2}$ is its second derivative, and g the gravity acceleration. It is:

$$\dot{s}(t) = \dot{\ell}(t)\varphi(t) + \ell(t)\dot{\varphi}(t) \tag{18}$$

Therefore, the second derivative is:

$$\ddot{s} = \ddot{\ell}\theta + 2\dot{\ell}\dot{\varphi} + \ell\ddot{\varphi} \tag{19}$$

Now, assuming that: i) the pendulum length changes with a constant rate, $\dot{\ell} = const.$ and hence $\ddot{\ell} = \frac{d^2\ell}{dt^2} = 0$; ii) during the oscillation, the pendulum length $\ell(t)$ changes slowly in respect to $\theta(t)$ variation, $\dot{\ell} \ll \dot{\varphi}$, then $\ddot{s} = \ell\ddot{\varphi}$, and hence:

$$\mu\ell(t)\ddot{\varphi}(t) = -\mu g \sin\varphi(t) \tag{20}$$

If $\varphi(t) \ll 1$ then $\sin\varphi\,(t) \sim \varphi$(t), and then:

$$\ddot{\varphi}(t) = -\frac{g}{\ell(t)}\varphi(t) \tag{21}$$

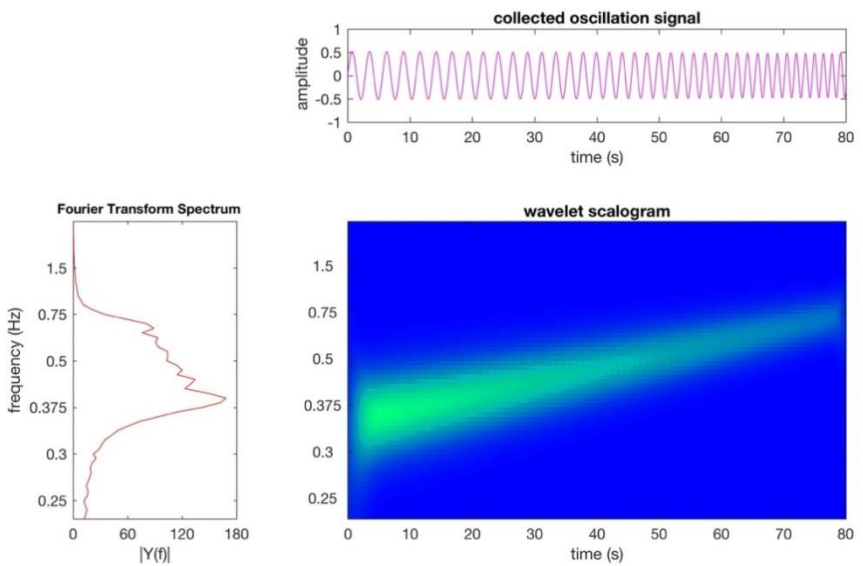

Figure 6. FT vs WT comparison. Both the approaches are applied to characterize the effects of the pendulum length change on the time-dependent oscillation frequencies. On the top: collected oscillation signal; on the right: signal FT which shows only an average of the oscillation frequencies; on the bottom: signal WT scalogram which shows how the oscillation frequency changes with time. WT outperforms the FT approach highlighting which frequencies are present and where they are.

The solution of this equation is:

$$\alpha(t) = \alpha_0 \sin(\omega(t)t + \varphi) \tag{22}$$

with:

$$\omega(t) \approx \sqrt{\frac{g}{\ell(t)}} \tag{23}$$

The experimental set-up includes: i) a 0,150 kg spherical mass; ii) a rotating device for the pendulum length variation; iii) a Logger Lite data acquisition program; IV) a GoMotion-Vernier ultrasonic sensor device to measure displacements. We have collected, and then analyzed by a WT approach, a set of measurements in which the length changed linearly in time following the law $\ell(t) = \ell_0 - \frac{1}{40}t$ (meter vs second). Figure 6 shows, on the top, the collected oscillation signal. As it can be seen while the signal FT, shown on the right, provides only an average of the oscillation signal frequencies, the WT scalogram, on the bottom shows the oscillation frequency changes in time [38].

Variable Mass Pendulum

Let us now take into account a funnel filled with sands and hang through a thread of fixed length ℓ whose $\mu(t)$ changes in time from its initial value m_0 following the law:

$$\mu(t) = \mu e^{-\beta t} \tag{24}$$

The rigid body dynamics equations are:

$$\begin{cases} \bar{F} = \overline{\dot{P}} \\ \bar{\tau} = \overline{\dot{L}} \end{cases} \tag{25}$$

where $\bar{F}$ is the net external force, $\bar{P}$ is the linear momentum which can be expressed in terms of the center mass velocity $\bar{v}_G$ as $\bar{P} = m\bar{v}_G$; $\bar{\tau}$ is the net external torque, $\bar{L} = \bar{r} \wedge \bar{P}$ is the total angular momentum. It is:

$$\bar{L} = I\bar{\omega} \tag{26}$$

where I is the system moment of inertia and $\omega = \dot{\vartheta}$ is the modulus of the angular velocity.

Being $|\bar{\tau}| = |\bar{r} \wedge \bar{F}| = \mu g \ell \sin\vartheta$, it is:

$$\begin{cases} \tau = -\mu g \ell \sin\vartheta = -\mu_0 e^{-\beta t} g \ell \sin\vartheta \\ I = \mu \ell^2 = \mu_0 e^{-\beta t} \ell^2 \end{cases} \tag{27}$$

and hence:

$$\bar{\tau} = \dot{I}\bar{\omega} + I\dot{\bar{\omega}} = -\mu_0 \ell^2 e^{-\beta t} \alpha\bar{\omega} + \mu_0 e^{-\beta t} \ell^2 \dot{\bar{\omega}} = -I\bar{\omega}\beta + I\dot{\bar{\omega}} \tag{28}$$

and by multiplying for $(1/I)$, it results:

$$-\bar{\omega}\alpha + \dot{\bar{\omega}} = -\frac{1}{\ell} g \sin\vartheta \hat{\jmath} \tag{29}$$

Assuming: i) small oscillation angles, then $\sin\vartheta = \vartheta$, and ii) $\omega_0 = \sqrt{\frac{g}{l}}$, one has:

$$\ddot{\vartheta} - \alpha\dot{\vartheta} + \omega_0\vartheta = 0 \tag{30}$$

which represents a homogeneous second order differential equation. By putting $\vartheta(t) = e^{-\gamma t}$:

$$\gamma^2 - \beta\gamma + \frac{g}{\ell} = 0 \tag{31}$$

it results:

$$\gamma_{1,2} = \frac{\alpha \pm \sqrt{\beta^2 - 4^{g}/_{\ell}}}{2} \tag{32}$$

The solution results:

$$\alpha(t) = k_1 e^{\gamma_1 t} + k_2 e^{\gamma_2 t} \tag{33}$$

In particular when is:

$$\beta^2 - \frac{4g}{\ell} > 0 \tag{34}$$

i.e.:

$$\beta > 2\sqrt{\frac{g}{\ell}} \tag{35}$$

the motion is not oscillating; on the contrary when it is:

$$\beta > 2\sqrt{\frac{g}{\ell}} \tag{36}$$

$$\gamma_{1,2} = \frac{\beta \pm i\omega}{2} \tag{37}$$

one has an oscillatory motion with frequency ω:

$$\omega = \sqrt{4\,{}^{g}/_{\ell} - \beta^2} \tag{38}$$

The procedure does not take into account that while the empty funnel center of mass keeps constant in time the center of mass of the sand inside the funnel lowers its position giving rise to an increase of the effective length; however such an effect is partially compensated by the fact that the empty funnel center of mass will increase its relative weight. Therefore one can assume that introducing the effecting length $\ell_{eff}(t)$, one has:

$$\omega(t) \approx \sqrt{\frac{g}{\ell_{eff}(t)}} \tag{39}$$

The experimental set-up includes: i) a funnel whose weight is 0,270 kg; ii) fine sand for a total mass of 1,790 kg; iii) a twine with a distance between the fixed support and the funnel of 0,66 m; a precision balance with capacity=2,100 kg; iv) a Logger Lite data acquisition program; v) a GoMotion-Vernier ultrasonic sensor device.

Regarding the experiment procedure, the funnel was filled with the sand and the measured mass variation versus time fulfilled the law $\mu(t) = \mu_0 e^{-\frac{1}{0.036}t}$.

Figure 7 shows in its upper portion the collected oscillation signal. As it can be seen, since the spectral content of the investigated process changes in time, FT as shown in the right portion of the figure is able to furnish only a mean oscillation frequency. Such a FT drawback is overcome by the employment of the WT analysis which furnishes the time evolution of the signal spectral components [39].

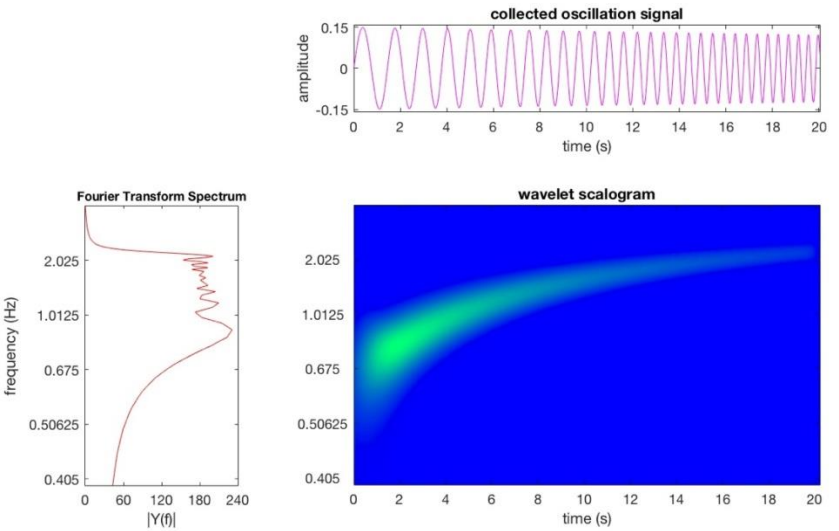

Figure 7. FT vs WT comparison. Both the approaches have been applied to characterize the effects of the pendulum mass change on the time-dependent oscillation frequencies. On the top the collected oscillation signal; on the right the signal FT which shows only an average of the oscillation frequencies; on the bottom the signal WT scalogram which shows how the oscillation frequency changes with time. WT outperforms the FT approach highlighting which frequencies are present and where they are.

Conclusion

In this chapter, a comparison of FT and WT approaches, finalized to signal processing, are introduced. In particular, we report the results obtained by the

application of FT and WT analysis on two Physics experiments, i.e., the motion of a variable length pendulum and the motion of a variable mass pendulum. These two motions are analyzed by means of a comparative FT and WT approach. Through these two experiments it is shown how, contrarily to FT that furnishes only an average frequency value for the non-stationary signal, WT allows to get information on the time evolution of the frequencies content, i.e., it allows a joint time-frequency analysis. It is shown that WT outperforms the FT approach highlighting which frequencies are present and, in addition, where they are, so providing an easy-to-interpret physical significance of time-frequency analysis. It is shown how Physics, together with its laboratory activities, can facilitate the clarification of this Mathematics concept and specifically that in teaching wavelet analysis it is often advantageous to adopt an integrated mathematical and physical approach.

References

Akulenko LD, Nesterov SV, The stability of the equilibrium of a pendulum of variable length, *J. Appl. Math. Mech.* 73, (2009) 642–647.

Caccamo MT, Cannuli A, Calabrò E, Magazù S, Acoustic Levitator Power Device: Study of Ethylene-Glycol Water Mixtures. *IOP Conf. Ser. Mater. Sci. Eng.* 2017, 199, 12119.

Caccamo MT, Magazù S, Ethylene Glycol - Polyethylene Glycol (EG-PEG) Mixtures: Infrared Spectra Wavelet Cross-Correlation Analysis. *Appl Spectrosc.* 2017, 71, 401-409.

Caccamo MT, Magazù S, Multiscaling Wavelet Analysis of Infrared and Raman Data on Polyethylene Glycol 1000 Aqueous Solutions. *Spectrosc Lett.* 2017, 50, 130-136.

Caccamo MT, Magazù S, Tagging the oligomer-to-polymer crossover on EG and PEGs by infrared and Raman spectroscopies and by wavelet cross-correlation spectral analysis. *Vib Spectrosc.* 2016, 85, 222-227.

Caccamo MT, Magazù S, Thermal restraint on PEG-EG mixtures by FTIR investigations and wavelet cross-correlation analysis. *Polym Testing* 2017, 62, 311-318.

Caccamo MT, Magazù S, *Variable Length Pendulum Analyzed by a Comparative Fourier and Wavelet Approach, Revista Mexicana de Fisica,* in Press.

Caccamo MT, Magazù S, Variable mass pendulum behaviour processed by wavelet analysis. *Eur. J. Phys*. 2017; 38(1): article number 15804.

Chopra S, Marfurt KJ, Choice of mother wavelets in CWT spectral decomposition, *83rd Annual International Meeting*, SEG, Expanded Abstracts, 2957–2961.

Delgado M, Portnoy A, Fuquene JA, Controlling the Oscillations of a Variable Length Pendulum, *Rev. Bras. Biom.* 24 (2010) 66–84.

Feynman RP, Leighton RB, and Sands ML, *The Feynman lectures on physics*. Reading Mass.: Addison-Wesley Pub. Co, 1963.

Fourier J, *The analytical theory of heat* (Cambridge University Press, 2009).

Gabor D, Theory of Communication, *J. Inst. Elec. Eng.* 93 (1946) 429–457.

Morlet J, Arens G, Fourgeau E, Glard D, Wave propagation and sampling theory, Part II: Sampling theory and complex waves., *Geophysics.* 47 (1982) 203–221.

Galli AW, Heydt GT, Ribeiro PF, Exploring the power of wavelet analysis, *IEEE Comput. Appl. Power*, 9, (1996) 37–41.

Magazù S, Calabrò E, Caccamo MT, Cannuli A, The shielding action of disaccharides for typical proteins in aqueous solution against static, 50 Hz and 1800 MHz frequencies electromagnetic fields. *Curr. Chem. Biol.* 2016, 10, 57-64.

Mallat SG, A theory for multiresolution signal decomposition: the wavelet representation *IEEE Trans. Pattern Anal. Mach. Intell.* 11 (1989) 674–693.

Marchese N, Cannuli A, Caccamo MT, C, Pace 2016 New generation non-stationary portable neutron hhhgenerators for biophysical applications of neutron activation analysis. *Biochimicaet Biophysica Acta* (BBA) 1861, Part B, 3661-3670.

Magazù S, Migliardo F, Caccamo MT, Innovative Wavelet Protocols in Analyzing Elastic Incoherent Neutron Scattering. *J. Phys. Chem. B*, 116, 2012, 9417-9423.

Magazù S, Migliardo F, Caccamo MT. Upgrading of resolution elastic neutron scattering (RENS), *Advances in Materials Science and Engineering*, Volume 2013, 2013, Article number 695405.

Magazù S, Migliardo F, Vertessy BG, Caccamo MT, Investigations of Homologous Disaccharides by Elastic Incoherent Neutron Scattering and Wavelet Multiresolution Analysis, *Chem. Phys.* 424, 56-61 (2013).

Mallat S, *A Wavelet Tour of Signal Processing*, 3rd ed. (Academic Press, 2008).

Miao XG, Moon WM, Application of wavelet transform in reflection seismic data analysis. *Geosc. J.* 3, 171-179 (1999).

Migliardo F, Caccamo MT, Magazù S, Elastic incoherent neutron scatterings wavevector and thermal analysis on glass-forming homologous disaccharides. *J. Non Cryst. Solids.* 2013;378, 144-151.

Migliardo F, Caccamo MT, Magazù S, Elastic Incoherent Neutron Scatterings Wavevector and Thermal Analysis on Glass-forming Homologous Disaccharides, *J. Non Crys Sol.* 378, 144–151 (2013).

Migliardo F, Magazù S, Caccamo MT, Infrared, Raman and INS Studies of Poly-Ethylene Oxide Oligomers," *J. Mol. Struc.* 1048, 261–266 (2013).

Migliardo F, Caccamo MT, Magazù S, Thermal Analysis on Bioprotectant Disaccharides by Elastic Incoherent Neutron Scattering. *Food Biophys.* 2014, 9, 99-104.

Morlet J, Arens G, Fourgeau E, Giard D, Wave propagation and sampling theory; Part II, Sampling theory and complex waves, *Geophysics*, 47 (1982) 222–236.

Oppenheim AV, Schafer RW, Buck JR, *Discrete time signal processing.* Prentice Hall PTR, Englewood Cliffs, NJ.

Osmond IT, Treatment of Simple Harmonic Motion, *Science* 22 (1905) 311-312.

Patterson LD, Pendulums of Wren and Hooke, *Osiris* 10 (1952) 277–321.

Priestley MB, Spectral Analysis and Time Series. *J. Time Ser. Anal.* 17 (1996) 85–103.

Prokoph A, Patterson RT, Application of wavelet and regression analysis in assessing temporal and geographic climate variability: Eastern Ontario, Canada as a case study, *Atm. Oc.* 42 (3), 201–212 (2004).

Serway RA, Beichner RJ, and Jewett JW, *Physics for scientists and engineers* (Brooks/Cole-Thomson Learning, 2000).

Squire PT, Pendulum damping, Pendulum damping, *Am. J. Phys*., 54, (1986) 984–991.

Tiersten MS, Force, momentum change and motion, *Am. J. Phys.*, 37 (1969) 82–87.

Wang XJ, Schmitt C, Payne M, Oscillations with three damping effects, *J. Phys.* 23, (2002) 155–164.

Welch PD, The use of fast Fourier transform for the estimation of power spectra: A method based on time averaging over short, modified periodograms, *IEEE Trans. Audio Electr.* 15, 70-73 (1967).

Xin X, Liu Y, A set-point control for a two-link underactuated robot with a flexible elbow joint. *Commun. Nonlinear Sci. Numer. Simul.* 19 (2014) 1544–1556.

In: Wavelets: Principles, Analysis and Applications ISBN: 978-1-53613-374-5
Editor: Joseph Burgess

Chapter 2

INT-HWT: INTERVAL EXTENSIONS AND OPTIMIZATIONS TO INCREASE PERFORMANCE AND ACCURACY OF HAAR WAVELET TRANSFORMS

***Vinícius R. dos Santos*[1,*], *Renata H. S. Reiser*[1,†], *Maurício Pilla*[1,‡] *and Alice J. Kozakevicius*[2,§]**
[1]Centre for Technological Development (CDTec)
Federal University of Pelotas-UFPEL
Pelotas, RS, Brazil
[1]Department of Mathematics
Universidade Federal de Santa Maria-UFSM
Santa Maria, RS, Brazil

Abstract

This work presents interval arithmetic extensions for the standard algorithms for the decimated and undecimated unidimensional Haar wavelet transform (HWT), and the standard and non-standard formulations for the two-dimensional HWT. The proposed algebraic optimizations for the algorithms are derived specifically for the formulation of the

[*]Corresponding Author Email: vrdsantos@inf.ufpel.edu.br.
[†]Corresponding Author Email: reiser@inf.ufpel.edu.br.
[‡]Corresponding Author Email: pilla@inf.ufpel.edu.br.
[§]Corresponding Author Email: alicek@ufsm.br.

HWT in the interval arithmetic context, being part of the already under development Int-HWT library, which is implemented using C-XSC library for interval arithmetic. This work is the first step to the development of the Int-DWTs library that will provide interval results for several Discrete Wavelet Transforms. The interval results show that the proposed formulations for the different standard algorithms for the HWT provide more exact values, with an increase of 20% in performance for the decimated HWT formulation. As an application, the interval optimizations for image filtering procedures based on the Hard and Soft thresholding of the wavelet coefficients are also presented, providing results more accurate than the standard algorithms with punctual values.

PACS: 07.05.Tp, 07.05.Pj

Keywords: Error analysis, Interval Arithmetics, Haar wavelet Transform, Compression

AMS Subject Classification: 65G30, 65G40

1. Introduction

The quality of numerical results in Scientific Computing (SC) depends on understanding the different error causes, on controlling their propagation and on improving accuracy and precision of computations upon the involved procedures. In this sense, the proposed study considers the Interval Mathematics (IM) approach for addressing this issue and proposes a solution based on Moore's arithmetic [1] for the implementation of the Haar wavelet transform (HWT). Two well established algorithms are considered: the Cascade for implementing the decimated version of the transform, and the Á Trous for the undecimated approach. Their standard formulations assume point values as input data, being the proposed interval formulation a first step on the development of the Int-DWT library that will provide interval results for several Discrete Wavelet Transforms (DWTs).

Interval results carry over the safety of their quality together with the degree of their uncertainty [1]. The diameter of the interval solution represents with fidelity the uncertainties of input parameters, being also an indicative of the error influence and of the extension of its propagation within the incoming data. Interval solutions also indicate truncation and rounding errors contained in the computed results. In the last decade, many studies associating wavelet

transforms with IM have arisen, promoting a new research direction and pointing out the relevance of interval computations for a wide range of applications. Shu-Li et al. [2] propose the interval extension of the interpolating wavelet family for the construction of an adaptive algorithm for solving partial differential equations (PDE). Another collocation method for solving PDE is presented by Liu [3], based on the interval extension for the Shannon-Garbor wavelet family. By analyzing wavelet synthesis in a piecewise manner, interval wavelet transform methods in [4] are considered to provide sparser representations in the vicinity of discontinuities than a classical wavelet transform, showing how they can be used for image compression and upscaling of signal approximation. With respect to image processing applications, Minamoto and Aoki [5] propose a blind digital image watermarking method using interval Daubechies wavelets.

The main motivation for interval techniques integrated with DWT is to provide trustworthy and validated results to technological and SC applications assuming such transformations. The pool of techniques involving wavelets is ample, specially in signal and image processing [6, 7]. The Haar basis, the less regular of the orthonormal Daubechies family, provides the simplest discrete wavelet transform (DWT) in terms of algorithm complexity and therefore is still nowadays largely explored. Its robustness with respect to many different mathematical structures and space formulations is also considered a relevant aspect [8] of the HWT addressed in different applications. Besides, as pointed out in [9], the imaging inaccuracy of the Haar wavelet basis is the smallest possible, motivating its usage in many 2D problems as well as the proposed formulations in the interval context presented in the current study.

Hence, this work introduces an integrated analysis of the original HWT algorithms and the proposed interval extensions. Preliminary results of the interval extension of the Int-HWT library, presented in [10], are revisited here, including the interval extensions of the decimated version of HWT [11] (given by the Cascade algorithm) for the 1D and 2D cases. Another contribution to be addressed is the interval extension for the non-decimated HWT formulation, given by the Á Trous algorithm [12, 13], in which the size of the input data does not change through out all the decomposition levels of the HWT. Interval extensions are also proposed for both 1D and 2D cases. Furthermore, a threshold procedure for treating signals and images, which is a significant part of many compression and filtering algorithms, is analyzed and its interval extension is presented. Interval metrics are also evaluated to validate the two studied interval filtering procedures.

This contribution is organized as follows. Section 2 summarizes some relevant aspects about interval arithmetics and the interval formulation of three metrics considered as figure of merit for analyzing the quality of the results obtained by the proposed interval extensions of the HWT. In the end of this section, some remarks about the C-XSC library, considered for the implementations, are also made. Section 3 presents the optimal interval formulations for the HWT. The 1D decimated formulation is discussed in Subsection 3.1 and the 1D undecimated case is given in 3.3. Both 2D formulations are also addressed. In Section 4 the interval extensions of two compression procedures are presented. Section 5 provides a pool of numerical simulations, for which some statistics are collected to demonstrate the gain related to the developed interval formulations. Finally, conclusions and future works are discussed in Section 6.

2. Interval Arithmetics

Interval analysis was devised by Ramon Moore in the 1960's [14, 15], when computers were still at an early stage of development and every additional cost associated with keeping track of computational errors was considered as too high. Furthermore, error bounds were overly pessimistic and, therefore, mostly useless for practical applications. Nowadays, the research for new interval methods have reached a high scientific level, producing tighter error bounds faster than approximations of non-rigorous computations. Even in pure mathematics, non-trivial results have recently been proved using computer-aided methods based on interval techniques [16]. Additionally, scientific computations demanding rigor as well as speed from numerical computations should be performed based on techniques with validated numerical calculations such as interval methods. Despite distinct approaches of arithmetic for intervals, such as [17, 18] and [19], this work considers the interval analysis proposed by Moore in the 1960's [1, 14, 15], providing methods to obtain accuray in numerical calculations.

2.1. Moore Interval Arithmetic Operations

In Moore's arithmetic, an interval X is a continuum subset of real numbers which is in the infimum-supremum representation given as:

$$X = \{x \in \mathbb{R} \colon a \leq x \leq b, a, b \in \mathbb{R}\}. \tag{1}$$

The set of all real intervals is indicated by $\mathbb{IR}$. Frequently, an interval $X \in \mathbb{IR}$ is indicated by its endpoints, $X = [a, b]$. When $a = b$ then $[a, b] \in \mathbb{IR}$ is called a degenerate interval. For an unary operator $\omega : \mathbb{R} \to \mathbb{R}$, we have that $\omega(X) = \{\omega(x) : x \in X\}$. According to [20], Def. 4.2 and Prop. 5.1, for a total and non-asymptotic real function $\omega : \mathbb{R} \to \mathbb{R}$, an interval function $\Omega(X) = \{\omega(x) : x \in X\}$, verifying properties below:

(i) Ω is an interval extension of ω, i.e. $\Omega(X) = [\omega(x), \omega(x)], \forall x \in X$;

(ii) Ω is correct w.r.t ω, implying that $\omega(x) \in \Omega(X), \forall x \in X$,

is well defined and called a canonical interval represention of w. In addition, for all $X \in \mathbb{IR}$, we have that $\Omega(X) = [\min f(x) : x \in X, \max f(x) : x \in X]$. Thus, for an interval representation function $* : \mathbb{IR}^2 \to \mathbb{IR}$ such that $* \in \{+, -, /, \cdot\}$, the following property is valid: $X * Y = \{x * y \colon x \in X \text{ and } y \in Y\}$, $\forall X, Y \in \mathbb{IR}$.

Interval functions can be computed by performing arithmetic operations or by applying rational approximation methods [17]. The former identifies the class of rational interval functions and the latter, the class of irrational interval functions. Thus, Moore arithmetic guarantees correctness in the sense that any computation performed with standard floating-point methods can also be done with their interval version. By considering the set $\Re = [-\infty, \infty]$ of extended real numbers, the related family of subintervals of $[a, b]$ is given as

$$\mathbb{I}_{[a,b]} = \{[x, y] \subseteq \Re \colon a \leq x \leq y \leq b\}. \tag{2}$$

In particular, let $U = [0, 1] \subseteq \Re$ be the real unit interval. By Eq. (2), the set of all subintervals of U is indicated as $\mathbb{I}_U = \{[x, y] \subseteq \Re \colon 0 \leq x \leq y \leq 1\}$. The projections $l, r : \mathbb{I}_{[a,b]} \to [a, b]$ are respectively given by $l([x, y]) = x$ and $r([x, y]) = y$, for all $[x, y] \in \mathbb{I}_{[a,b]}$. Additionally, when $X = [x, y] \in \mathbb{I}_{[a,b]}$, the projection functions $l(X)$ and $r(X)$ are also denoted by $\underline{X}$ and $\overline{X}$, respectively. Thus, for all $X, Y \in \mathbb{I}_{[a,b]}$, interval arithmetic operations can be defined as follows:

$$\begin{aligned}
X + Y &= [\underline{X} + \underline{Y}, \overline{X} + \overline{Y}];\\
X - Y &= [\underline{X} - \overline{Y}, \overline{X} - \underline{Y}];\\
1/Y &= [1/\overline{Y}, 1/\underline{Y}], \quad \text{if} \quad 0 \notin Y;\\
X \cdot Y &= [\min\{\underline{X} \cdot \underline{Y}, \underline{X} \cdot \overline{Y}, \overline{X} \cdot \underline{Y}, \overline{X} \cdot \overline{Y}\}, \max\{\underline{X} \cdot \underline{Y}, \underline{X} \cdot \overline{Y}, \overline{X} \cdot \underline{Y}, \overline{X} \cdot \overline{Y}\}].
\end{aligned}$$

The power, root and logarithm operations are, respectively, defined as follows:

$$X^n = \begin{cases} [\underline{X}^n, \overline{X}^n], & \text{if } \underline{X} > 0 \text{ or } n \text{ is odd;} \\ [\overline{X}^n, \underline{X}^n], & \text{if } \overline{X} < 0 \text{ and } n \text{ is even;} \\ [0, \max\{\underline{X}^n, \overline{X}^n\}], & \text{if } 0 \in X \text{ and } n \text{ is even.} \end{cases}$$

$$\sqrt[n]{X} = \begin{cases} [\sqrt[n]{\underline{X}}, \sqrt[n]{\overline{X}}], & \text{if } \underline{X} \geq 0 \text{ or } n \text{ is odd;} \\ \text{undefined,} & \text{otherwise.} \end{cases}$$

$$\log X = \begin{cases} [\log \underline{X}, \log \overline{X}], & \text{if } \underline{X} > 0; \\ \text{undefined,} & \text{otherwise.} \end{cases}$$

The partial order used here in the context of IM is the Product (or Kulisch-Miranker) order and, for all $X, Y \in \mathbb{I}_{[a,b]}$, it is defined as follows:

$$X \leq_{\mathbb{I}_{[a,b]}} Y \text{ iff } \underline{X} \leq \underline{Y} \text{ and } \overline{X} \leq \overline{Y}. \tag{3}$$

Additionally, an interval function preserving the partial order $\leq_{\mathbb{I}_{[a,b]}}$ is called $\mathbb{I}_{[a,b]}$-monotonic function with respect to the partially ordered set $(\mathbb{I}_{[a,b]}, \leq_{\mathbb{I}_{[a,b]}})$.

2.2. Interval Metrics

Not only interval algorithms, but metrics for evaluating procedure's accuracy may also assume concepts from IM [1] to manage computation errors. The motivation to consider numerical intervals instead of simple punctual values is linked to the capability of intervals to represent infinite punctual values. This sort of representation is very useful in SC when the accuracy of the input (or output) data is not known beforehand. In these cases of uncertainty or inaccuracy, the interval procedures should ensure that all possible punctual results belong to the interval results. In addition, due to memory limitation, it is also common to compute round (or simply truncated) values to store the result afterwards. This heuristic may result in different values which are depending on the machine's configuration.

The interval extension of real metrics being used in the current work to measure result quality are interval metrics in the sense of Trindade e.al. [21]. However, they are not interval metrics in the sense of Moore [20]. See [22] for a more general theory of metric spaces.

2.2.1. Euclidean Distance

Let $\tilde{Y} = (\tilde{y})_{ij} \in \mathbb{R}^{n\times m}$ be an estimator of $Y = (y)_{ij} \in \mathbb{R}^{n\times m}$ whose nm elements $\tilde{y}_{ij}$ are predictions of the original values y_{ij}. The Euclidean distance between Y and its estimator $\tilde{Y}$ is defined by the following expression:

$$D(\tilde{Y}, Y) = \sqrt{\sum_{j=0}^{m}\sum_{i=0}^{n}(\tilde{y}_{ij} - y_{ij})^2}. \tag{4}$$

Analogously, $\tilde{\mathbb{Y}} = (\tilde{\mathbf{Y}})_{ij}$ is called an interval estimator of $\mathbb{Y} = (\mathbf{Y})_{ij} \in \mathbb{IR}^{n\times m}$ with an nm-dimensional matrix of interval predictions $\tilde{\mathbf{Y}}_{ij}$ of the original interval quantities $\mathbf{Y}_{ij}$. An interval extensional of Eq.(4) is defined as:

$$\mathbf{D}(\tilde{\mathbb{Y}}, \mathbb{Y}) = \sqrt{\sum_{j=0}^{m}\sum_{i=0}^{n}\left(\tilde{\mathbf{Y}}_{ij} - \mathbf{Y}_{ij}\right)^2}. \tag{5}$$

2.2.2. Mean Squared Error

The Mean Squared Error (MSE) is a risk function, corresponding to the expected value of the squared error loss. It measures the average of the squares of the errors in SC, providing the difference between the estimator and what is estimated. MSE allows us to compare the pixel values of our original image to our image degraded by noise based on the amount by which the values they differ.

Let $Y = (y)_{ij} \in \mathbb{R}^{n\times m}$ be the related matrix of true values y_{ij}. The accuracy of $\tilde{Y} = (\tilde{y})_{ij}$ can be obtained by the application of an MSE operator as the following

$$MSE(\tilde{Y}, Y) = \frac{1}{mn}\sqrt{\sum_{j=0}^{m}\sum_{i=0}^{n}(\tilde{y}_{ij} - y_{ij})^2} = \frac{1}{mn}D(\tilde{Y}, Y). \tag{6}$$

Analogously, for all $\mathbb{Y} = (\mathbf{Y})_{ij} \in \mathbb{IR}^{n\times m}$ corresponding to the related matrix of true values $\mathbf{Y}_{ij}$, the accuracy of the estimated values can be obtained by applying an interval extension of the MSE operator in Eq. (4), which is

given by the following expression:

$$\mathbf{MSE}(\tilde{\mathbf{Y}}, \mathbf{Y}) = \frac{1}{mn}\sqrt{\sum_{j=0}^{m}\sum_{i=0}^{n}(\tilde{\mathbf{Y}}_{ij} - \mathbf{Y}_{ij})^2} = \frac{1}{mn}\mathbf{D}(\tilde{\mathbb{Y}}, \mathbb{Y}). \quad (7)$$

2.2.3. Peak Signal-to-Noise Ratio

An important performance metric for evaluation and comparison of image or video codecs is the Rate/Distortion (R/D), which measures the image quality in terms of Peak Signal-to-Noise Ratio ($PSNR$). $PSNR$ expresses the ratio between the maximum possible power of a signal and the power of corrupting noise affecting the fidelity of its representation. $PSNR$ is used to measure the quality of reconstruction of lossy compression codecs. The signal is the original data and the noise is the error introduced by compression. However, the range of validity of this metric is limited since it is only conclusively valid quality measure when used to compare results from the same content or same codec type. Thus, the expression of $PSNR$ is most easily defined via the logarithmic decibel scale related to the MSE as follows:

$$PSNR(\tilde{Y}, Y) = 10 \cdot \log_{10} \frac{MAX_I^2}{MSE(\tilde{Y}, Y)}, \text{if } MSE(\tilde{Y}, Y) \neq 0 \quad (8)$$

when I indicates a mn-dimensional monochrome image associated to Y and MAX_I is the maximum possible pixel value of the image I. When $\tilde{Y} = Y$, then $MSE(\tilde{Y}, Y) = 0$ and it makes no sense to compute the PSNR value. Therefore, a natural interval extension of Eq. (8) is given as:

$$\mathbf{PSNR}(\tilde{\mathbf{Y}}, \mathbf{Y}) = 10 \cdot \log_{10} \frac{[MAX_I, MAX_I]^2}{\mathbf{MSE}(\tilde{\mathbf{Y}}, \mathbf{Y})}, \text{if } 0 \notin \mathbf{MSE}(\tilde{\mathbf{Y}}, \mathbf{Y}) \quad (9)$$

when $[MAX_I, MAX_I]$ denotes the degenerate interval obtained by MAX_I and $\mathbf{MSE}(\tilde{\mathbf{Y}}, \mathbf{Y})$ is the interval extension of $MSE(\tilde{Y}, Y)$. Finally, in the computation of the MSE between two identical images, the value will be zero and hence PSNR will be undefined. Moreover, the main limitation of both metrics is that they strictly rely on numerical comparison, which is exactly the focus of this contribution.

2.3. C-XSC Library

Algorithms performing only interval arithmetic must be designed in a way that interval results contain all possible punctual results. In this work, HWT and its many formulations are extended according to the interval arithmetic, considering the C-XSC interval library [23]. C-XSC is an extensive C++ class library for SC that includes a set of basic data types definitions (from intervals to multiple precision complex intervals). These types are predefined and can be called by their usual operator symbols. So, arithmetic expressions and numerical algorithms are expressed in a notation that is very close to the usual mathematical notation and verification algorithms are written in a way which is very near to pseudo-code used in SC. All predefined numerical operators are of highest accuracy, meaning that computed results differ from the correct result by at most one rounding.

Such system incorperated some concepts of mathematics of computation and computational arithmetic, such as high accuracy arithmetic, interval mathematics and automatic numerical verification. C-XSC is an open source library available from [23] that adds extra packages, such as extended interval division, evaluation of polynomials, automatic differentiation, linear and nonlinear equations, global linear and optimization, accurate evaluation of arithmetic expressions,etc.

Function and operator overloading ease the common mathematical notation of expressions involving interval types. This is also true for (interval) matrix/vector expressions. Numerical verification methods, also called self-validating methods, are constructive and they allow to handle uncertain data with mathematical rigor. The C-XSC library provides support for users to develop efficient numerical verification methods in self-validating numerical applications.

2.4. Int-DWTs Library

The implementation of our interval extension and optimizations for the HWT is maintained using a Git repository at [1]. The library distribution is being made using Github, an open-source development platform for easy access.

The Int-DWTs library requires three programs in order to be compiled, which are $make$, $clang$ and $cxsc$. The following commands show how to install

[1] github.com/fireapache/Int-DWTs

the required programs.

```
$ sudo apt-get install make
$ sudo apt-get install clang
$ wget http://www2.math.uni-wuppertal.de/~xsc/xsc/
cxsc/cxsc-2-5-4.tar.gz
$ tar -zxvf cxsc-2-5-4.tar.gz
$ cd cxsc-2-5-4/
$ ./install_cxsc
```

It is important to install $cxsc$ at $/home/ < user > /cxsc/$, where $< user >$ is the user's name in the system. The following commands show how to clone the repository and to compile the library.

```
$ git clone https://www.github.com/fireapache/Int-DWTs/
$ cd Int-DWTs/
$ make tests
```

The compilation process will produce an executable named $test.exe$, which has several implemented tests. The program can list the available tests by using the $-l$ flag and can execute a given test by using $-t\ n$, being n the selected test number.

In the last decade, significant improvements have been made in parallelized versions of interval linear system solvers supplied by C-XSC [24, 25, 26]. Once the interval extensions allow different error computations, different compression algorithms can be derived, as shown in Section 4. With the summarized background already presented, the remainder of this work develops the extension of the Haar wavelet transform for the context of interval arithmetics. Some formulation simplifications are made in order to improve the quality of interval extensions of related transforms, directly implying in more accurate results. Image compression step is chosen as a case study of the techniques discussed before.

Thus, interval techniques and optimization of Int-DWTs library are mainly concerned with execution performance, accuracy of the calculations stating the relation between the diameter of intervals and computing errors, together with metrics providing quality measures of results. Additionally, constrains in performances are discussed based on algorithm complexity analysis.

3. Optimal Interval Formulations for the HWT

The Haar basis was proposed in 1910, introduced by the Hungarian mathematician Alfred Haar [27] in a different approach than the one considered by Ingrid Daubechies in 1988, when she presented her orthogonal basis of wavelet functions with compact support for the space of square integrable functions[28]. Nevertheless, through her work, the Haar functions started to be seen as a particular case of orthogonal wavelets. Nowadays, the HWT is well stated through different fast algorithm formulations, been well established for many applications, specially those involving data compression, as considered by JPEG-2000 [29].

When dealing with the original algorithms of the HWT [11, 12], the transformation is characterized by a convolution with a family of filters. For the unnormalized transform the filters are $h = [1/2, 1/2]$ and $g = [1/2, -1/2]$. For the normalized case, $h = [1/\sqrt{2}, 1/\sqrt{2}]$ and $g = [1/\sqrt{2}, -1/\sqrt{2}]$, implying that divisions by $\sqrt{2}$ have to be considered in all iterations within the HWT decomposition. Once $\sqrt{2}$ is not a computable value, each composition or decomposition level adds a certain degree of error, generated in each iteration and then propagated through all levels until the end of the HWT procedure. In [30] a solution to avoid this loss of accuracy for the interval extension of the decimated HWT was proposed based on algebraic simplifications performed to eliminate the computation of these non computable rational values, $2^{j/2}$. As a result, more reliable results in comparison with the original ones given in [11, 13] were obtained.

In this section, the heuristic from [30] is briefly summarized. New interval extensions for the undecimated HWT inspired by the previously proposed simplifications are addressed as part of our main contributions. Assuming the same input data and all different formulations of the HWT: the Cascade (decimated) and Á Trous (undecimated) algorithms for both normalized and non-normalized approaches are analyzed and their interval versions developed here are compared. All algorithm complexities are expressed in terms of worst case complexity.

3.1. 1D Decimated Int-HWT Simplification

According to the description in [11], when assuming the decimated HWT and given an initial vector C^j with $n = 2^j$ punctual values, the one-dimensional

non-normalized HWT calculates the averages (convolution of C^j with the filter $h = [1/2, 1/2]$) and differences (convolution with $g = [1/2, -1/2]$) of each pair of adjacent elements in the input vector C^j, $(C^j_{2k-1}, C^j_{2k}), k = 1, ..., n/2$, generating therefore two output sets: one denoted by C^{j-1} for the scaling (averages) and another for the wavelets (differences) coefficients D^{j-1}, both with $n_1 = n/2$ points, half size of the original input vector C^j, assumed to be given in the finest resolution level j. For the normalized version of the HWT, the only modification is the consideration of the normalized set of filters.

Since the HWT main feature is to decompose information in many resolution levels, the next level of the decimated HWT decomposes C^{j-1} in a second pair of half-sized vectors, C^{j-2} and D^{j-2} both now with size $n_2 = n_1/2$. This procedure is recursively defined by further decomposing the scaling components and can be applied until a specific level of coarser resolution is achieved or until a single scalar scaling coefficient and a single wavelet coefficient are obtained. The whole process of the direct HWT (also called decomposition) produces a multi-resolution representation of the input vector C^j in terms of the complete set of all wavelet and scaling coefficients, represented by the $1:1$ correspondence $C^j \longleftrightarrow (C^0, D^0, D^1, ..., D^{j-1})$.

The novelty on the interval code remains in the definition of vectors as interval vectors [31]. Constants are defined as interval quantities and all arithmetics are treated as interval operations. In this sense, $h = (1/\sqrt{[2;2]}, 1/\sqrt{[2;2]})$ and $g = (1/\sqrt{[2;2]}, -1/\sqrt{[2;2]})$ (considered as interval quantities) are the normalized interval filters associated to the Int-HWT, being part of the interval extension of the standard algorithm.

The simplification of the normalized decomposition procedure for the decimated version of the Int-HWT, either 1D or 2D, is executed in the following order: first a non-normalized decomposition is made, as indicated by the pseudo-code in Figure 1; the normalization of all coefficients is performed after this stage, multiplying them by the normalization factor $2^{-j/2}$, where j is the resolution level of the coefficients throughout the decomposition. Depending on j, the computation of $\sqrt{2}$ may be unnecessary, avoiding any computation error in this case. This process is illustrated in Figure 1 with an example presented in [11], assuming $C^2 = [9 \quad 7 \quad 3 \quad 5]$ the input vector. The complete decomposition of $C^2 \longleftrightarrow (C^0, D^0, D^1) = [6 \quad 2 \quad 1 \quad -1]$ is obtained by 2 levels of the non-normalized 1D HWT. The normalization step if performed as a final separate procedure, given the output $[6 \quad 2 \quad 1/\sqrt{2} \quad -1/\sqrt{2}]$.

Figures 2 and 3 show interval extensions of the decimated 1D HWT pro-

$$[9 \quad 7 \quad 3 \quad 5] \quad \rightarrow \quad [6 \quad 2 \quad 1 \quad -1] \quad \rightarrow \quad [6 \quad 2 \quad \tfrac{1}{\sqrt{2}} \quad \tfrac{-1}{\sqrt{2}}]$$

Input **Decomposition** **Normalization**

Figure 1. Example of two level decimated 1D HWT with optimized normalization step.

cedure, which are referenced as Int-HWT in this work. Figure 2 presents the normalized case of decomposition and Figure 3 shows the non-normalized one. The number of operations from $DecompositionStep$ is $n+1$, and for the main $Decomposition$ algorithm the number of operations is $n+\log(n)\cdot(n+2)+1$. Our proposed simplification, represented in Figure 4, reduce the same number of operations to n and $n+n\cdot\log(n)$, respectively.

Where C and C' are arrays of interval data

Decomposition $(C[1..n])$
1 $C \leftarrow C/\sqrt{[2;2]}$;
2 $i \leftarrow n$;
3 **while** $i > 1$ **do**
4 | $DecompositionStep(C[1..i])$;
5 | $i \leftarrow i/2$;
6 **end**

DecompositionStep $(C[1..n])$
1 **for** $i \leftarrow 1$ ***to*** $n/2$ **do**
2 | $C'[i] \leftarrow (C[2i-1]+C[2i])/\sqrt{[2;2]}$;
3 | $C'[i+n/2] \leftarrow (C[2i-1]-C[2i])/\sqrt{[2;2]}$;
4 **end**
5 $C \leftarrow C'$;

Figure 2. 1D decimated Int-HWT: normalized decomposition process.

Decomposition $(C[1..n])$
1 $i \leftarrow n$;
2 **while** $i > 1$ **do**
3 | $DecompositionStep(C[1..i])$;
4 | $i \leftarrow i/2$;
5 **end**

DecompositionStep $(C[1..n])$
1 **for** $i \leftarrow 1$ ***to*** $n/2$ **do**
2 | $C'[i] \leftarrow (C[2i-1]+C[2i])/[2;2]$;
3 | $C'[i+n/2] \leftarrow (C[2i-1]-C[2i])/[2;2]$;
4 **end**
5 $C \leftarrow C'$;

Figure 3. 1D decimated Int-HWT: non-normalized decomposition process.

The normalization procedure in Figure 4 performs the normalization step of all coefficients after their convolution using the non-normalized filters. Since it is executed once on every coefficient of a n sized vector, the number of operations is n. By performing a non-normalized transform and the normalization procedure afterwards, the number of operations is $n\log(n)+n$, which is the

same amount of operations from the normalized transformation. The goal is therefore the gain in exactitude obtained by avoiding high number of divisions using $\sqrt{2}$ from the original $DecompositionStep$ algorithm, as shown in Figure 20. According to [11], in the inverse transform (also called composition

```
   Normalization (C[1..n])
1  levels ← log2(n) ;
2  for i ← 1 to levels do
3  |  start ← i^2 ;
4  |  end ← (i+1)^2 ;
5  |  for j ← start to end do
6  |  |  C[j] ← C[j] * 2 ∧ (−(i/2)) ;
7  |  end
8  end
```

```
   Denormalization (C[1..n])
1  levels ← log2(n) ;
2  for i ← 1 to levels do
3  |  start ← i^2 ;
4  |  end ← (i+1)^2 ;
5  |  for j ← start to end do
6  |  |  C[j] ← C[j] / 2 ∧ (−(i/2)) ;
7  |  end
8  end
```

Figure 4. 1D decimated Int-HWT: dimensional normalization procedure.

process) the original values are restored level by level, starting from the coarsest resolution level of the transformation, combining the wavelet and scaling coefficients from the level immediately below. Therefore, the 1D HWT is completely reversible, allowing the exact data reconstruction in each level of the transformation, until the end of the process is achieved, when the finest resolution level is finally reconstructed.

The normalized inverse 1D HWT also avoids computation of $\sqrt{2}$ by performing the non-normalized inverse transform, but this time a denormalization step is executed before the inverse transform begins (Figure 4). The interval extension for composition and its step procedure (Figure 5) is similar to the decomposition, being characterized also by the convolution of the vectors by filters. The number of operations of the $Composition$ procedure is $n \cdot \log(n)$.

The denormalization step, also shown in Figure 4, is very similar to the $Normalization$ algorithm, performing n operations. The difference is at line 6, where each coefficient is divided by the normalization factor, preparing the data for the inverse transform. Therefore, the optimal composition has the same complexity as the original version, $\mathrm{O}(n \cdot \log(n))$, but its results are more exact due to the normalization step, avoiding the calculation of $\sqrt{2}$ in every iteration.

Composition $(C[1..n])$
1 $i \leftarrow 2$;
2 **while** $i < n$ **do**
3 | $CompositionStep(C[1..2i])$;
4 | $i \leftarrow 2i$;
5 **end**
6 $C \leftarrow C * \sqrt{[2;2]}$;

CompositionStep $(C[1..n])$
1 **for** $i \leftarrow 1$ ***to*** $n/2$ **do**
2 | $C'[2i-1] \leftarrow (C[i] + C[i+n/2])/\sqrt{[2;2]}$;
3 | $C'[2i] \leftarrow (C[i] - C[i+n/2])/\sqrt{[2;2]}$;
4 **end**
5 $C \leftarrow C'$;

Figure 5. Inverse 1D decimated Int-HWT: composition process to reconstruct $l = log_2 n$ levels.

3.2. 2D Decimated Int-HWT Simplification

The HWT can be extended for 2D vectors. According to the procedure described in [11], the fast algorithm for the 2D decimated HWT is obtained through the application of the 1D transformation per direction (in all rows of the input matrix and after that, in all columns of the resulting one). In fact, the order how the many levels of the 1D transformation are applied to the 2D data generates different intermediate results and, therefore, distinct algorithms for the 2D transform. Following what was presented in [11], the 2D decimated Int-HWT can be calculated through the *Standard* formulation. In this formulation, an input matrix with $n \times n$ entries is initially decomposed in $L = log_2 n$ levels by the 1D transform, applied to all its rows. After the L decomposition levels of the 1D HWT were applied to the entire set of rows, the same 1D procedure is applied to the columns to the resulting matrix (already containing transformed data), as many levels as done for the rows.

The simplifications implemented for the normalized version of the 2D decimated int-HWT consider the same principle presented in the 1D case. The same strategy of multiplying the transformed values with respect to non-normalized filters by the corresponding $2^{-j/2}$ normalization factor is employed, where j is the corresponding level. The 1D transform is applied to all rows and columns of the input matrix in order to compose or decompose a matrix. However, according to [11], there is another well established algorithm for composition and decomposition of matrices, known as the *Non-Standard* procedure.

In this case, once one level of the 1D HWT is performed per rows, before considering the next level, the 1D HWT is applied to the columns. This procedure produces completely different decomposition sets of the input matrix from those obtained by the *Standard* formulation. As a consequence, *Standard* and

Non-Standard 2D HWT suggest distinct normalization procedures to allow their optimized interval extensions. During the study of the original algorithms [11], patterns of normalization factors were recognized. These patterns were analyzed and employed in the development of the normalization procedures for both algorithms, assuming the decimated version of the 1D HWT as the starting point.

These patterns are illustrated in Figure 6, in which three decomposition levels are presented for 8x8 matrices. The parameters j' and j'' indicate the normalization levels. The rule to calculate these normalization factors is described as follows:

$$2^{-(j'+j'')/2},$$

where $0 \leq j', j'' \leq (\log_2 n) - 1$ and n indicates the matrix order.

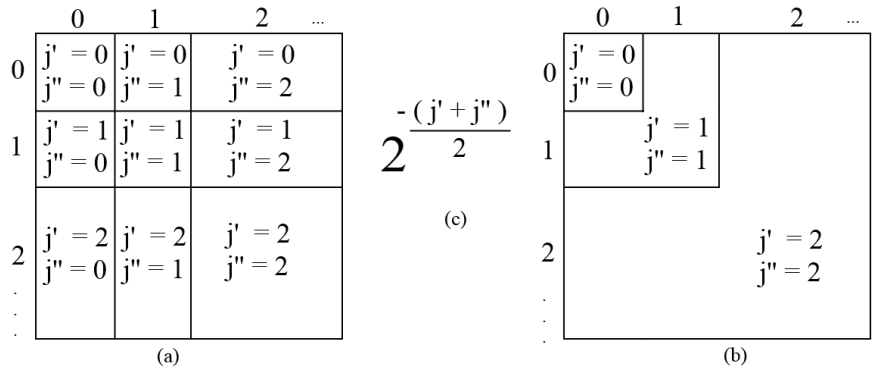

Figure 6. Scheme for the normalization patterns of the 2D decimated Int-HWT: (a) standard, (b) non-standard formulation and (c) rule for normalization factors.

Analysis of the original standard algorithm in Figure 7 shows that it depends on the original normalized decomposition procedure, whose amount of operations is $n \cdot \log(n)$, executing it for every row and column of the input matrix. Considering a $n \times n$ matrix, the number of operations in the original standard algorithm is $n \cdot (n \cdot \log(n) + n) + n \cdot (n \log(n) + n)$, therefore $\mathrm{O}(n^2 \cdot \log(n))$. Performing the non-normalized decomposition algorithm, discussed in Section 3.1, it reduces the calculations by avoiding intermediate normalization steps.

The non-normalized standard decomposition is performed with $2n^2 \cdot \log(n)$, and the last step is to normalize the results using the $Standard-$

```
Standard (C[1..h, 1..w])
for row ← 1 to h do
    Decomposition(C[row, 1..w]) ;
end
for col ← 1 to w do
    Decomposition(C[1..h, col]) ;
end
```

```
Non-Standard (C[1..h, 1..w])
C ← C/h ;
while h > 1 do
    for row ← 1 to h do
        DecompositionStep(C[row, 1..w]) ;
    end
    for col ← 1 to w do
        DecompositionStep(C[1..h, col]) ;
    end
end
```

Figure 7. 2D decimated HWT: standard and non-Standard decomposition processes.

```
StandardNormalization (C[1..h, 1..w])
Levels ← log2(h) ;
for LevelR ← 1 to Levels do
    StartR ← 2 ∧ LevelR ;
    EndR ← 2 ∧ (LevelR + 1) ;
    for Row ← StartR to EndR do
        for LevelC ← 1 to Levels do
            StartC ← 2 ∧ LevelC ;
            EndC ← 2 ∧ (LevelC + 1) ;
            for Col ← StartC to EndC do
                Factor ← 2 ∧ ((LevelR + LevelC) / 2) ;
                C[Row][Col] ← C[Row][Col] ∗ Factor ;
            end
        end
    end
end
```

Figure 8. 2D decimated Int-HWT: normalization step for the standard decomposition process.

$Normalization$ algorithm, presented in Figure 8, and since it is operating one time on each coefficient of the input matrix, its complexity can be expressed by $\mathrm{O}(n^2)$. The number of operations for the non-normalized standard decomposition and the standard normalization steps can be expressed by $2n^2 \cdot \log(n) + n^2$, which is faster than the original normalized procedure by avoiding a second iteration of $\mathrm{O}(n^2)$ on the input matrix. The original non-standard algorithm (Fig-

ure 7) executes an intermediate normalization at line 1, dividing each coefficient by the order of the input matrix with complexity $\mathrm{O}(n^2)$. Considering a square matrix of order n, the rest of the algorithm operates in a $while$ loop which is executed $\log_2(n)$ times. For each $while$ loop there are two for loops also executing $\log_2(n)$ times, each one performing the $DecompositionStep$ algorithm ($\mathrm{O}(n)$) in portions of the input matrix, depending on the level of transformation.

The original non-standard decomposition is executed in $n^2 + 2 \cdot \log(2 \cdot \log(n))$ operations. The non-normalized, non-standard decomposition ($\mathrm{O}(\log(n))$) does not require the normalization step, and its $Non - StandardNormalization$ algorithm (Figure 9) is performed with complexity $\mathrm{O}(n^2)$.

```
   NonStandardNormalization (C[1..h, 1..w])
 1 Levels ← log2(h) ;
 2 for i ← Levels to 1 do
 3 |   Factor ← 2 ∧ i ;
 4 |   Start ← Factor ;
 5 |   End ← 2 ∧ i + 1 ;
 6 |   for Row ← 1 to End / 2 do
 7 |   |   for Col ← Start to End do
 8 |   |   |   C[Row][Col] ← C[Row][Col] / Factor ;
 9 |   |   end
10 |   end
11 |   for Row ← Start to End do
12 |   |   for Col ← 1 to End do
13 |   |   |   C[Row][Col] ← C[Row][Col] / Factor ;
14 |   |   end
15 |   end
16 end
```

Figure 9. 2D decimated Int-HWT: normalization step for the non-standard decomposition process.

The overall number of operations of these procedures is $(n^2+\log(2\cdot\log(n))$, which is the same as the original normalized non-standard algorithm. The gain of time presented in Figure 21 is obtained by avoiding divisions by $\sqrt{2}$, a more expensive operation. The original normalized standard composition (i.e. the 2D inverse HWT assuming normalized filters and standard formulation), shown in

Figure 10, may be analyzed in the same way as its decomposition procedure. It performs the same number of operations and although both versions have complexity $BigO(n^2 \cdot \log(n))$, the original version is executed in $2n^2 \cdot \log(n) + 2n^2$ operations, while its optimized version requires only $2n^2 \cdot \log(n) + n^2$ operations.

```
InverseStandard (C[1..h, 1..w])
1 for row ← 1 to h do
2 |  Composition(C[row, 1..w]) ;
3 end
4 for col ← 1 to w do
5 |  Composition(C[1..h, col]) ;
6 end
```

```
InverseNon-Standard (C[1..h, 1..w])
1 while h > 1 do
2 |  for row ← 1 to h do
3 |  |  CompositionStep(C[row, 1..w])
4 |  end
5 |  for col ← 1 to w do
6 |  |  CompositionStep(C[1..h, col]) ;
7 |  end
8 end
9 C ← C ∗ h ;
```

Figure 10. 2D decimated HWT: composition process (a) standard formulation, and (b) non-standard formulation.

3.3. 1D Undecimated Int-HWT Simplification

Another alternative version for the HWT is the undecimated approach, which avoids the decimation operation after the convolution with the filters is computed. This undecimated transform has one well established formulation, called the *à trous* algorithm, which is considered in many astrophysical and statistical applications [12, 13], specially for been a translation invariant transform.

The undecimated formulation generates, for all decomposition levels, two vectors of the same size as the original one, containing the scaling and the wavelet coefficients. The undecimated formulation can also be executed assuming normalized or non-normalized filters. In the current subsection both cases are addressed, and the corresponding interval extensions are proposed.

The normalized decomposition procedure for the undecimated version of the Int-HWT, either 1D or 2D, is executed in the same order as the optimization developed for the decimated version: first a non-normalized decomposition of the input vector C^0 is made, as illustrated in Figure 11 for the case of two decomposition levels.

Now, to compute the last position values of the decomposition vectors C^j

$$C^0 = [9 \quad 7 \quad 5 \quad 3] \quad \rightarrow \quad \begin{matrix} C^1 = [8 & 6 & 4 & 6] \\ D^1 = [1 & 1 & 1-3] \end{matrix} \quad \rightarrow \quad \begin{matrix} C^2 = [7 & 5 & 5 & 7] \\ D^2 = [1 & 1-1-1] \end{matrix} \quad \rightarrow \quad ...$$

Figure 11. 1D undecimated HWT: example of two decomposition levels, without normalization and periodic extension on the right boundary of the vectors $C^j, j = 0, 1, ...$

Decomposition $(Input[1..n], Levels)$
1 $Declare\ C[1..Levels][1..n]$;
2 $Declare\ D[1..Levels][1..n]$;
3 $Declare\ LastC[1..n] \leftarrow Input$;
4 **for** $j \leftarrow 1$ ***to*** $Levels$ **do**
5 $\quad DecompositionStep(C[j], D[j], LastC)$;
6 $\quad LastC \leftarrow C[j]$;
7 **end**
8 **return** C, D ;

DecompositionStep $(C[1..n], D[1..n], LastC[1..n])$
1 **for** $i \leftarrow 1$ ***to*** $n-1$ **do**
2 $\quad C[i] \leftarrow (LastC[i] + LastC[i+1])/\sqrt{[2;2]}$;
3 $\quad D[i] \leftarrow LastC[i] - C[i]$;
4 **end**
5 $C[i] \leftarrow (LastC[n] + LastC[0])/\sqrt{[2;2]}$;
6 $D[i] \leftarrow LastC[n] - C[n]$;

Figure 12. 1D undecimated Int-HWT: normalized decomposition algorithm.

and D^j, the finite dimensional input vector C^{j-1} has to be extended. One natural assumption is the cyclic periodic extension, in which $C^{j-1}_{n+1} = C^{j-1}_1$. After all levels of the transform are obtained, the normalization of all coefficients is performed by multiplying by the normalization factor $2^{j/2}$, where j is the resolution level of the coefficients through out the decomposition.

The number of operations for $DecompositionStep$ and $Decomposition$ procedures are $2 \cdot n + 2$ and $2 \cdot Levels \cdot n + 3$, respectively. Both are part of the original decomposition procedure, shown in Figure 12. As in the previous cases, by performing a non-normalized decomposition there is no need to execute divisions by $\sqrt{2}$ in the step procedure (pseudo-code shown in Figure 13), reducing the number of operations to $2n$ and $2 \cdot n \cdot Levels$ with the same $BigO(n)$ complexity as the original normalized transform.

```
DecompositionStep (C[1..n], D[1..n], LastC[1..n])
1 for i ← 1 to n − 1 do
2 |   C[i] ← (LastC[i] + LastC[i + 1]) / [2; 2] ;
3 |   D[i] ← LastC[i] − C[i] ;
4 end
5 C[i] ← (LastC[n] + LastC[0]) / [2; 2] ;
6 D[i] ← LastC[n] − C[n] ;
```

Figure 13. 1D undecimated HWT: non-normalized decomposition step, without algebraic simplification.

The procedure in Figure 14 performs the normalization step of all coefficients after the transform. In contrast with the decimated version, the undecimated approach deals with a set of vectors as result of the transform, and each one of the resultant vectors needs to be normalized individually. The normalization procedure multiplies each scalar coefficient by its normalization factor $2^{i/2}$ for each resultant vector from the transform, configuring $n \cdot Levels$ operations from line 1 to 5 of the pseudo-code. With the new set of scalar values, all wavelet coefficients are then recalculated configuring $Levels \cdot (n + 3) + 2$ operations from line 6 to 16, which can be simplified to $n \cdot Levels$. The total of execution cost in this procedure, from line 1 to 16, can be expressed as $2 \cdot n \cdot Levels$ operations.

By performing a non-normalized vector transform followed by the normalization procedure, the number of operations is $4 \cdot n \cdot Levels$, which is more expensive than the original normalized formulation. The gain obtained with the new implementation is on the exactitude of results by avoiding high number of divisions by $\sqrt{2}$ from the original $DecompositionStep$ algorithm, as shown in Figure 20. The composition process (inverse transform), presented in Figure 15, starts with C^L, the component with the scalar coefficients from the lowest level L, adding it with all wavelet vectors D^j, $j = L, L-1, ..., 1$, produced during decomposition (the addition here is done position by position).

In this sense, the inverse formultion of the undecimated transform avoids the convolution with filters, characterizing the main difference with respect to the decimated case. The complexity of this procedure is $\mathrm{O}(n \cdot Levels)$ and can be used for both normalized and non-normalized transformations.

```
   À-TrousNormalization
   (C[1..n], C'[1..Levels][1..n], D'[1..Levels][1..n])
 1 for i ← 1 to Levels do
 2 |   for j ← 1 to n do
 3 |   |   C'[i][j] ← C'[i][j] * 2 ∧ ((i/2)) ;
 4 |   end
 5 end
 6 LastC ← C ;
 7 NextC ← C'[1] ;
 8 for i ← 1 to Levels do
 9 |   D ← LastC − NextC ;
10 |   if i + 1 < Levels then
11 |   |   LastC ← C'[i] ;
12 |   |   NextC ← C'[i + 1] ;
13 |   end
14 end
```

Figure 14. 1D undecimated Int-HWT: normalization procedure.

```
   Composition (C[1..n], D[1..Levels][1..n])
1 Declare Result[1..n] ← C ;
2 for i ← 1 to Levels do
3 |   Result ← Result + D[i] ;
4 end
5 return Result ;
```

Figure 15. 1D undecimated HWT: composition algorithm (inverse transform).

3.4. 2D Undecimated Int-HWT Simplification

As done for the decimated case, the undecimated 2D HWT considers the same principle presented in the 1D optimization, i.e., the same strategy of multiplying the transformed values by the corresponding $2^{j/2}$ normalization factor, where j is the corresponding level. To decompose a matrix, the 2D implementation creates a set of matrices carrying scalar coefficients and another set of matrices to store wavelet coefficients. The procedure is expensive on both performing and storing the results. Applying the same idea used in previous implementations, it is possible to reduce the error involved in the process. In Figure 16 the original standard procedure is presented. It performs the decomposition of

every line and level of a $n \times m$ matrix, configuring $2 \cdot m \cdot n \cdot Levels$ operations. The analog procedure for all columns of the same matrix executes the same $2 \cdot n \cdot m \cdot Levels$ operations. The entire procedure can be expressed by $2{\cdot}m{\cdot}n{\cdot}Levels{+}m{\cdot}2{\cdot}n{\cdot}Levels$, which can be simplified to $4{\cdot}m{\cdot}n{\cdot}Levels$. The non-standard procedure executes the same amount of calculations, but intercalating the decomposition of rows and columns. Both standard and non-standard algorithms can be used in conjunction with $DecompositionStep$ shown in Figure 3, so the execution cost of operating the normalized and non-normalized methods are the same.

```
StandardDecomposition (Input[1..n][1..m], Levels)
1  Declare C[1..Levels * 2][1..n][1..m] ;
2  Declare D[1..Levels * 2][1..n][1..m] ;
3  Declare C'[1..Levels][1..n] ;
4  Declare D'[1..Levels][1..n] ;
5  for i ← 1 to n do
6  |  C', D' ← Decomposition(Input[i][1..m], Levels) ;
7  |  for j ← 1 to Levels do
8  |  |  C[j][n][1..m] ← C'[j][1..m] ;
9  |  |  D[j][n][1..m] ← D'[j][1..m] ;
10 |  end
11 end
12 for i ← 1 to m do
13 |  C', D' ← Decomposition(C[Levels][1..n][i], Levels) ;
14 |  for j ← Levels to Levels * 2 do
15 |  |  C[j][1..n][i] ← C'[j][1..n] ;
16 |  |  D[j][1..n][i] ← D'[j][1..n] ;
17 |  end
18 end
19 return C, D ;
```

Figure 16. Undecimated 2D HWT: standard matrix decomposition.

The next step in order to normalize the transformed values is to perform the $ATrousMatrixNormalization$ procedure (Figure 17) which is executes $4 \cdot n \cdot m \cdot Levels$ operations. Therefore, the optimized decomposition procedure performs $8 \cdot n \cdot m \cdot Levels$ operations, twice the cost of the original normalized formulation and same complexity $BigO(n \cdot m)$, considering $Levels$ as a con-

stant value. Nevertheless, our approach results in more exact values as shown in Figure 22.

```
À-TrousMatrixNormalization
(C[1..n][1..m], C'[1..Levels][1..n][1..m], D'[1..Levels][1..n][1..m])
1  for i ← 1 to Levels * 2 do
2  |  for j ← 1 to n do
3  |  |  for w ← 1 to m do
4  |  |  |  C'[i][j][w] ← C'[i][j][w] * 2 ∧ ((i/2)) ;
5  |  |  end
6  |  end
7  end
8  LastC ← C ;
9  NextC ← C'[1] ;
10 for i ← 1 to Levels * 2 do
11 |  D ← LastC − NextC ;
12 |  if i + 1 < Levels then
13 |  |  LastC ← C'[i] ;
14 |  |  NextC ← C'[i + 1] ;
15 |  end
16 end
```

Figure 17. Undecimated 2D Int-HWT: normalization procedure.

4. Interval Data Compression

This section presents the interval extension of compression procedures, another contribution of the current study. The main goal of compression procedures is to express an initial data set with the smallest amount of points as possible, and this task can be done either with or without loss of information [11, 32].

In the wavelet context, the wavelet expansion of the initial data is analyzed to decide the most significant wavelet coefficients, comparing them with a threshold value. The truncated series without the least significant coefficients represents the compressed (or filtered) data. In many signal analysis applications, the significant wavelet coefficients can be used to draw conclusions. For example, in [33] micro-calcifications in mammograms were detected based on

the truncated wavelet representation of the images. In [34], ECG signals were analyzed assuming adaptive compression techniques.

The coefficient significance is judged by a threshold strategy, i.e. an heuristic to select the threshold value. There are many options, such as the Universal threshold value proposed by [35] which considers one single threshold value to be compared with all wavelet coefficients in all decomposition levels. Adaptive strategies to define the threshold value, such the one proposed in [36], are attempts to define threshold values depending on the analyzed coefficients, and therefore producing approximations closer and more coherent to the original data. For a review about the many possibilities for choosing threshold values see [32] and the references therein.

By discarding (excluding) non significant wavelet coefficients from the wavelet expansion, this strategy turns the method into a lossy compression procedure. This procedure is called hard thresholding [35]. When the wavelet coefficients are also smoothed by the threshold value, the strategy is called soft thresholding [35].In Figure 18, an example presented in [11] shows a sequence of approximations, generated by varying the compression rate $\frac{s}{N}$, where s is the number of significant coefficients, and N the total amount of points in the initial data representation. The criteria of selecting the m wavelet coefficients with the largest modulus is called the m-Best approximation procedure[11].

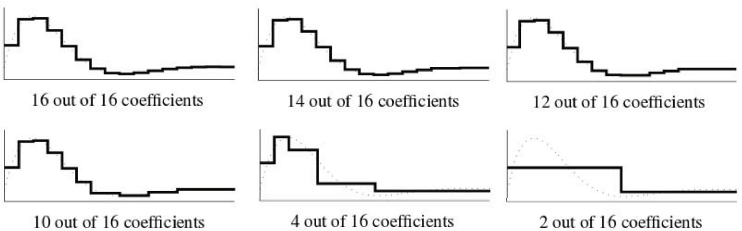

Figure 18. Approximation of functions after compression. Source: [11].

The hard thresholding is trivial for punctual data, but it cannot be applied in the same way to interval information. The punctual algorithm uses a real value τ as the threshold value, and the decision of which details must be ignored is a set of simple punctual comparisons.

When dealing with interval data, τ turns to be also an interval, carrying the error in the threshold calculus. In this way, the truncation decision cannot be evaluated with the same punctual comparison as before [1]. Since interval com-

pression demands extra computations than punctual compression, the strategy considered to manage two solutions which overcome computational cost preserve automatic validation and correctness code. The first one is named Hard Decision and the second one Soft Decision, both inspired on the hard and soft threshold operators defined by [35]. The Hard Decision tests if the interval data

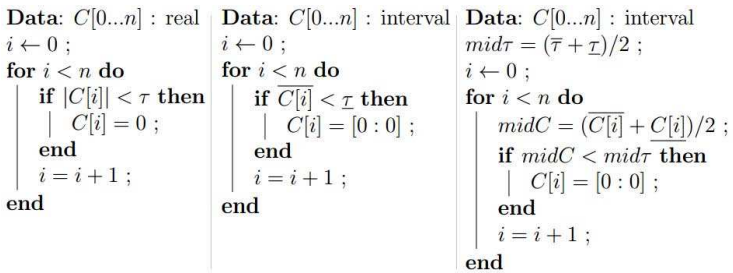

Figure 19. Hard Thresholding, Hard Decision, and Soft Decision compression procedures.

is entirely less than τ, comparing the left bound of the information and the right bound of the threshold. This procedure grants that every possible punctual coefficient is less than all possible punctual values belonging to τ. The Soft Decision verifies if most of the interval data is less than the midpoint of the interval τ, comparing the left bound of the information and the center of the threshold interval. This procedure grants that most possible punctual coefficients are less than the midpoint of $\overline{\tau}$ and $\underline{\tau}$.

5. Tests and Results

The numerical validation of algorithms proposed and described in Section 3 is based on the application of the HWT for image processing. In this way, interval parameters are obtained from punctual values setting degenerated intervals and using them as input to the interval extensions of both decimated and undecimated implementations of the HWT. The implementation of interval procedures in the Int-HWT library performs the computation of interval error in the process, presenting the widest interval diameter contained in the transformation results. For all tests, each function was executed 30 times, from which mean and standard deviation values for execution time were calculated. Standard deviation was less than 5% of average in the worst case.

In order to compute tests using the 1D HWT and its interval extension, a vector filled with $1,048,576$ random values is used as input. For tests using 2D HWT algorithms, the input is generated from a 1024×1024 matrix of random values, configuring the same $1,048,576$ values. The tests were executed on an Intel ® Core ™ i7 950 Processor @ 3.07GHz, 6GB RAM DDR3 at 1066MHz, Windows 10, compiled using Microsoft Visual C++ Compiler for Visual Studio s2013 on x64 Release. For each HWT, performance, accuracy, and metrics of Euclidean distance (EUC), Mean Square Error (MSE) and Peak-to-Noise Ratio (PSNR) were compared with results from the literature and their improvement or loss is presented in percentage. Such comparison is performed over diameters of such interval results in order to obtian their error analysis.

Thus, the corretness of HWT algorithms can be achieved by establishing that the result of interval computations contains all values of the related punctual computations. The interval metrics presented in Eqs.(5), (7) and (9) are applied in order to obtain the result intervals, which are compared based on usual order in $\mathbb{I}_{[a,b]}$.

5.1. Results for 1D HWT

Results of both decomposition and composition procedures for decimated and undecimated 1D HWT with the algorithms from [11] are presented in Figure 20a. Performance improvements for the decimated 1D HWT range from 36.8 to 51.8%. For the undecimated 1D HWT, performance loss was 52% for decomposition and 32% for both operations. Composition showed a slight improvement in performance.

The accuracy gain ranges from 95% up to 99.8% for the decimated case, meaning that the developed algorithms generate more exact results when compared to those from the literature. Euclidean Distance (EUC) and Mean Square Error (MSE) presents a gain of 99.8%, and Peak-to-Noise Ratio (PSNR) shows 24.4% of gain. The undecimated formulation adds no error to calculations on the composition step, considering that the input does not contain errors, which explains the lack of bars in Figure 20b. The accuracy gain when performing the combination of both decomposition and composition is around 81%. The EUC is about 54.5%, and MSE is 79.3%, while PSNR is 2.15%. These results show that, despite the loss of performance, the developed algorithms are more accurate than those related in [12].

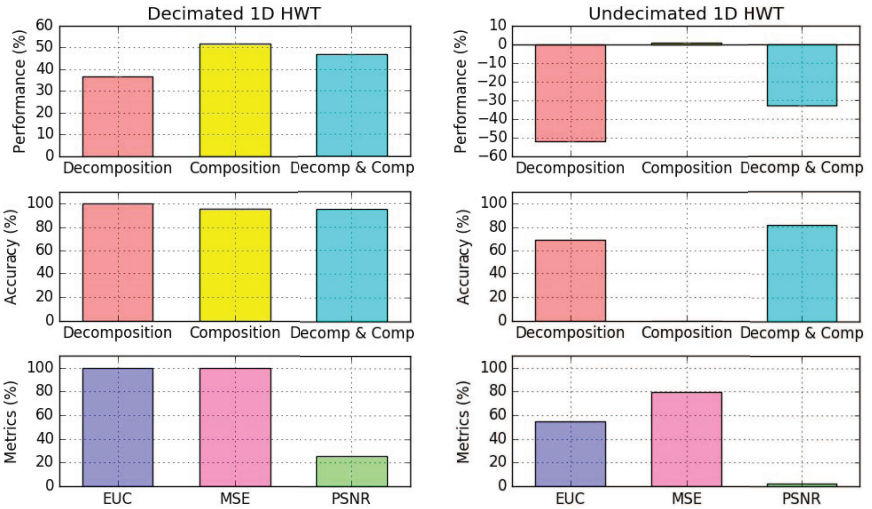

(a) Decimated 1D HWT (b) Undecimated 1D HWT

Figure 20. Performance, accuracy, and metric gains for the 1D HWT.

5.2. Results for 2D HWT

Figure 21 shows results for both standard and non-standard approaches for the decimated 2D HWT. The results presented in Figure 21a show a performance boost of 58.1% during the composition step. The accuracy gain of decomposition, composition and the combination of both are 99.8%, 93.5% and 98.3%, meaning that the results provided from the developed algorithms are more exact than results from the literature [11]. The EUC, MSE and PSNR metrics are 99.8%, 99.9% and 19.2% better respectively, showing that the developed algorithms are more accurate. Figure 21b shows the performance, accuracy and metric gains for the decimated 2D non-standard HWT comparing to the original algorithms found in [11]. As shown in Figure 6, the developed non-standard method avoid calculating $\sqrt{2}$ by algebraic simplifications. Therefore, the corresponding calculations do not increase the error during this process, indicated by accuracy values at 100% for all three methods. Due to the lack of error, the EUC and MSE are also shown at 100%. The PSNR metric cannot be calculated due to division by 0, since it uses MSE as divisor and its value is 0.

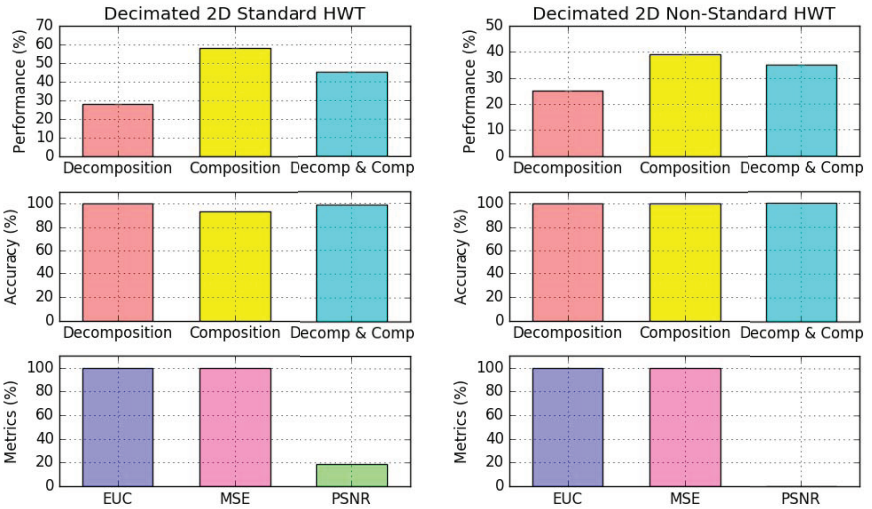

(a) Decimated 2D Standard HWT (b) Decimated 2D Non-Standard HWT

Figure 21. Execution Times and error measurements for the 2D HWT using 2^{10} x 2^{10} matrix with random values.

5.3. Comparison of Standard and Non-Standard Approaches

Figure 22 shows the results for both standard and non-standard approaches for the undecimated 2D HWT. Performance is shown in Figure 22a and Figure 22b indicates that the developed algorithms are at least 10% slower than the originals, despite the composition step having a little advantage of 5% on the standard method. Nevertheless, both approaches present accuracy gains, 92.6% for decomposition and 87.4% for the combination of both algorithms performing together. The EUC, MSE and PSNR of both approaches are roughly 51%, 76% and 2% respectively.

Conclusion

The current work presents interval extensions of the 1D and 2D HWT, for both decimated and undecimated approaches, normalized and non-normalized versions, covering the most studied formulations for the Haar transform. The error analysis is compatible based on the time complexity of the algorithms. Accu-

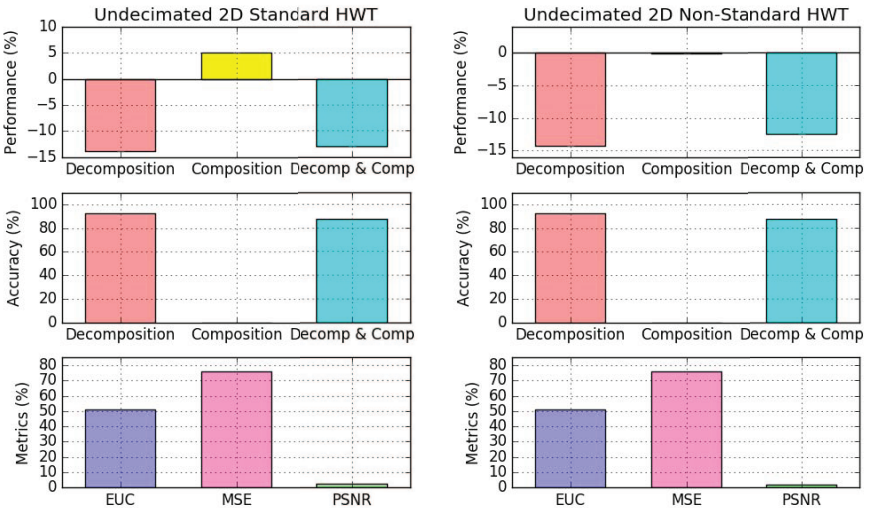

(a) Undecimated 2D Standard HWT (b) Undecimated 2D Non-Standard HWT

Figure 22. Execution times and error measurements for the 2D HWT using 2^{10}x 2^{10} matrix with random values on 4 levels of decomposition.

racy is improved through the proposed algebraic optimizations obtained for the normalized versions of the transforms. As a consequence of the implemented optimizations, our algorithms designed for interval arithmetic are faster than the original decimated formulations, but slower than the original undecimated algorithm, presenting in all scenarios an increase in accuracy.

The task of data compression in the wavelet context is also stressed. Two interval extensions are designed, the Hard and the Soft Decision procedures, allowing an entire new branch of applications to be treated in the interval context. In addition, the precision gains obtained with the proposed simplifications represent a significant contribution to the research area. Further research considers the study of the DWT together with corresponding parallel and/or distribution Int-DWT library extension, by making use of massive parallel architectural of GPUs and considering CUDA programming language.

Acknowledgments

Fundings: CNPq PQ-2 grant 309533/2013-9; FAPERGS grant PqG 2014; FAPERGS PQG 1873-2551/13-0; MCTI/CNPq grant Universal 14/2014 B 448766/2014-0; CAPES/Brazil Ph.D. and project grants.

References

[1] R. Moore, *Methods and Applications of Interval Analysis*, SIAM, Philadelphia, 1979.

[2] M. Shu-li, L.Qi-shao, Z. Sen-wen, J. Li, Adaptive interval wavelets precise integration method for partial differential equations, *Applied Math. and Mech.* 26 (3) (2005) 364–371.

[3] L. Liu, Interval wavelet numerical method on Fokker-Planck equations for nonlinear random systems, *Advances in Mathematical Physics* 2013 (ID 651357) (2013) 1–7.

[4] W. S. Lee, A. A. Kassim, Signal and image approximation using interval wavelet transform, *IEEE Trans. Image Processing* 16 (1) (2007) 46–56. doi:10.1109/TIP.2006.884950.
URL `http://dx.doi.org/10.1109/TIP.2006.884950`

[5] T. Minamoto, K. Aoki, A blind digital image watermarking using interval wavelet decomposition, Int. *Journal of Signal Proc., Image Proc. and Pattern Recognition* 3 (2) (2010) 59–72.

[6] M. B. H. Om, An improved image denoising method based on wavelet thresholding, *J. of Signal and Inf. Processing* 3 (2012) 109–116.

[7] M. Kumar, S. K. Sudhansu, V. Kasabegoudar, Wavelet based texture analysis and classification with linear regration model, *Intl. J. of Eng. Research and App. (IJERA)* 2 (2012) 1963–1970.

[8] I. Y. Novikov, M. A. Skopina, Why are Haar bases in various structures the same?, *Math. Notes – Short Comm.* 91 (6) (2012) 895–898.

[9] A. Brito, O. Kosheleva, Interval + image = wavelet: for image processong under interval uncertainty, wavelets are optimal, *Reliable Computing* 4 (1998) 291–301.

[10] V. dos Santos, M. Pilla, R. Reiser, A. Kozakevicius, Int-haar: Intervalar extension of the Haar transform, in: *Regional School on High Perf. Comp.* (ERAD 2013, in Portuguese), SBC, Brazil, 2013, pp. 167–170.

[11] E. J. Stollnitz, T. D. DeRose, D. H. Salesin, Wavelets for computer graphics: A primer, part 1, *IEEE Comp. Graphics and App.* 15 (3) (1995) 76–84.

[12] J.-L. Starck, J. Fadili, F. Murtagh, The undecimated wavelet decomposition and its reconstruction, in: *IEEE Trans. on Image Proc.*, Vol. 16, 2007, pp. 297–309.

[13] A. Kozakevicius, A. A. Schmidt, Wavelet transform with special boundary treatmentfor 1d data, *Comp. Appl. Math* 1 (2013) 1–15.

[14] R. E. Moore, Automatic error analysis in digital computation, *Tech. Rep.* LMSD-48421, Lockheed Aircraft Corporation (1959).

[15] R. E. Moore, *Interval arithmetic and automatic error analysis in digital computing*, Ph.D. thesis, Dept. of Math., Stanford University, Stanford (1962).

[16] W. Tucker, *Validated Numerics: A Short Introduction to Rigorous Computations*, Princeton Univ. Press, New Jersey, 2011.

[17] G. Walster, *Interval arithmetic: The new floating-point arithmetic paradigm*, Tech. rep., Sun Microsystems (Oct. 1997).

[18] T. Hickey, Q. Ju, M. V. Emdem., Interval arithmetic: From principles to implementation, *J. of the ACM* 48 (5) (2001) 1038–1068.

[19] L. H. Figueiredo, J. Stolfi, Affine arithmetic: Concepts and applications, *Numerical Algorithms* 37 (2004) 147–158.

[20] R. H. N. Santiago, B. R. C. Bedregal, B. M. Acióly, Formal aspects of correctness and optimality of interval computations, *Formal Aspects of Correctness and Optimality of Interval Computations* 18 (2) (2006) 231–243. doi:10.1007/s00165-006-0089-x.
URL `https://doi.org/10.1007/s00165-006-0089-x`

[21] R. M. P. Trindade, B. R. C. Bedregal, A. ao Duarte Doria Neto, B. M. Acióly, An Interval Metric, *New Advanced Technologies*, InTech, 2010.

doi:10.5772/9424. URL https://www.intechopen.com/books/new-advanced-technologies/an-interval-metric

[22] F. L. Santana, R. H. N. Santiago, A generalized distance based on a generalized triangle inequality, *Information Science* 345. URL https://doi.org/10.1016/j.ins.2016.01.058

[23] C-XSC. URL http://www2.math.uni-wuppertal.de/~xsc/xsc/cxsc.html

[24] Pblas (Parallel Basic Linear Algebra Subprograms). URL http://www.netlib.org/scalapack/html/pblas_qref.html

[25] M. Kolberg, L. G. Fernandes, D. Claudio, Dense linear system: A parallel self-verified solver, *Intl. J. of Parallel Programming* 36 (2008) 412–425.

[26] C. R. Milani, M. L. Kolberg, L. G. Fernandes, Solving dense interval linear systems with verified computing on multicore architectures, in: *High Perf. Comp. for Comp. Science - VECPAR* 2010, Berkeley, CA, 2010, pp. 435–448, revised Selected Papers.

[27] A. Haar, Zur theorie der orthogonalen funktionensysteme, *Mathematische Annalen* 69 (3) (1910) 331–371. doi:10.1007/BF01456326. URL http://dx.doi.org/10.1007/BF01456326

[28] I. Daubechies, Ten Lectures on Wavelets, *CBMS-NSF Regional Conference Series in Applied Mathematics*, SIAM, Philadelphia, 1992.

[29] C. Christopoulos, A. Skodras, T. Ebrahimi, The JPEG2000 still image coding system: an overview, Consumer Electronics, *IEEE Transactions* on 46 (4) (2000) 1103–1127.

[30] V. dos Santos, M. Pilla, R. Reiser, A. Kozakevicius, Int-haar: Improving precision of the haar interval wavelet extension, in: *Workshop-School on Theoretical Computer Science (WEIT 2013)*, IEEE CS, Rio Grande, Brazil, 2013, pp. 92–96. doi:10.1109/WEIT.2013.16.

[31] J. Rohn, *A handbook of results on interval linear problems*, Prague: Czech Academy of Sciences, Czech Republic, 2005.

[32] A. J. Kozakevicius, F. M. Bayer, Signal denoising via wavelet coefficients thresholding, *Ciéncia & Natura*, Special Issue 1 (2014) 37–51.

[33] M. Asadzadeh, E. Hashemi, A. Kozakevicius., On efficiency of combined Daubechies wavelets and statistical parameters applied in mammography., *Applied and Computational Mathematics* 12 (3) (2013) 289–306.

[34] G. Perin, A. J. Kozakevicius, Filtragem wavelet de sinais cardacos atravás de algoritmos adaptativos, *RITA* (in Portuguese) 20 (3) (2013) 95–111.

[35] D. Donoho, De-noising by soft-thresholding, *IEEE Trans. on Infor. Theory* 41 (1995) 613–627.

[36] F. M. Bayer, A. J. Kozakevicius, Spc-threshold: a limiar proposal for adaptative signal filters, *Tendences in Applied and Computational Mathematics* (in Portuguese) 11 (2) (2010) 121–132.

In: Wavelets: Principles, Analysis and Applications ISBN: 978-1-53613-374-5
Editor: Joseph Burgess

Chapter 3

WAVELET ANALYSIS AS A TOOL FOR CHARACTERIZING TRENDS IN CLIMATIC DATA

F. Colombo[1,2], S. Magazù[1,3] and M. T. Caccamo[1,3]
[1]Dipartimento di Scienze Matematiche e Informatiche,
Scienze Fisiche e Scienze della Terra,
Università di Messina, Messina, Italy
[2]Italian Air Force Meteorological Service,
Comando Aeroporto – Sigonella, Catania, Italy
[3]Istituto Nazionale di Alta Matematica "F. Severi" – INDAM –
Gruppo Nazionale per la Fisica Matematica – GNFM, Rome, Italy

Abstract

Wavelet transform is an effective mathematical tool able to provide a time–frequency representation of signals defined in the time domain. So far this innovative multiscale analysis has been successfully applied in various fields of science, such as, for example, geophysics, astrophysics, telecommunications and climatology. In this chapter the wavelet analysis is employed to analyse Sicily temperature data. Sicily represents one of the hot spot for the study of climate change in the Mediterranean area, because of its vulnerability to desertification processes. Precipitations and temperature trends forecasted for the XXI century by Regional Climate Models (RCM) show an increasing temperature trend and a non-clear precipitation trend. To better characterize the temperature trend, the 1865-2016 temperature time

series of Palermo and the 1962-2014 time series of four Sicilian localities have been analysed by means of Continue and Discrete Wavelet Transforms. Such analyses allow to identify the fast and slow events contained in the time series and to identify the major features of the Sicilian climate dynamics.

Keywords: wavelet analysis, climatic data, trends, anomalies, temperature

Introduction

The increasing of temperatures and the intensification of the hydrologic cycles are the most evident effects caused by climate change in the Mediterranean basin. One of the most significant consequences of temperature increase and of changes in precipitations is the dramatic modification of hydrologic regimes. During the last 15 years an impressive series of extreme weather events occurred in different places of Sicily, producing damages and, in some cases, even victims.

For example, one can cite the following tragic sequence of severe meteorological events occurred between the years 2007 and 2011:

- 25th October 2007, which took place at Santa Margherita, Giampilieri and Scaletta (Messina), with flash flood and precipitations of 175 mm in 2 hours, against an annual average value of 800-1000 mm;
- 22nd November 2011 at Barcelona and Saponara (Messina) with precipitations of 351 mm in 10 hours (recorded by the Castroreale weather station);
- 01st October 2009 at Giampilieri; this latter was a tragic and disastrous event with 37 victims.

With reference to these three events, the recovery costs of the disaster damages were estimated to be about 900 million euros [1, 2].

These findings are in agreement with the predictions of the Mediterranean Regional Climate Model as shown in the report "The future climate of Italy: analysis of projections of regional models" [3]. The Model predicts that the accumulated yearly precipitations will slightly decrease, while the maximum rain rate is expected to increase in most of Italy, with the exception of Sicily. One more interesting parameter is the forecast of the maximum number of

days without rain: it will increase from 5 to 40% respect the average 1971-2000. It is therefore not surprising that many of the arguments concerning both climate variability and climatic change are directly related to the detection of trends in hydro-climatic parameters, such as temperature and precipitation [4]. One way to accomplish trend assessments is through time-series analysis. Wavelet analysis offers several advantages in respect to Fourier Transform or Windowed Fourier Transform analysis, these latter using a single analysis window. The main problem with the fixed window used in the Windowed Fourier Transform is that it loses the time localization at high frequencies when the window is sliding along the time series because there are too many oscillations captured within the window. It also losses the frequency localization at low frequencies because there are only a few low-frequency oscillations included in the window [5-7]. The wavelet transform can handle these issues by decomposing a one-dimensional signal into two-dimensional time–frequency domains at the same time [8-11]. Wavelets are usually irregular and asymmetric in shape and this property makes a wavelet ideal for analysing signals that contain sharp changes and discontinuities [12-15]. Wavelet transforms use different window sizes, which are able to compress and stretch wavelets in different scales used to decompose a time series. Narrow windows are used to track the high-frequency components or rapidly changing events of the analysed signals (which are represented by the lower detail levels), whereas wider window sizes are used to track the signals' low-frequency components including trends (which are represented by the higher detail levels and the approximation component). Moreover, wavelet analysis is able to show many properties of a time series or data (such as trends, discontinuities, change points, and self-similarity) that may not be revealed by other signal analysis techniques. In summary, the wavelet transform is capable of analysing a wider range of signals more accurately when compared to the Fourier analysis [16-19]. The results of wavelet analysis can be used to determine the main components or modes that contribute to producing trends [11, 21, 22].

The main purpose of this study is to combine the use of the Discrete Wavelet Transform (DWT) technique and the Continues Wavelet Transform (CWT) in order to investigate trends, periodicities and singularities present in four datasets concerning the temperature of Sicily by analysing their monthly and annual time series collected from 1962 to 2014.

A Background on Wavelet

Any climate signal can be interpreted as a result of interactions between physical and dynamic processes that occur on a wide range of spatial and temporal scales. The scale of the processes involved extends into the space between a few meters and thousands of kilometres and in time in a few hours and millions of years [23]. To analyse such behaviour we need to use special mathematics tools. The wavelet analysis represents a powerful instrument to extract information from a time series. It can be used to analyse time series that contain non-stationary power at many different frequencies. In the case of meteorological and climatological series, this type of analysis is particularly appreciated because it is able to extract valuable information from the signal [24, 25]. For example, if compared to the simple Fourier transform, the wavelets analysis allows to find not only in the value of certain frequencies in a non-stationary series, but also to identify the time interval in which these frequencies are present and predominant. A wavelet function is a function having a wave shape and a limited but flexible length with a mean value that is equal to zero, and is localized in both time and frequency domains. Let consider a complex-valued function ψ satisfying the following conditions:

$$\int_{-\infty}^{\infty} |\psi(t)|^2 dt < \infty \tag{1}$$

$$C_\psi = 2\pi \int_{-\infty}^{\infty} \frac{|\Psi(\omega)|^2}{|\omega|} d\omega < \infty \tag{2}$$

where Ψ is the Fourier transform of ψ. The first condition implies finite energy of the function ψ, and the second condition, the admissibility condition, implies that if $\Psi_{(\omega)}$ is smooth then $\Psi(0) = 0$. The function ψ is the mother wavelet [26].

Wavelet transforms involve shifting forward the wavelet in a number of steps along an entire time series, and generating a wavelet coefficient at each step. This measures the level of correlation of the wavelet to the signal in each section. The variation in the coefficients indicates the shifting of similarity of the wavelet with the original signal in time and frequency. This process is then repeated for each scaled version of the wavelet, in order to produce sets of wavelet coefficients at the different scales. The lower scales represent the compressed version of the mother wavelet, and correspond to the rapidly changing features or high-frequency components of the signal. The higher

scales are the stretched version of a wavelet, and their wavelet coefficients are identified as slowly changing or low frequency components of the signal. Therefore, wavelet transforms analyse trends in time series by separating its short, medium, and long-period components [27]. WT can be performed using two approaches: Continuous Wavelet Transform (CWT) and Discrete Wavelet Transform (DWT). CWT operates on smooth continuous functions and can detect and decompose signals on all scales, while Discrete Wavelet Transform (DWT) operate on scale that have discrete numbers.

Figure 1. Geographic position of the four analysed weather station.

Site and Data Description

Sicily, being located in the centre of the Mediterranean, represents a privileged point of observation to study climate changes. Its climatic characteristics are able in fact to be considered with a good approximation, as representative of the whole Mediterranean basin. The choice of the data sets used in this work, has been done taking into account the geographic position of each station and its characteristics. All the selected weather stations are in fact very close to the sea coast, with a maximum altitude of 54 metre and, for this reasons, they can be considered as good indicators of the mean Mediterranean climate. The Palermo's temperature time series starts from 1865 and is the longest series

available in Sicily. The geographic positions and the characteristics of each station are shown in Figure 1 and in Table 1, respectively.

The Palermo and Messina weather stations are positioned inside the town; the Cozzo Spadaro weather station is located inside a lighthouse building in a small fisherman village, while the Trapani weather station is sited in the military airport located 12 kilometres far from the nearest city. In order to uniform and to compare the time series length for wavelet analysis, we have taken into account the longest common period, i.e., 1962-2014. During this time interval, Sicily had a great economic growth; the populations of the towns of Palermo and Messina increased and several new building have been built, beginning from early seventies. This anthropogenic change could affect the temperature signal, producing a higher increase in respect to the signals of Trapani and Cozzo Spadaro, where minor or no environment changes occurred since 1960. The monthly and annual temperatures of these four weather stations were analysed. The stations used in this study were chosen on the basis of completeness and length of their available record for the period of 1962-2014. This time interval is considered to be long enough to obtain valid statistics mean values in assessing the temperature trend [28]. Furthermore, Partal (2010) [29] considered 40-years data adequate for trend analysis studies. Moreover, although up to three-percent missing data is considered acceptable for meteorological studies [30], we chose only the stations with fully complete records over the chosen time period. This was done in order to avoid possible uncertainties associated with the computation of extrapolation procedures. Therefore, we concluded that having 53 years data is sufficient for the purpose of trend detection.

Table 1. Meteorological stations employed to record temperature and precipitation data

WMO ID	Station Name	Latitude (°)	Longitude (°)	Elevation (m a.s.l.)	Observation Period
16405	Palermo	38°07’00”	13°18’44”	36	1865-2015
16420	Messina	38°12’02”	15°33’11”	54	1962-2014
16480	Cozzo Spadaro	36°41’10”	15°07’57”	44	1952-2015
16429	Trapani-Birgi	37°54’50”	12°29’28”	4	1962-2014

Data Analysis

The temperature data sets of the four stations are composed by monthly and annual mean values. In addition, the temperature data set of Cozzo Spadaro weather station also contains the daily 12 UTC temperatures. In order to identify the trends, the conventional discrete wavelet analysis of signals was performed on each time series using the multilevel 1-D wavelet decomposition function in MATLAB. This produces the wavelet transform of the input data at all dyadic scales. The Mayer (dmey) wavelet was used in this study because the Meyer mother wavelet has two features that make them very useful in analysing temperature records: first, they are fairly smooth and second, they have limited frequency bands. The smoothness feature makes them more capable of detecting the smooth component of the signal. Moreover, smoother wavelets are preferred here because the trends are supposed to be gradual and represent slowly changing processes. Smoother wavelets should be better at detecting long-term time-varying behaviour (good frequency-localization properties) [31]. The finite frequency bandwidth enables them to detect and isolate the various periodic components of the record. For each monthly dataset, seven levels of decomposition were used. This number is based upon the number of data point, equal to 636 average monthly temperature, as well as the mother wavelet used. Decomposing the signals using specified filters (wavelet and scaling functions) produces two types of coefficients: the approximation or residual, and detail vectors [32, 33]. These coefficients resulted from the convolution of the original signal with a low-pass filter and a high-pass filter. The low-pass filter is the scaling function and the high-pass filter is the wavelet function. The convolutions of signals with the low-pass filter produced the approximation coefficients, which represent the large-scale or low frequency components of the original signal. Convolutions with the high-pass filter produced the detail coefficients, which represent the low-scale or high-frequency components [34, 35]. The data were also analysed by using the CWT in order to identify discontinuities, singular episode and periodicities contained in the signal. In this case, one of the most widely used continuous wavelet, a Morlet mother wavelet, was used. It consists of a plane wave modified by a Gaussian envelope [36]:

$$\psi_0(\eta) = \pi^{-1/4} e^{i\omega_0\eta} e^{-\eta^2/2} \tag{3}$$

where ω_0 is the nondimensional frequency, here taken to be 6 to satisfy the admissibility condition [37].

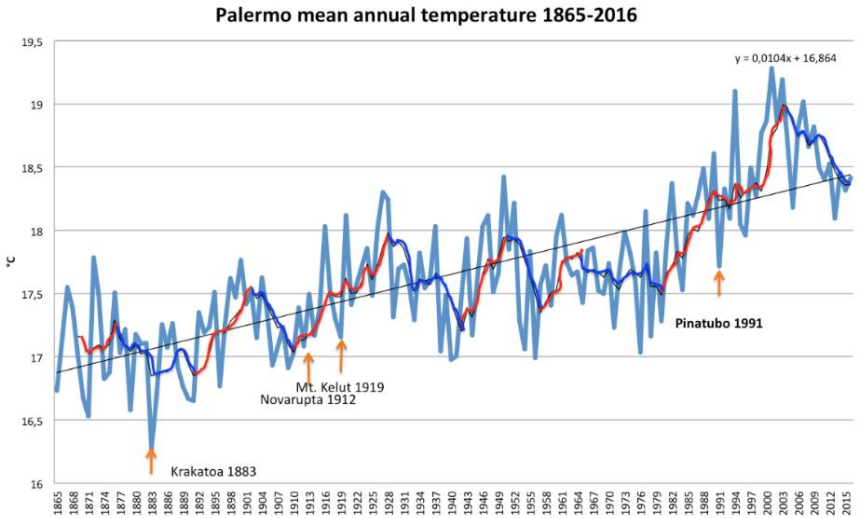

Figure 2. Palermo mean annual temperature data (blue curve); 5 years mean values (red and dark blue curves) and linear trend (black line). The orange arrows show the correspondence of negative peaks with the major volcanic eruptions occurred during the last 150 years.

Results and Discussion

The analysis of Palermo's annual mean temperature 1865-2016 graph (Figure 2) allow us to make some general considerations regarding the influence of the world biggest volcanic eruption on the temperature signal. Volcanic eruptions can inject into the stratosphere a huge volume of chemically and micro physically active gases and solid aerosol particles, which affect the Earth's radiative balance and climate and disturb the stratospheric chemical equilibrium. The resulting disturbance to the Earth's radiation balance affect surface temperatures trough directs radiative effect as well as trough indirect effects on the atmospheric circulation. In the analysed signal we found in fact the footprint of the Hearth's major volcanic eruptions occurred during the last 150 years. They are all remarked in the figure with an orange arrow in correspondence of the year of the eruption. The linear trend of temperature was also calculated and it was equal to 0,0104°C/years that means a total

temperature increase of 1,58°C for the whole period. The first analysis performed on Palermo longer time series of monthly temperature was a Discrete Wavelet Transform. The detail of reconstruction at level 9 is shown on Figure 3. It shows a positive trend of temperature with 2 main slopes: the first starts on 1870 and continue till 1910. A range of about 40 years in which the temperature stay about stationary before stating to increase again becoming from 1960 and continuing till 2010 follows it. The total amount of temperature increasing was about + 1,55°C on line with the value obtained using the linear regression.

After this result obtained for Palermo, we started to analyse the 53 years long temperature series for Messina, Palermo, Trapani and Cozzo Spadaro, respectively. For each data set a Discrete Wavelet Transform decomposition at level 7 and a Continuous Wavelet Transform was performed. For the DWT we used the temperature data sets, while for CWT, in order to eliminate the strong yearly periodicity, the temperature anomalies were calculated and used.

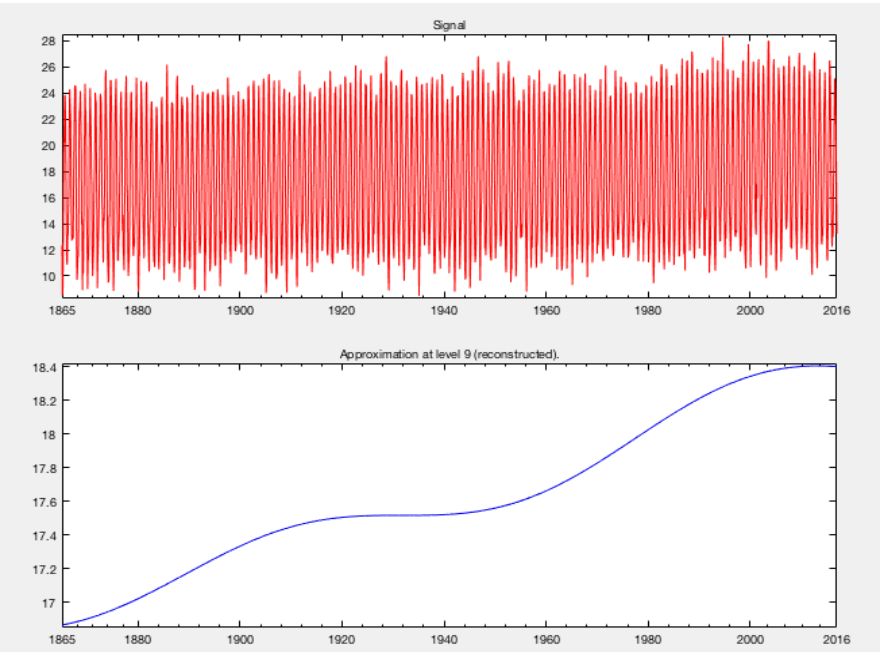

Figure 3. Palermo DWT signal (on the top) and approximation at level 9 (on the bottom) of the 1865-2016 mean monthly temperature values.

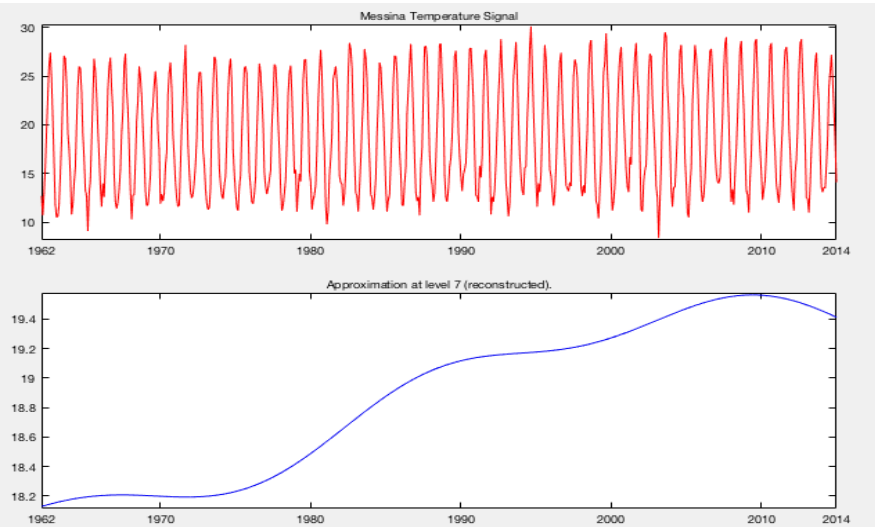

Figure 4. Messina DWT (on the top) and approximation at level 7 (on the bottom) of the 1962-2014 mean monthly temperature values.

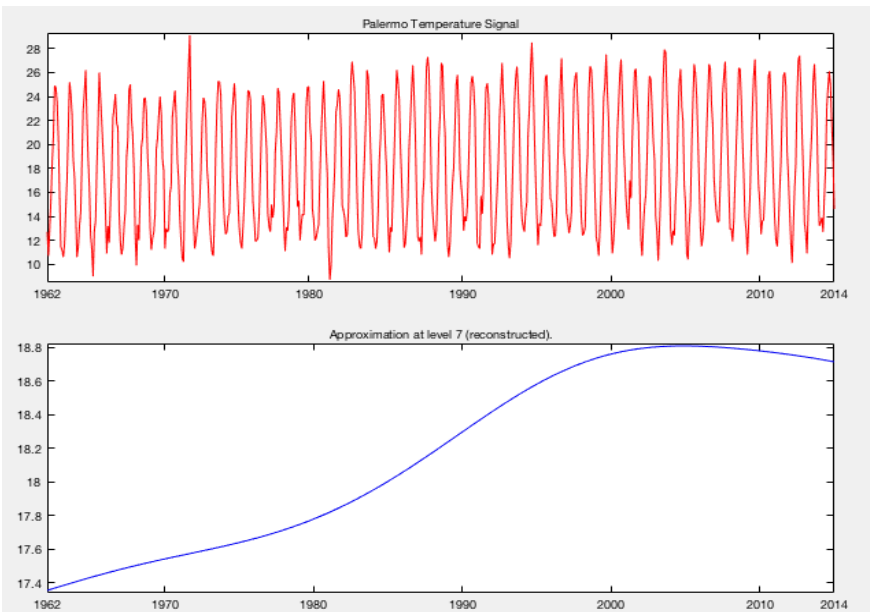

Figure 5. Palermo DWT data (on the top) and approximation at level 7 (on the bottom) of the 1962-2014 mean monthly temperature values.

Each signal shows some differences and some common trend characteristics. Messina, Palermo and Trapani show, for example, a decreasing trend during the last years. Palermo seems to reach the maximum temperature in 2005 while Messina and Trapani reach the maximum value in 2010, before that the temperature starts to decrease. Messina shows also an almost flat trend during the 1962-1975 time range and then a rapid up-slope till 1990, while Palermo and Trapani show a more regular trend. The Cozzo Spadaro trend is quite different; it is the only one that shows a negative trend from 1962 to 1978; moreover, it shows a continue temperature increase till the end of the signal. In Table 2 the minimum and maximum values reached, the difference and the increasing of temperature obtained subtracting the value of 2014 to the values of 1962, are shown.

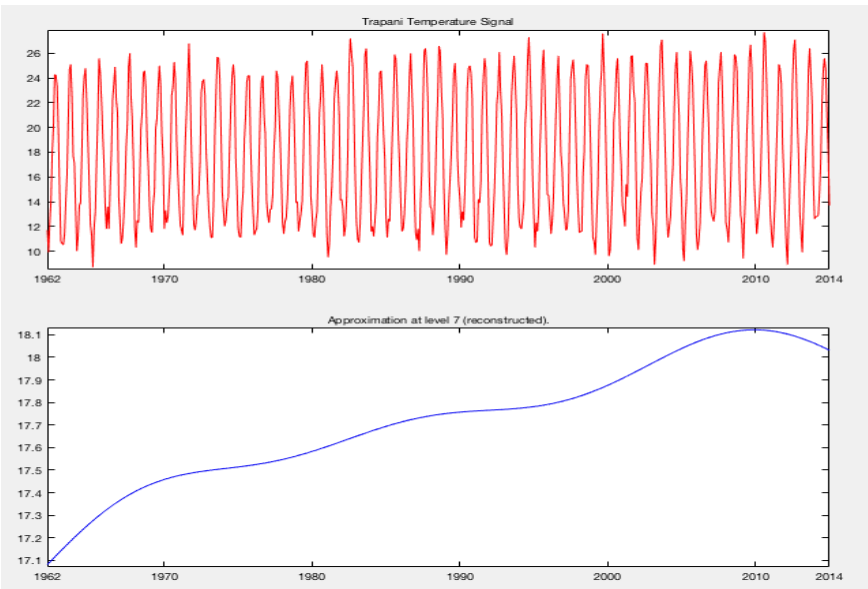

Figure 6. Trapani DWT data (on the top) and approximation at level 7 (on the bottom) of the 1962-2014 mean monthly temperature values.

A Continuous Wavelet Transform has also been performed on the mean monthly temperature anomaly of four time series using a Morlet mother wavelet. The anomaly was first calculated subtracting from the monthly mean temperature, the average monthly temperature of the 30 years 1971-2000. This operation cleans the signal of the strong annual frequency, making the CWT graph more readable.

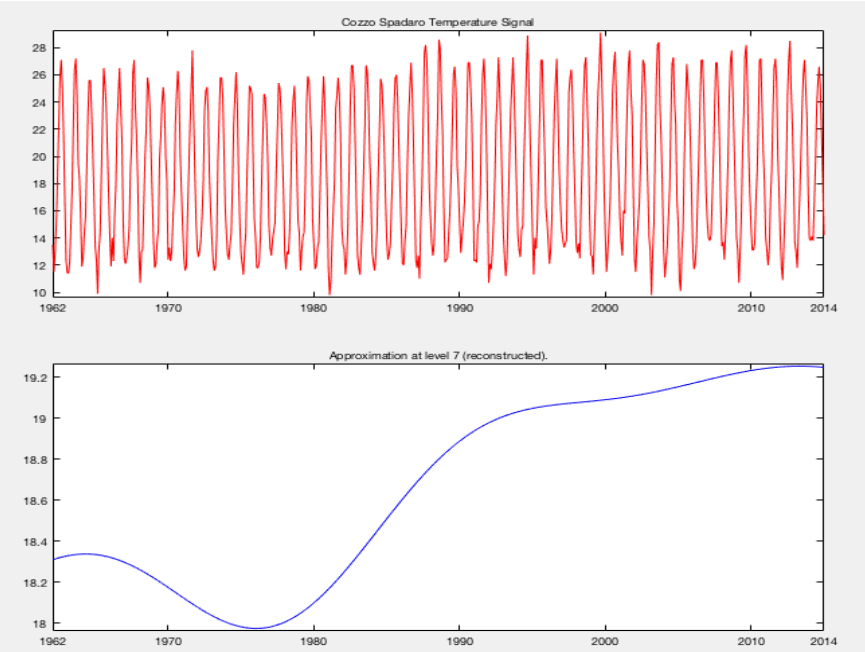

Figure 7. Cozzo Spadaro DWT data (on the top) and approximation at level 7 (on the bottom) of the 1962-2014 mean monthly temperature values.

Table 2. Minimum, Maximum, Max difference and temperature increase of each weather station

Weather Station	Minimum	Maximum	Max difference	Temperature increasing 1962-2014
Messina	18,13	19,56	1,435	+1,27°C
Palermo	17,35	18,81	1,453	+1,37°C
Trapani	17,08	18,12	1,041	+0,94°C
Cozzo Spadaro	17,98	19,25	1,278	+0,95°

Messina CWT shows the presence of periodicities longer than 2 years from 1980, when a 24-36 months signal started. It disappears around 1990. During these 10 years, an abrupt episode is present in 1987. At the same time,

a periodicity of about 60 month appears and continues till 2008, overlapped to a 36-month periodicity that finishes in 2010. A second strong singular episode is presents in 2003 (Figure 8). Palermo CWT graph also shows the absence of longer than 2 years periodicities from 1962 to 1980. Starting from these years a periodicity of 24 to 36 month appears and continues to be present until 2008. Two singular episodes are again visible in the graph in 1987 and in 2003. A longer periodicity of about 60 months appears in the graph in correspondence of the singular episode of 1987 and continues until 2012 (Figure 9).

Trapani CWT, as also seen for Messina and Palermo, maintains the same characteristics: absence of periodicities longer than 2 years till 1980 when a 24 to 36 months periodicity appears and continues until 1990. The point at 1987 shows a well-defined singularity, while a second one appears in 1999. Starting from this point a new periodicity of about 60 months appears and continues till 2010 (Figure 10). The CWT of Trapani contains also another important feature: the presence of a well-defined periodicity of about 128 months from 1962 to the middle of 1980s. This periodicity is typical of solar cycles and is more or less present also in the others CWT.

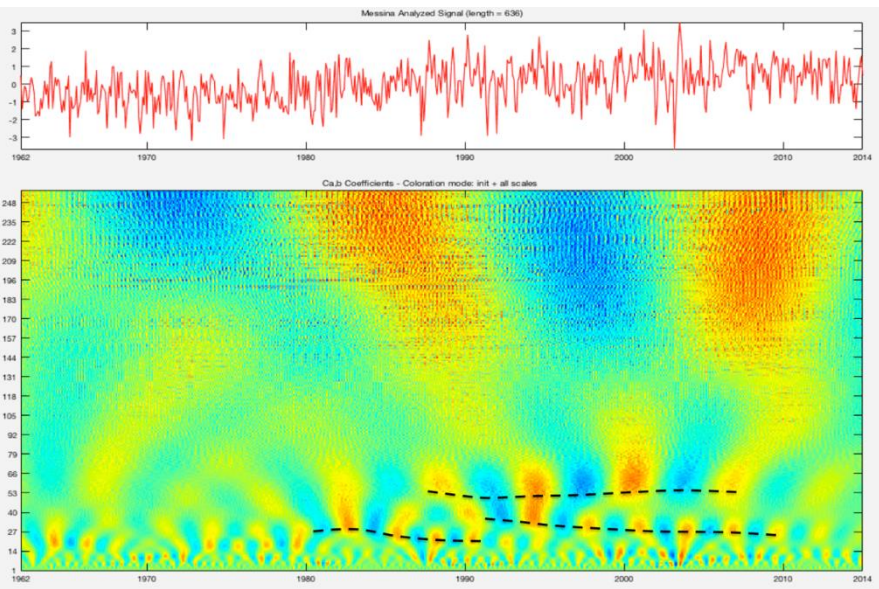

Figure 8. CWT of Messina 1962-2014 mean monthly temperature anomaly.

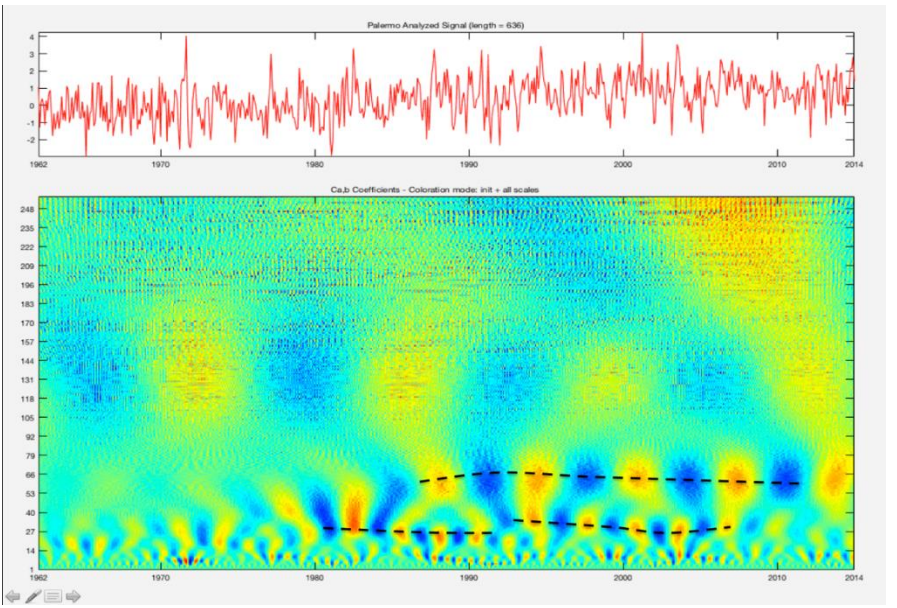

Figure 9. CWT of Palermo 1962-2014 mean monthly temperature anomaly.

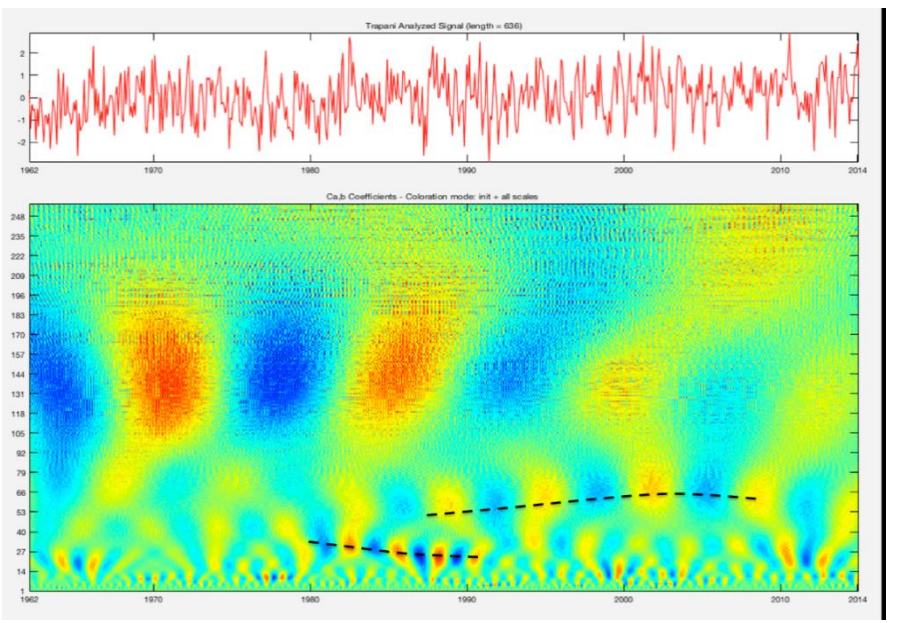

Figure 10. CWT of Trapani 1962-2014 mean monthly temperature anomaly.

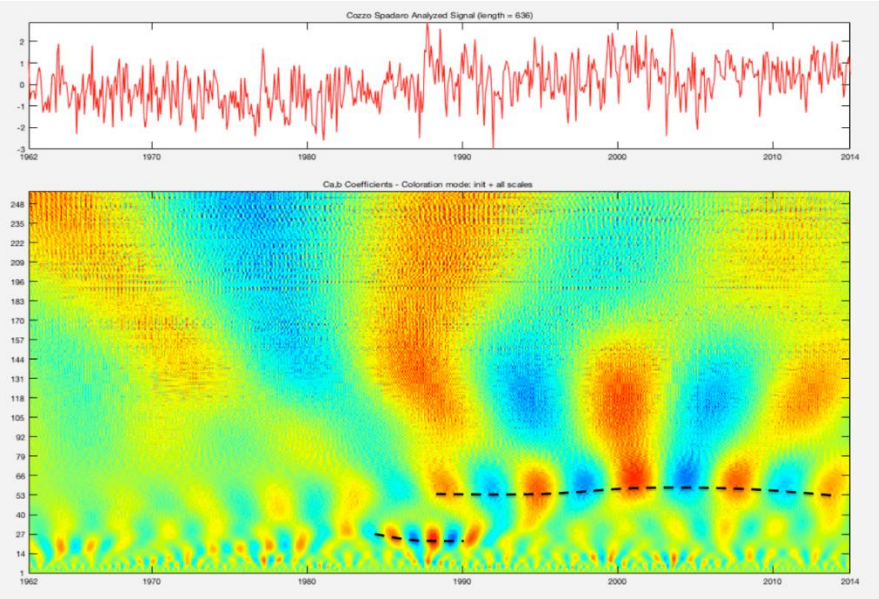

Figure 11. CWT of Cozzo Spadaro 1962-2014 mean monthly temperature anomaly.

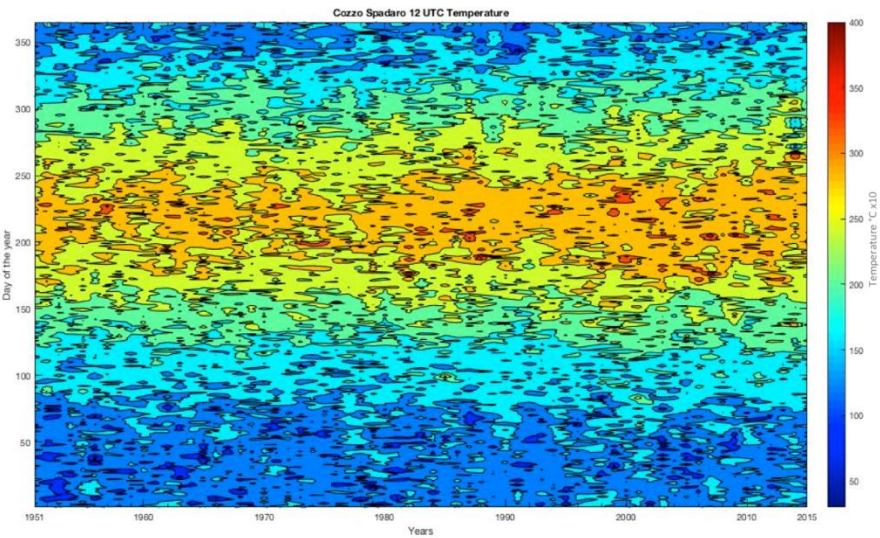

Figure 12. Cozzo Spadaro daily 12 UTC temperature surface plot.

Finally, concerning the Cozzo Spadaro CWT, the graph shows the absence of periodicities until 1985. A periodicity of about 30 months appears and continues till 1990. The singular episode of 1987 is here well marked as the beginning of the 60 months periodicity that continues till the end (Figure 11). The availability of Cozzo Spadaro daily 12 UTC temperatures from 1951 to 2015, let us allow to further explore it in order to understand how the temperature is changing. For this reason, the data have been arranged in a matrix of 365 rows per 65 columns, where the rows represent the days of each year from January 1st (on the bottom) to December 31st (on the top) and the columns (from left to right) the years from 1951 to 2015. To better visualize the temperature changes, a colour scale has been used to represent the temperature. The obtained plot is showed in Figure 12.

Conclusion

The aim of this chapter was to use the Wavelet analysis on a 53 years long temperature time series of four localities of Sicily, in order to detect the temperature trends and to identify the climate dynamics that drives the process of global warming in Sicily and in general in the Mediterranean area. The first step of this work was to compare the annual mean temperatures of Palermo (the longest available time series), with the big world volcanic eruption calendar. It soon appears a strong correlation between the occurrences of an eruption, which is immediately followed by decreasing temperature. As second step, we performed a Discrete Wavelet Transform on the temperature signal, in order to identify the trends present in the signal. For Palermo, the DWT performed on the 150 years temperature time series, identifies a total positive trend of 1,55°C, with two periods of more intense warming during 1880-1910 and 1960-2000, together with a range in which the temperature values have been stationary or decreased. This is about the same trend recorded for the global temperature trend of the Northern Hemisphere. In order to make comparable the four data series, only the common years 1962-2014 have been analysed during the next step. The DWT of the four time series, show that during these years, all the four weather stations have registered a temperature increase. The amplitude of this warming, oscillates from less than 1°C to about 1,4°C, depending on the position and on the characteristics of each weather stations. Both the weather stations positioned inside the town of Palermo and Messina, showed for example, the major increasing of temperature, respectively of 1,37°C and 1,27°C. This is due to the major

anthropogenic impact occurred in the two cities and to the urban heat island effect. The places where the anthropogenic impact was negligible registered a temperature increase of about 1°C during last 53 years.

The next step was to analyse the four time series using the CWT. The obtained results show some common features:

- Two strong singularities that appear in the signal in correspondence of the year 1987 and 2003;
- A 60 months periodicity starting in 1987 and continuing at least until 2010.
- A 128 months periodicity starting in 1962 and continuing to about middle 1980s.

This means that in 1987 something occurred in the climate dynamics of Sicily and requires further analysis. An interesting and intriguing hypothesis is described in different literature papers and regards the sea-atmosphere interaction. Conversi et al. 2010 [38] states "1987 appears to be a year of change for the entire Mediterranean basin surface circulation." Furthermore Demirov and Pinardi's [39] simulations of the interannual surface Mediterranean circulation from 1979 to 1993 identify two periods, 1981–87 and 1988–93, which differ in precipitation and winter wind regimes. Pinardi et al. [40] and Korres et al. [41], using data-validated simulations describe the dramatic reversal of the Ionian gyre in the summer of 1987 from its "usual" cyclonic state to an anticyclonic pattern. In particular, they show a reversal in the surface current directions in the Ionian sea, with the Atlantic/Ionian stream (and associated nutrients and hydrographical properties), branching further northward, at 35.5°N, and linked it to the surface circulation changes to the previous winter anomalies in the winds and heat fluxes. The alteration lasted approximately 10 years, until 1997, when the gyre re-reversed.

The presence of the 128 months periodicity in the CWT, let us to make the hypothesis that before 1985 was the Sun to mainly drive the temperature trends, while starting from the middle 1980s, other cyclic oscillations like ENSO or NAO or others unknown, become most significant in the determination of the increasing temperature.

Finally, the Cozzo Spadaro 12 UTC daily temperature analysis allows to understand the way in which the temperature is changing. Starting from the beginning of the '1980s, a long sequence of red spot is visible in Figure 12. Each red spot could be assimilated to a heat wave with temperature higher of

35°C. This means than the temperature pattern is changing, showing an increasing number of summer hot days and heat waves. Another distinguishing feature is expressed by the colours in the plot where the expansion of the orange area corresponding to an increasing length of the summer season is registered. Counting the number of the days comprised from the first and the last day of the year in which temperature reached 30°C (summer days), the average length passed from about 58 days in 1950s to about 74 days in 2010s, with an average increase of 16 summer days (Figure 13).

Moreover the graph shows that in 1987, 1999 and 2003, the number of summer days exceeded 100 days. This result is coherent with the presence of the singularities we have found in the CWT of the four Sicilian weather stations. These new evidences let us to state that the year 1987 is confirmed to represent an important year for climate change in Sicily because for the first time the number of summer days reached the record value of 100 days. This so high number, was reached again only 12 years later in 1999 and then again in 2003; both years were characterized by a sequence of very long heat wave, one of which is still remembered as "killer heat wave" because during the summer 2003 caused a record high temperature across the whole Europe with at least 30.000 deaths (more than 14.000 in France alone).

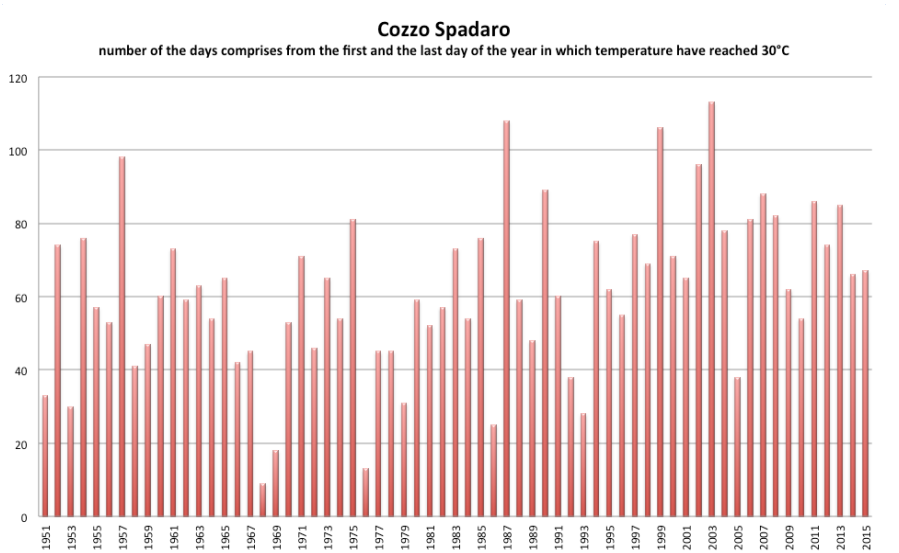

Figure 13. Cozzo Spadaro number of days comprised from the first and the last day of the year in which temperature have reached 30°C (Summer days).

In conclusion, the use of discrete and continuous wavelet analysis coupled with other graphics tools such as the matrix temperature arrangement and the surface graph visualization, reveals to be very powerful tools capable to extract additional and very useful information on the climate dynamics contained in a simple data set of temperature.

References

[1] Caccamo M. T., Castorina G., Colombo F., Insinga V., Maiorana E. and Magazù S. (2017). Weather forecast performances for complex orographic areas: Impact of different grid resolutions and of geographic data on heavy rainfall event simulations in Sicily, *Atmos. Res.* (198): 22-33.

[2] DRPC Sicily – Stato dei rischi del territorio Siciliano – Rischio idrogeologico: raccolta dati storici – Sicilian Territory State of Risk – Hydrogeological Risk: *Historical data Record*.

[3] Future climate in Italy – *An analysis of regional climate models projections.* 2015 National Climate Services Network of Italy – ISPRA - ISBN: 978-88-448-0723-8.

[4] Birsan, M. V., Molnar, P., Burlando, P., Pfaundler, M., 2005. Streamflow trends in Switzerland. *J. Hydrol.* 314 (1–4), 312–329.

[5] Caccamo M. T., Magazù S., Variable mass pendulum behaviour processed by wavelet analysis. *Eur. J. Phys.* 2017; 38(1): article number 15804.

[6] Nalley, D., Adamowski, J., Khalil, B., 2012. Using discrete wavelet transforms to analyze trends in streamflow and precipitation in Quebec and Ontario (1954–2008). *Journal of Hydrology* 475 (2012) 204–228.

[7] Santos, C. A. G., Galvão, C. D. O., Suzuki, K., Trigo, R. M., 2001. Matsuyama city rainfall data analysis using wavelet transform. *Annu. J. Hydraul. Eng.*, JSCE 45, 6.

[8] Migliardo F., Caccamo M. T., Magazù S. Thermal Analysis on Bioprotectant Disaccharides by Elastic Incoherent Neutron Scattering. *Food Biophys.* 2014, 9, 99-104.

[9] Magazù S., Migliardo F., Vertessy B. G., Caccamo M. T. Investigations of homologous disaccharides by elastic incoherent

neutron scattering and wavelet multiresolution analysis. *Chem. Phys*. 2013, 424, 56-61.

[10] Migliardo F., Caccamo M. T., Magazù S. Elastic incoherent neutron scatterings wavevector and thermal analysis on glass-forming homologous disaccharides. *J. Non Cryst. Solids.* 2013;378, 144-151.

[11] Adamowski, K., Prokoph, A., Adamowski, J., 2009. Development of a new method of wavelet aided trend detection and estimation. *Hydrol. Process.* 23 (18), 2686–2696.

[12] Quiroz, R., Yarlequé, C., Posadas, A., Mares, V., Immerzeel, W. W., 2011. Improving daily rainfall estimation from NDVI using a wavelet transform. *Environ. Modell. Softw.* 26 (2), 201–209.

[13] Magazù, S., Migliardo F., Caccamo M. T., Innovative Wavelet Protocols in Analyzing Elastic Incoherent Neutron Scattering. *J. Phys. Chem. B*, 116, 2012, 9417-9423.

[14] Caccamo M. T., Magazù S. Tagging the oligomer-to-polymer crossover on EG and PEGs by infrared and Raman spectroscopies and by wavelet cross-correlation spectral analysis. *Vib Spectrosc.* 2016, 85, 222-227.

[15] Caccamo M. T., Magazù S. Ethylene Glycol - Polyethylene Glycol (EG-PEG) Mixtures: Infrared Spectra Wavelet Cross-Correlation *Analysis. Appl Spectrosc.* 2017, 71, 401-409.

[16] Nolin, A. W., Hall-McKim, E. A., 2006. Frequency modes of monsoon precipitation in Arizona and New Mexico. *Mon. Weather Rev.* 134 (12), 3774–3781.

[17] Caccamo M. T., Magazù S. Multiscaling Wavelet Analysis of Infrared and Raman Data on Polyethylene Glycol 1000 Aqueous Solutions. *Spectrosc Lett.* 2017, 50, 130-136.

[18] Caccamo M. T., Magazù S. Thermal restraint on PEG-EG mixtures by FTIR investigations and wavelet cross-correlation analysis. *Polym Testing* 2017, 62, 311-318.

[19] Goodwin, D. A., 2008. *"Wavelet Analysis of Temporal Data"*. Dissertation, Department of Statistics, The University of Leeds, Leeds, UK.

[20] Kim, S., 2004. Wavelet analysis of precipitation variability in northern California, USA. *KSCE J. Civ. Eng.* 8 (4), 471–477.

[21] Labat, D., 2005. Recent advances in wavelet analyses: Part 1. A review of concepts. *J. Hydrol.* 314 (1–4), 275–288.

[22] Wang, W., Hu, S., Li, Y., 2011. Wavelet transform method for synthetic generation of daily streamflow. *Water Resour. Manage*. 25 (1), 41–57.

[23] Lau M., Weng H., Climate Signal Detection Using Wavelet Transform: How to Make a Time Series *Sing Bulletin of the American Meteorological Society*, 76, 1995, p. 2391–2401.

[24] N. Marchese, A. Cannuli, M. T. Caccamo, C. Pace 2016 New generation non-stationary portable neutron generators for biophysical applications of neutron activation analysis. *Biochimica et Biophysica Acta (BBA)* 1861, Part B, 3661-3670.

[25] Caccamo, E. Calabrò, A. Cannuli and S. Magazù 2016 Wavelet Study of Meteorological Data Collected by Arduino-Weather Station: Impact on Solar Energy Collection Technology, *MATEC Web of Conference 55*, 02004.

[26] Daniel T. L., Yamamoto A., 1994. Wavelet analysis: theory and application. *Hewlett-Packard Journal December* 1994, 44-52.

[27] Drago, A. F., Boxall, S. R., 2002. Use of the wavelet transform on hydro-meteorological data. *Phys. Chem. Earth* 27 (32–34), 1387–1399.

[28] Burn, D. H., Hag Elnur, M. A., 2002. Detection of hydrologic trends and variability. *J. Hydrol.* 255 (1–4), 107–122.

[29] Partal, T., 2010. Wavelet transform-based analysis of periodicities and trends of Sakarya basin (Turkey) streamflow data. *River Res. Appl.* 26 (6), 695–711.

[30] Mishra, A. K., Singh, V. P., 2010. Changes in extreme precipitation in Texas. *J. Geophys. Res*. 115 (D14), D14106.

[31] Adamowski, K., Prokoph, A., Adamowski, J., 2009. Development of a new method of wavelet aided trend detection and estimation. *Hydrol. Process.* 23 (18), 2686–2696.

[32] Chou, C. M., 2007. Applying multi-resolution analysis to differential hydrological grey models with dual series. *J. Hydrol.* 332 (1–2), 174–186.

[33] Migliardo F., Magazù S., Caccamo M. T. Infrared, Raman and INS studies of poly-ethylene oxide oligomers. *J. Mol. Struct.* 2013, 1048, 261-266.

[34] Bruce, L. M., Koger, C. H., Jiang, L., 2002. Dimensionality reduction of hyperspectral data using discrete wavelet transform feature extraction. *IEEE Trans. Geosci. Remote Sens*. 40 (10), 2331–2338.

[35] Magazù S., Migliardo F., Caccamo M. T. Upgrading of resolution elastic neutron scattering (RENS), *Advances in Materials Science and Engineering*, Volume 2013, 2013, Article number 695405.

[36] Lau, K. M., Weng, H., 1995. Climate signal detection using wavelet transform: How make a time series sing. *Bulletin of American Meteorological Society* Vol. 76, No 12, December 1995.

[37] 3Farge, M., 1992: Wavelet transforms and their applications to turbulence. *Annu. Rev. Fluid Mech*., 24, 395–457.

[38] Conversi A., Fonda Umani S., Peluso T., Molinero J. C., Santojanni A, et al. (2010) The Mediterranean Sea Regime Shift at the End of the 1980s, and Intriguing Parallelisms with Other European Basins. *PLoS ONE* 5.

[39] Demirov E., Pinardi N. (2002) Simulation of the Mediterranean Sea circulation form 1979 to 1993. Part I: the interannual variability. *J Mar Syst* 33: 23–50.

[40] Pinardi N., Korres G., Lascaratos A., Roussenov V., Stanev E. (1997) Numerical simulation of the interannual variability of the Mediterranean Sea upper ocean circulation. *Geophys Res Lett* 244: 425–428.

[41] Korres G., Pinardi N., Lascaratos A. (2000) The ocean response to low-frequency interannual atmospheric variability in the Mediterranean Sea. Part II: Empirical Orthogonal Function Analysis. *J Clim* 13: 732–745.

In: Wavelets: Principles, Analysis and Applications ISBN: 978-1-53613-374-5
Editor: Joseph Burgess

Chapter 4

APPLICATIONS OF WAVELET ANALYSES ON SPECTROSCOPIC EXPERIMENTS

M. T. Caccamo and S. Magazù
Dipartimento di Scienze Matematiche e Informatiche,
Scienze Fisiche e Scienze della Terra,
Università di Messina, Messina, Italy
Istituto Nazionale di Alta Matematica "F. Severi" – INDAM -
Gruppo Nazionale per la Fisica Matematica – GNFM, Rome, Italy

Abstract

Wavelet transform is an innovative and powerful tool for analyzing complex data such as those obtained by spectroscopic techniques. In particular, it allows to locally resolve a non-stationary signal by means of functions called mother wavelets so producing a time-scale view of the signal. In addition, thanks to the wavelet multiscaling properties it is possible to get information both on a global and on a local view, to characterize transitory signal characteristics, trends, drifts, spectra abrupt changes and to perform signal denoising.

The aim of this chapter is to highlight how wavelet transform can be effectively employed to extract precious information from experimental results obtained by spectroscopic techniques, such as Infrared, light and neutron scattering spectroscopies.

In particular, it will be shown how it is possible to characterize, following different approaches, the registered spectral profiles as well as, by means of Wavelet Cross Correlation, to evaluate spectra and images similarity degree.

Keywords: wavelet transform, Fourier transform, spectroscopy, applications

Introduction

Wavelet analysis (WT) has revealed to be a new, effective and powerful tool in signal treatment, especially when these contain non-stationary or transitory features such as rapid changes, discontinuities, self-similarity features, noise, etc. WT analysis is capable of extracting data features that other signal analysis techniques miss. This is possible using long time windows for extracting low-frequency information, and short time windows for extracting high-frequency information and, in doing so it does not work on a time frequency space, but on a time-scale space [1-5].

Let $L^2(\mathbb{R})$ be the space of Lebesgue measurable functions and $\psi(t) \in L^2(\mathbb{R})$ a fixed function;

$\psi(t)$ is said to be a wavelet if it satisfies the following three conditions:

1) admissibility condition:

$$C_\psi = \int_0^\infty \frac{|\hat{\psi}(\omega)|^2}{|\omega|} d\omega < \infty \quad (1)$$

where $\hat{\psi}$ denotes the Fourier Transform of $\psi(t)$;

2) zero average:

$$\int_{-\infty}^{\infty} \psi(t) dt = \hat{\psi}(0) = 0; \quad (2)$$

3) finite energy:

$$E = \int_{-\infty}^{\infty} |\psi(t)|^2 dt < \infty. \quad (3)$$

Continuous WT (CWT) provides the wavelet coefficients and defines a scalogram, i.e., a local time–frequency energy density:

$$P_W(s,\tau) = |W(s,\tau)|^2 \quad (4)$$

where s is the scale parameter, τ the shift parameter and $W(s,\tau)$ is the wavelet coefficient matrix. In other words, $P_W(s,\tau)$ provides the time evolution of energy by viewing a map of the square of the wavelet coefficients; in different words, it reveals pockets of high and low energy in different frequency basis [6-10].

Since many data are constituted by a finite number of values, it is important to consider also a discrete version of the CWT. Generally, the orthogonal (discrete) WT are employed because this method associates the wavelets to orthonormal bases of $L^2(\mathbb{R})$. In this case, the WT is performed on only a discrete grid of parameters of dilation and translation. Within this framework, an arbitrary signal $h(t)$ of finite energy can be written using an orthonormal wavelet basis:

$$h(t) = \sum_i \sum_j d_j^i \psi_j^i(t)\,, \tag{5}$$

where the coefficients of the expansion are given by

$$d_j^i = \int_{-\infty}^{\infty} y(t)\,\psi_j^i(t)dt. \tag{6}$$

Another quantity associated to WT is the WT cross correlation that furnishes a measure of the correlation degree between two spectra: WT cross correlation is defined as:

$$XWT = W_{1,2}(s,\tau) = W_1(s,\tau)W_2^*(s,\tau) \tag{7}$$

where $W_1(s,\tau)$ represents the WT of the first signal, $W_2(s,\tau)$ is the WT of the second signal, and * denotes the complex conjugation. More precisely, XWT provides the WT cross-spectrum$\left|W_{1,2}(s,\tau)\right|$, that allows to quantify the power correlation and the relative phase between two signals [48–50]. The cross-correlation coefficients are complex numbers and can be represented as $W_1(s,\tau) = |W_1(s,\tau)\exp\phi_1(s,\tau)|$. $|W_1(s,\tau)|$ is the wavelet amplitude while $\phi_1(s,\tau)$ is the absolute phase defined in the scale–time plane. $\left|W_{1,2}(s,\tau)\right|$ shows the regions where $W_1(s,\tau)$ and $W_2(s,\tau)$ have a high common power.

The phase difference between the two time signals is:

$$\phi_{1,2}(s,\tau) = \phi_1(s,\tau) - \phi_2(s,\tau) \tag{8}$$

where $\phi_1(s,\tau)$ = phase of e and $\phi_1(s,\tau)$ is the phase of I can be evaluated as it follows:

$$\phi_{1,2}(a,\tau) = \tan^{-1}\left(\frac{\mathrm{Im}(\langle s^{-1}W_{1,2}(s,\tau)\rangle)}{\mathrm{Re}(\langle s^{-1}W_{1,2}(s,\tau)\rangle)}\right) \quad (9)$$

where <> represents the average operator. It should be stressed that a high correlation between two time signals is connected both with a high common power at a given time and scale (frequency) and an in-phase behaviour [11-14].

In this chapter it will be shown how WT makes possible to characterize the registered spectral profiles performing an analysis at different space scales, to perform a spectra analysis at different frequency scale and to evaluate, by means of the Wavelet Cross Correlation operator, the similarity degree of spectra and images.

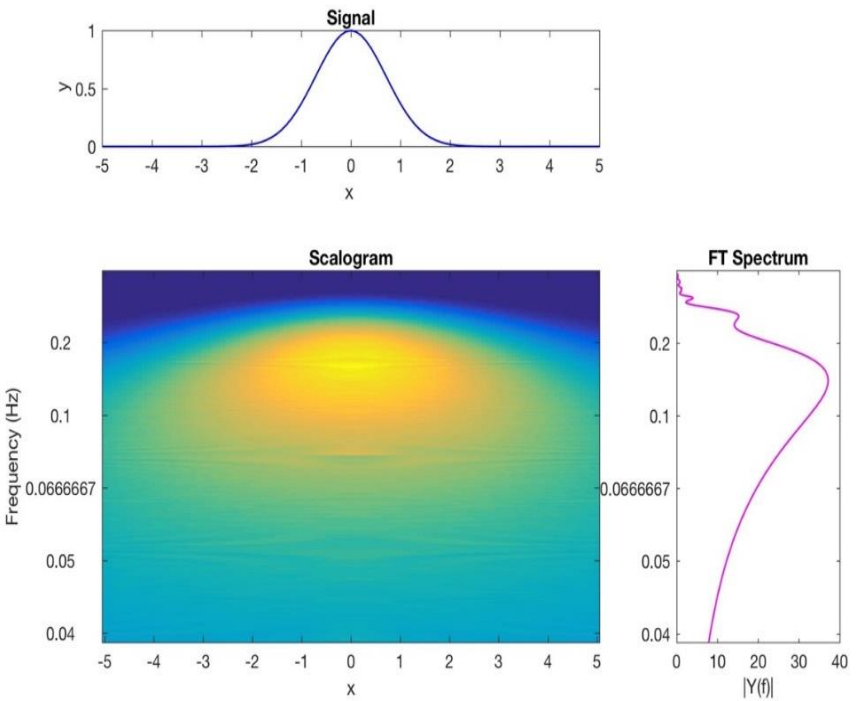

Figure 1. Comparison between the results of an FT and the WT spectral analysis obtained for a damped time oscillation.

In order to perform a comparison between the Fourier Trasform (FT) and WT, Figure 1 shows a comparison between the results of the FT and the WT spectral analysis for a damped time oscillation while Figure 2 shows the same comparison for a chopped chipir function. It is evident that, in this latter case, FT furnishes only an average frequency value while WT furnishes information on the time evolution of the frequencies content.

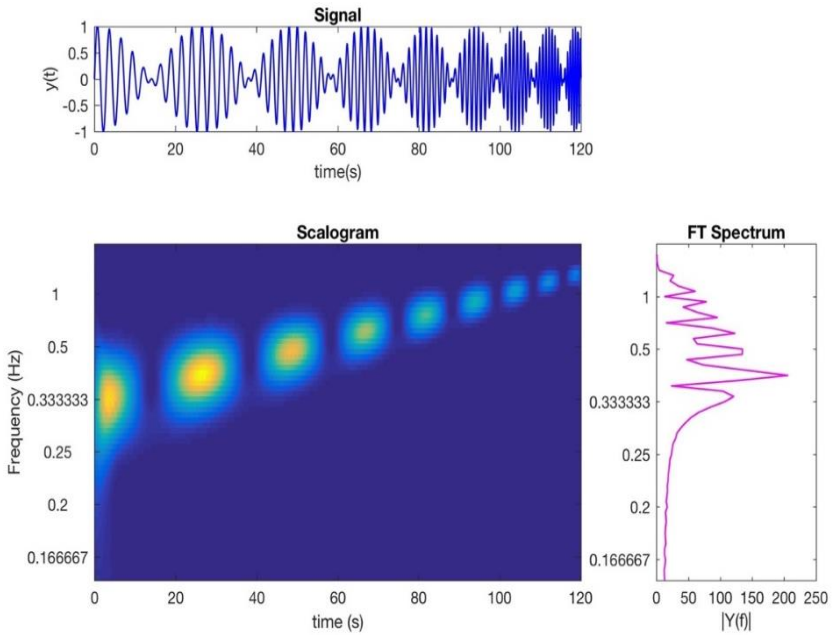

Figure 2. Comparison between the results of an FT and the WT spectral analysis obtained for a chopped chipir function. It is evident that FT furnishes only an average frequency value while WT furnishes information on the time evolution of the frequencies content.

Detection of Anomalies and Discontinuities in Data Trend

WT analysis is capable to detect aspects of data such as anomalies and discontinuities in the data trend that other signal analysis techniques miss. On that score, in Figure 3, a signal with a sudden spike is shown; the wavelet analysis, which defines a local time−frequency energy density, clearly reveals the spike of the signal [15-16].

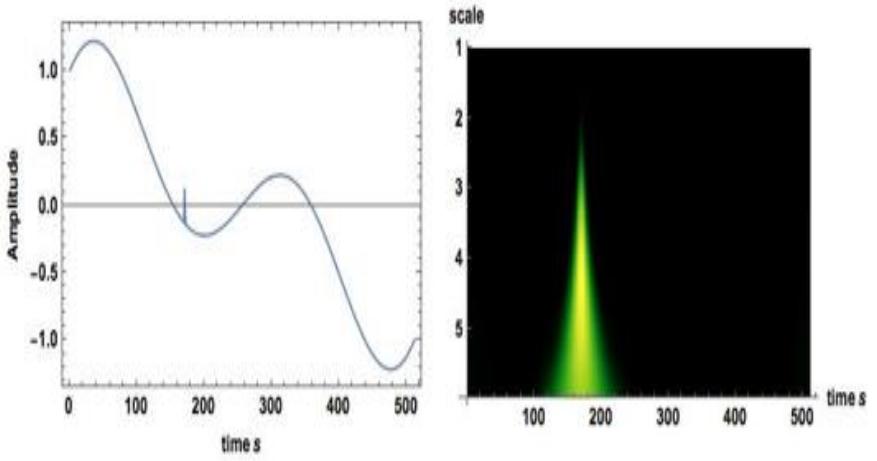

Figure 3. On the left a signal with a spike and on the right the relatively 2D scalogram plot. As it can be seen the wavelet transform clearly reveals the spike of the signal.

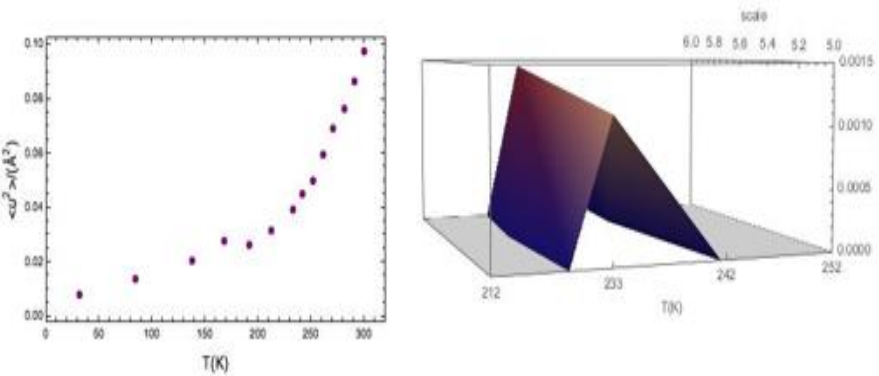

Figure 4. MSD as a function oftemperature for D2O hydrated lysozyme/glycerol (50:50) for h=0.1 on the top and its relative 3D scalogram which shows a kink at T∼233 K.

A further example of application of WT analysis which show how WT is capable to detect discontinuities in the data trend is reported in Figure 4 where the so called Mean Square Displacement $\mathrm{MSD} = \langle u^2(T) \rangle_{tot}$ versus temperature, evaluated by means of Elastic Incoherent Neutron Scattering (EINS), for D2O hydrated lysozyme/glycerol (50:50) is reported [17]; in such a case the 3D scalogram obtained by WT analysis allows to localize the kink in the MSD vs T trend at T ∼ 234 K.

Spectra Denoising

It is well known that in many cases the noise can corrupt a signal (e.g., spectrum) in a significant way. The procedure of noise removal is generally referred to as denoising. There is a wide range of applications in which denoising is important including, for instance, medical image/signal analysis, data mining, radio astronomy, spectral analysis and so on. There are many approaches in the literature for denoising. They can be roughly divided into two classes: i) denoising in the original signal domain (e.g., time or space) and denoising in the transform domain (e.g., Fourier or Wavelet Transform). WT is a powerful tool for removing noise from a variety of signals due to its ability to decompose a signal into different scales. Such a property is very important for denoising and it improves the analysis of the signal significantly. In particular, it allows to analyse the noise level at different scales and to adapt a denoising algorithm accordingly. Furthermore, WT does not require particular assumptions about the signal nature, also in the presence of discontinuities. Whereas classical denoising methods of a signal remove the high frequency components which are usually associated with the noise, i.e., provide a signal smoothing, WT attempts to remove whatever noise is present and retain whatever signal is present regardless of the signal frequency content. This approach has been proven to be optimal when the smoothness of the signal is unknown. The general wavelet–based method for denoising is to transform the data into the wavelet domain, threshold the wavelet coefficients, and invert the transform; inparticular WT allows to: i) decompose the signal by choosing a wavelet and a level nand then to compute the wavelet decomposition of the signal S down to level N; ii) to threshold detail coefficients for each level from 1 to N and iii) to reconstruct the signal. In Figure X is reported, as an example, a Noised Signal (NS) decomposed by means of Discrete WT into a Signal (S) and Noise (N) contribution; furthermore a decomposition of the signal into approximate and detail coefficients [18, 19].

Spectral Analysis of Spatial Data

WT allows to perform a spatial analysis of spectroscopic data simultaneously on different space scales. A remarkable example of such a WT analysis is obtained by taking into account neutron elastic intensity data collected as a function of exchanged wavevector [20-28].

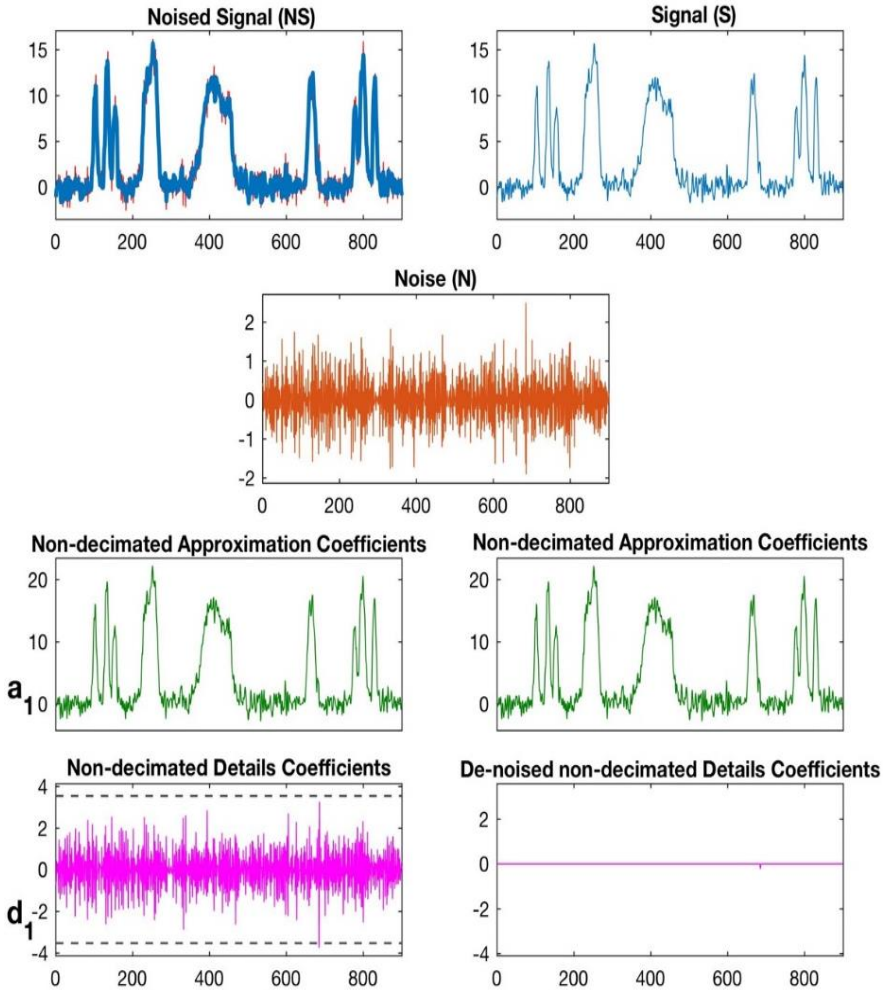

Figure 5. A Noised Signal (NS) decomposed by means of Discrete WT into a Signal (S) and Noise (N) contribution; furthermore a decomposition of the signal into approximate and detail coefficients.

In such a case WT allows to characterize the protons dynamics in different wave-vector ranges. As it can be seen in Figure 6, which report the 3D scalogram of EINS data at the temperature value of T = 264 K, two different contributions at low and high wavevector values, i.e., Q<0.25Å-1andQ > 0.25Å-1 clearly emerge. WT allows to evaluate the correlation degree at

different scales between collected spectra. Figure 7 shows, as an example, the results of a wavelet cross-correlation analysis between different couples of Infrared spectroscopy spectra of pure polyethylene oxide with molecular weight 600 Dalton (PEG600) and a mixture of PEG600 with Ethylene Glycole (EG), in the proportion [(75% PEG600):(25% EG)], i.e., [PEG600]–[(75% PEG600):(25% EG)]. XWT analysis for the pairs of spectra [PEG600]–[(75% PEG600):(25% EG)] was performed at T=43°C [29-31].

The color scale is proportional to the WT cross-correlation power, represented in octaves. The arrows superimposed on the color representation show the local "phase" difference between the two spectra. More precisely, the phase arrows show the relative phasing of each pair of spectra.

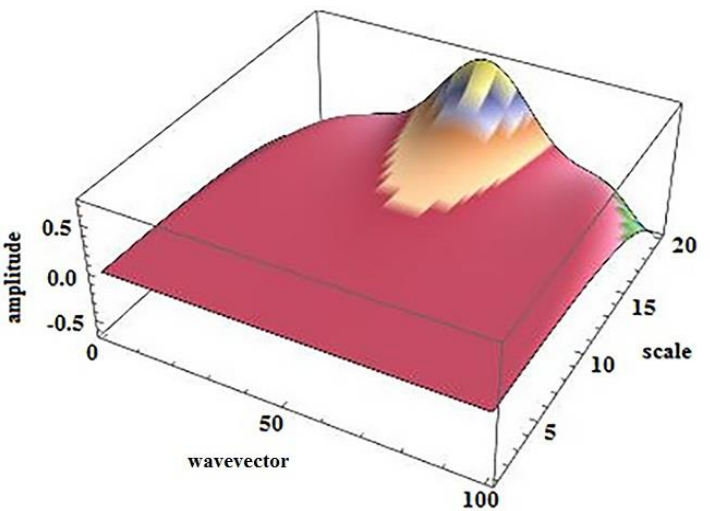

Figure 6. 3D scalogram for trehalose/19 H2O mixtures at three different temperatures, 264K Spectral correlation.

The arrows superimposed on the color representation show the local "phase" difference between the two spectra. More precisely, the phase arrows show the relative phasing of each pair of spectra: arrows pointing right denote in-phase spectra while arrows pointing left denote anti-phase spectra. Arrows pointing up denote that the second spectrum leads the first spectrum by 90° while arrows pointing down denote that the first spectrum leads the second spectrum by 90°. The shaded regions indicate the cone of influence.

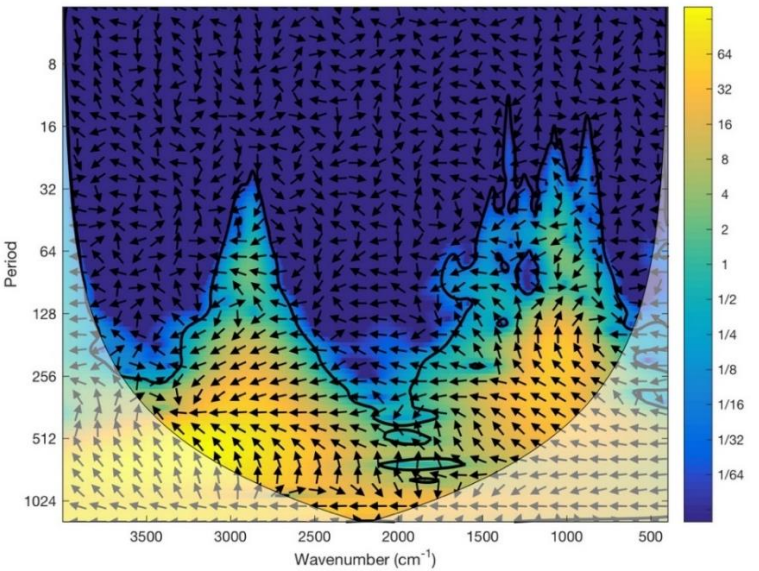

Figure 7. Wavelet cross-correlation (XWT) analysis for the pairs of spectra [PEG600]–[(75% PEG600):(25% EG)] at T=43°C; the color scale is proportional to the WT cross-correlation power, represented in octaves.

The arrows which point towards right denote in-phase spectra while arrows which point towards left denote anti-phase spectra [32-39]. Arrows pointing up denote that the second spectrum leads the first spectrum by 90° while arrows pointing down denote that the first spectrum leads the second spectrum by 90°. The shaded regions indicate the cone of influence.

Conclusion

The goal of this chapter is to highlight how WT can be effectively employed to extract precious information from experimental results obtained by means of different spectroscopic techniques. Specific reference is made to Infrared spectroscopy, light and neutron scattering. In particular, it will be shown how it is possible to characterize the registered spectral profiles performing an analysis at different space scales, to perform a spectra analysis at a different frequency scale and to evaluate, by means of the Wavelet Cross Correlation operator, the similarity degree of spectra and images. Finally it is shown how, thanks to the wavelet multiscaling properties, it is possible to get information both on a global and on a local view.

References

[1] Nalley, D., Adamowski, J., Khalil, B (2012). Using discrete wavelet transforms to analyze trends in streamflow and precipitation in Quebec and Ontario (1954–2008). *Journal of Hydrology*, 475 (2012) 204–228.

[2] Santos, C. A. G., Galvão, C. D. O., Suzuki, K., Trigo, R. M. (2001). Matsuyama city rainfall data analysis using wavelet transform. *Annu. J. Hydraul. Eng., JSCE,* 45, 6.

[3] Adamowski, K., Prokoph, A., Adamowski, J. (2009). Development of a new method of wavelet aided trend detection and estimation. *Hydrol. Process*, 23 (18), 2686–2696.

[4] Quiroz, R., Yarlequé, C., Posadas, A., Mares, V., Immerzeel, W. W. (2011). Improving daily rainfall estimation from NDVI using a wavelet transform. *Environ. Modell. Softw*., 26 (2), 201–209.

[5] Nolin, A. W., Hall-McKim, E. A. (2006). Frequency modes of monsoon precipitation in Arizona and New Mexico. *Mon. Weather Rev.*, 134 (12), 3774–3781.

[6] Goodwin, D. A. (2008). *Wavelet Analysis of Temporal Data. Dissertation*, Department of Statistics, The University of Leeds, Leeds, UK.

[7] Kim, S. (2004). Wavelet analysis of precipitation variability in northern California, USA. *KSCE J. Civ. Eng*., 8 (4), 471–477.

[8] Labat, D. (2005). Recent advances in wavelet analyses: Part 1. A review of concepts. *J. Hydrol*., 314 (1–4), 275–288.

[9] Wang, W., Hu, S., Li, Y. (2011). Wavelet transform method for synthetic generation of daily streamflow. *Water Resour. Manage*, 25 (1), 41–57.

[10] Lau, M., Weng, H. (1995). Climate Signal Detection Using Wavelet Transform: How to Make a Time Series SingBulletin of the *American Meteorological Society*, 76, p. 2391–2401.

[11] Caccamo, M. T., Magazù, S. (2017). Thermal restraint on PEG-EG mixtures by FTIR investigations and wavelet cross-correlation analysis. *Polym. Testing*, 62, 311-318.

[12] Caccamo, M. T., Magazù, S. (2017). Variable mass pendulum behaviour processed by wavelet analysis. *Eur. J. Phys.*, 38(1): article number 15804.

[13] Daniel, T. L., Yamamoto, A., (1994). Wavelet analysis: theory and application. *Hewlett-Packard Journal December*, 44-52.

[14] Drago, A. F., Boxall, S. R., 2002. Use of the wavelet transform on hydro-meteorological data. *Phys. Chem. Earth*, 27 (32–34), 1387–1399.

[15] Marchese, N., Cannuli,A., Caccamo, M. T., Pace, C.(2016). New generation non-stationary portable neutron hhhgenerators for biophysical applications of neutron activation analysis *Biochimica et Biophysica Acta (BBA)*,1861, Part B, 3661-3670.

[16] Partal, T. (2010). Wavelet transform-based analysis of periodicities and trends of Sakarya basin (Turkey) streamflow data. *River Res. Appl*., 26 (6), 695–711.

[17] Magazù, S., Migliardo, F., Caccamo, M. T. (2012). Innovative Wavelet Protocols in Analyzing Elastic Incoherent Neutron Scattering *J. Phys. Chem. B*, 116, 9417-9423.

[18] Adamowski, K., Prokoph, A., Adamowski, J. (2009). Development of a new method of wavelet aided trend detection and estimation. *Hydrol. Process*, 23 (18), 2686–2696.

[19] Bruce, L. M., Koger, C. H., Jiang, L. (2002). Dimensionality reduction of hyperspectral data using discrete wavelet transform feature extraction. *IEEE Trans. Geosci. Remote Sens*., 40 (10), 2331–2338.

[20] Barreca, D., Laganà, G., Ficarra, S., Tellone, E., Leuzzi, U., Magazù, S., Galtieri, A., Bellocco, E. (2010). Anti-aggregation properties of trehalose on heat-induced secondary structure and conformation changes of bovine serum albumin. *Biophys. Chem*., 147, 146-152.

[21] Pagnotta, S. E., Ricci, M. A., Bruni, F., McLain, S., Magazù, S. (2008) Water structure around trehalose. *Chem. Phys.*, 2008, 345, 159-163.

[22] Faraone, A., Magazù, S., Maisano, G., Ponterio, R., Villari, V. (1999). Experimental Evidence of Slow Dynamics in Semidilute Polymer Solutions. *Macromolecules*, 32, 1128-1133.

[23] Magazù, S.; Maisano, G.; Mallamace, F.; Micali N. (1989). Growth of Fractal Aggregates in Water Solutions of Macromolecules by Light-Scattering. *Phys. Rev. A.*,39, 4195-4200.

[24] Jannelli, M. P., Magazù, S., Migliardo, P., Aliotta, F., Tettamanti, E. (1996). Transport properties of liquid alcohols investigated by

IQENS, NMR and DLS studies. *J. Phys. Condens. Matter*., 8, 8157-8171.

[25] Ballone, P., Marchi, M., C. Branca, A., Magazú, S. (2000). Structural and Vibrational Properties of Trehalose: A Density Functional Study, *J. Phys. Chem. B.*, 104, 6313–6317.

[26] Lokotosh, T. V., Magazù, S., Maisano, G., Malomuzh, N. P. (2000). Nature of self-diffusion and viscosity in supercooled liquid water. *Phys Rev E - Stat Physics, Plasmas, Fluids, Relat. Interdiscip. Top.*, 62, 3572-3580.

[27] Branca, C., Magazù, S., Maisano, G., Migliardo, P., Villari, V. (1998). Conformational distribution of poly(ethylene oxide) in molten phase and in aqueous solution by quasi-elastic and inelastic light scattering. *J. Phys. Condens. Matter*., 10, 10141-10157.

[28] Magazù, S. (1996). IQENS - Dynamic Light Scattering Complementarity on Hydrogenous Systems. *Phys. B.*, 226, 92-106.

[29] Caccamo, M. T., Magazù, S. (2016). Tagging the oligomer-to-polymer crossover on EG and PEGs by infrared and Raman spectroscopies and by wavelet cross-correlation spectral analysis. *Vib. Spectrosc.*, 85, 222-227.

[30] Caccamo, M. T., Magazù, S. (2017). Ethylene Glycol - Polyethylene Glycol (EG-PEG) Mixtures: Infrared Spectra Wavelet Cross-Correlation Analysis. *Appl. Spectrosc*., 71, 401-409.

[31] Caccamo, M. T., Cannuli, A., Calabrò, E., Magazù, S. (2017). Acoustic Levitator Power Device: Study of Ethylene-Glycol Water Mixtures. *IOP Conf. Ser. Mater. Sci. Eng.*, 199, 12119.

[32] Magazù, S., Calabrò, E., Caccamo, M. T., Cannuli, A. (2016). The shielding action of disaccharides for typical proteins in aqueous solution against static, 50 Hz and 1800 MHz frequencies electromagnetic fields. *Curr.Chem. Biol.*, 10, 57-64.

[33] Migliardo, F., Caccamo, M. T., Magazù, S. (2014) Thermal Analysis on Bioprotectant Disaccharides by Elastic Incoherent Neutron Scattering. *Food Biophys*., 9, 99-104.

[34] Magazù, S., Migliardo, F., Vertessy, B. G., Caccamo, M. T. (2013). Investigations of homologous disaccharides by elastic incoherent neutron scattering and wavelet multiresolution analysis. *Chem. Phys.*, 424, 56-61.

[35] Migliardo, F., Caccamo, M. T., Magazù, S. (2013). Elastic incoherent neutron scatterings wavevector and thermal analysis on glass-forming homologous disaccharides. *J. Non Cryst. Solids*, 378, 144-151.

[36] Migliardo, F., Magazù, S., Caccamo, M. T. (2013). Infrared, Raman and INS studies of poly-ethylene oxide oligomers. *J. Mol. Struct.*, 1048, 261-266.

[37] Magazù, S., Migliardo, F., Caccamo, M. T. (2013). Upgrading of resolution elastic neutron scattering (RENS), *Advances in Materials Science and Engineering*, Volume 2013, Article number 695405.

[38] Lau, K. M., Weng, H. (1995). Climate signal detectionusing wavelet transform: How make a time series sing. *Bulletin of American Meteorological Society*, Vol. 76, No 12.

[39] Farge, M. (1992). Wavelet transforms and their applications to turbulence. *Annu. Rev. Fluid Mech.*, 24, 395–457.

In: Wavelets: Principles, Analysis and Applications ISBN: 978-1-53613-374-5
Editor: Joseph Burgess

Chapter 5

THE "À TROUS" TRANSFORM WITH WAVELET EXTRAPOLATED BOUNDARY EXTENSIONS FOR DATA ANALYSIS

Alice J. Kozakevicius* *and Alex A. Schmidt*†
Department of Mathematics
Universidade Federal de Santa Maria-UFSM
Santa Maria, RS, Brazil

Abstract

An iterative *à trous* coarsening algorithm combined with a wavelet extrapolation procedure is presented and analyzed to filter and identify the mean trend of simulated 1D data with non trivial boundary conditions. Results show that the wavelet extrapolation based algorithm considered for the data-driven analysis is robust and reliable, enabling the increase of the confidence region of the wavelet transform. Relative errors for the simulations were found to be in the order of 0.2% or less for each simulated 1D data set, independent of noise intensity, decomposition level or coarsest signal shape near data boundaries, confirming the contribution of the wavelet extrapolation to the non-linear analysis scheme. The intrinsic interpolatory property of the wavelet transform, combined with the *à trous* coarsening algorithm, also allowed the proposal of an automatic local curve approximation procedure for regions where strong localized

*Corresponding Author Email: alicek@ufsm.br.
†Corresponding Author Email: aas@ufsm.br.

influences are present and need to be removed in order to diminish distortions in the mean signal pattern. The proposed procedure avoids the necessity of model fitting for the regions to be treated. Numerical simulations for the analysis of noisy data are also presented and discussed, highlighting the potential of the proposed scheme to be considered for a wide range of applications.

PACS: 02.60.Ed, 02.60.Gf

Keywords: *à trous* transform, wavelet extrapolation, data-driven analysis, adaptive filtering process

AMS Subject Classification: 42C40, 60G35, 65T60

1. Introduction

The wavelet boom goes back to the 80's and 90's, when most of the contributions were focused on the theory development [3, 6], creation of different wavelet families [8,25] and design of fast algorithms [17,33]. In fact, this rather new wavelet approach brought to the scientific community, in a wide range of applications, a complementary powerful tool (with respect to Fourier Transform) for analyzing and representing information according to different scales of resolution [6]. In particular, astronomical data – generally having a fractal structure – greatly benefits from the multiscale analysis wavelet transforms can provide [28].

One of the formulations for the fast wavelet transform, and the one considered in this work, is its undecimated version, known as the *à trous* transform, where the number of points in each resolution level is kept equal to the initial amount of points of the input data. The *à trous* algorithm, belonging to the class of stationary wavelet transforms, is known for being ingenious and conveniently easy to implement. It uses scaling functions with compact support, assuming a formulation based on their filters and its reconstruction algorithm is quite simple [30]. The *à trous* algorithm was first developed for music synthesis [13] and has been applied in a variety of signal and image processing studies ever since [7, 22]. Along with other wavelet transforms, it has been widely used in astrophysical data analysis [29] (and references therein) from X-ray imaging of extended sources to studies of spatial distribution of galaxies. In particular, the *à trous* algorithm has proven to be very useful in extracting information from noisy spectra [27, 31].

It is well known that the quality of the results obtained by any transformation at the vicinity of the domain boundaries may lack reliability due to the assumptions considered to produce approximated values outside the domain, which are necessary for computing interior values. These assumptions involve the definition of the basis functions and/or the type of extrapolation computed [11, 32] – the periodic extension been one of the most common used. In many applications the edge effects are rarely mentioned or simply neglected [34]. Of course, in many cases disregarding these effects may cause no significant damage to the analysis, but this can not be considered as an *ad hoc* universal true, specially when treating information through multiresolution approaches and involving non-linear analysis, since the extrapolation procedure requested at any level of the decomposition may cause a significant impact in the final analysis result. This issue motivates the study presented here.

One of the first attempts to circumvent the periodicity assumption for data extension was proposed by Cohen et al. in [5], where a modified family of orthogonal wavelets for a finite closed interval was introduced. Their procedure implied the construction of new filters for the wavelet transform which should be utilized whenever data at the boundaries or beyond the finite domain should be considered for the standard transform. This formulation, presented in 1993, is effective in theory but not entirely satisfactory for practical applications. Since then, alternative constructions for the interval wavelet have been proposed [2, 14, 15] as well as new families of wavelets such as countourlets, ridglets, curvelets, bandlets and other families incorporating geometrical and directional properties in the wavelet design [23, 26, 29].

Attempts involving biorthogonal wavelets on the interval again go back to the 90's, having another seminal work from Cohen et al. in [4] as main reference, in which the starting point is the modification of the scaling, the wavelet and their associated dual functions on the boundaries and their inner vicinity. More recent formulations involving spline-wavelets [19] despite being more stable, still require the reformulation of all four families of functions involved in the transformation on the boundaries. As an alternative, different types of strategies to extrapolate data had also been investigated. In [11], different wavelets families had been considered: Daubechies for the extrapolation and Spline-wavelets for the transformation. In [32], the extrapolation was handled through the Fourier transform, associated to the wavelet analysis. In fact, hybrid formulations for sparse and redundant data representation have been gaining space, specially in the context of methods based on dictionaries [20], in which differ-

ent types of wavelet transforms can be part of the many different steps of the dictionary learning process [18].

The current chapter combines the data extrapolation procedure, presented in work [11], with the undecimated wavelet transform assuming spline-wavelet filters to propose an iterative algorithm for determining the mean trend of simulated data. The Daubechies orthonormal compactly supported wavelets are only deployed throughout the one dimensional extrapolation construction, and for the discrete wavelet transform itself we make use of the *à trous* transform [9,24] with bi-orthogonal spline wavelets filters, providing a simplification in the design of the transformation as well as its inverse. In [11], the algorithm for data extrapolation considered is based on the vanishing moments property of the Daubechies orthogonal wavelet family and follows the approach presented by [35] for image processing and analysis. In [35], the scheme for the extrapolated discrete wavelet transform was particularly designed to generate well conditioned transformation matrices and to have a critically sampled output. The construction of the inverse transform outlined in [35], however, had the drawback of loosing the dyadic structure in case of extrapolated data storage.

Both set of Daubechies and spline filters form a basis for the square-integrable space $L^2(\mathbb{R})$ and are numerically very close to each other [4]. In this sense, the *à trous* and the multiresolution approach of the Cascade Algorithm have been combined in a consistent way in order to perform the undecimated wavelet transform. It should be noted that, due to the choice of the *à trous* wavelet transform with splines filters, the inverse transform on the extrapolated data is performed in an exact manner, completely avoiding the storage of the extrapolated values obtained for each level of the direct transform. Therefore, no Gibb's phenomenon occurs at the boundaries, increasing the confidence zone for the data analysis.

In the present chapter, the proposed non-linear analysis algorithm is then tested using data from simulated spectral energy distribution of stars added to noise with the goal of determining the continuum associated to the spectrum. The continuum determination is similar to the baseline extraction issue in biomedical signal processing applications [16], and also similar to the determination of the coarsest trend in empirical mode decomposition schemes [10], where the mean signal behavior, usually associated to the information with the lowest frequencies (and lowest scales), has to be identified. In the case of stellar spectra, data is often associated to a single or a combination of black-body energy distribution curves (mean trends) affected by other high frequency phe-

nomena such as noise and other perturbations like absorption and emission lines and non-thermal continuum components.

This kind of simulated data is suitable for the demonstration of the efficiency of our extrapolation and analysis technique, since it is a non stationary and non periodical signal with different behaviors at each one of the boundaries, drifted by noise and other influences, which makes the standard extrapolation techniques to fail, as illustrated in our section of numerical experiments.

In Section 2 of this chapter we briefly present the Cascade and the *à trous* formulations for the discrete wavelet transform. In Section 3 we summarize the discussion presented in [11] in order to address the intrinsic boundary extension problem in such a way the scale dependency of the algorithm can be highlighted. This is relevant to enable the complete reproduction of the results when associating the extrapolation procedure to the data-driven *à trous* based algorithm presented in Section 5. Before presenting the main results of this work, a quantitative analysis of the wavelet extension is carried out in Section 4 using known functions to build discrete data sets. In Section 5 we describe an iterative *à trous* coarsening algorithm employing the wavelet extrapolation. This algorithm is then used in Section 6 for continuum determination of simulated noisy spectra with and without features (strong perturbations summed to the signal), validating the data-driven proposed procedure as a robust tool for data analysis. Conclusions are summarized in Section 7.

2. Discrete Wavelet Transform

One of the most important properties involving discrete orthogonal wavelets is the scaling relation for the scale function $\phi(x)$ as well as for the wavelet function $\psi(x)$:

$$\phi(x) = \sum_{k=0}^{N-1} \mathbf{a}[k]\,\phi(2x-k), \;\; \psi(x) = \sum_{k=0}^{N-1} \mathbf{b}[k]\,\phi(2x-k),$$

where $\mathbf{b}[k] = (-1)^k \mathbf{a}[N-1-k]$ and $p = N/2$ is the number of vanishing moments of the wavelet family, which determines the filter values $\mathbf{a}$ and $\mathbf{b}$. The equations for $\phi(x)$ and $\psi(x)$ above are the main relations in the conception of the Cascade algorithm for the direct wavelet transform [17].

Considering the input data vector $\mathbf{c}_m$ given with respect to a fine grid with 2^m points, the direct discrete wavelet transform for one level of decomposition

is given by following relations:

$$\mathbf{c}_{m-1}[n] = \frac{1}{\sqrt{2}} \sum_{k=2n}^{2n+N-1} \mathbf{a}[k-2n]\,\mathbf{c}_m[k]\,, \tag{1}$$

$$\mathbf{d}_{m-1}[n] = \frac{1}{\sqrt{2}} \sum_{k=2n}^{2n+N-1} \mathbf{b}[k-2n]\,\mathbf{c}_m[k]\,, \tag{2}$$

for $n = 0, 1, \ldots, 2^{m-1}-1$, the vector $\mathbf{d}_{m-1}$ contains the wavelet coefficients from the transformation and the vector $\mathbf{c}_{m-1}$ contains the scale coefficients, both at one coarser level $m-1$, discretized with the half amount of points than the finer reference level m.

In order to reconstruct the original vector $\mathbf{c}_m$, considering now as input data both components $\mathbf{c}_{m-1}$ and $\mathbf{d}_{m-1}$ obtained according to (1) and (2), the inverse discrete wavelet transform is given by

$$\mathbf{c}_m[n] = \sum_{k=k_1}^{k_2} \frac{\mathbf{a}[n-2k]\,\mathbf{c}_{m-1}[k] + \mathbf{b}[n-2k]\,\mathbf{d}_{m-1}[k]}{\sqrt{2}}\,, \tag{3}$$

for $k_1 = \lceil \frac{(n-N+1}{2} \rceil$ given by the ceiling function, $k_2 = \lfloor \frac{n}{2} \rfloor$ given by the floor function and $n = 0, 1, \ldots, 2^{m-1}-1$.

2.1. The *à trous* Algorithm

The *à trous* algorithm, also called redundant wavelet transform, is a non-decimated version of the wavelet transform [9, 24]. It modifies the standard decomposition scheme given by (1) and (2) by changing the low-pass and high-pass filters at each consecutive level by introducing 'holes' (*à trous*), i.e., zero values between each of the filter's coefficients. Considering a change of variables, while the number of filter coefficients can be kept unaltered, the function values set for the transform are chosen according to the space step 2^{j-1}, which depends on the scale j. In this sense the holes of the *à trous* scheme are transferred to the function values. The following expressions express this formulation for the direct transform. The wavelet coefficients are straightforward computed as the difference between the low passed signals from two consecutive levels as

$$\mathbf{c}_j[n] = \sum_{k=-s}^{s} \mathbf{h}[k]\;\mathbf{c}_{j-1}[n+2^{j-1}k]\,, \tag{4}$$

$$\mathbf{d}_j[n] = \mathbf{c}_{j-1}[n] - \mathbf{c}_j[n]\,, \tag{5}$$

for $n = 0, 1, \ldots, L-1$, $j = 1, 2, \ldots, J$, where $\mathbf{c}_0$ is the initial data set with L points (usually but not necessarily 2^q points, q being a positive integer), $j = 0$ is now the finest level of resolution, J is the number of decomposition levels and $\mathbf{h}$ is a low-pass filter initially defined with size $2s+1$. The choice of the index to indicate the finest level may change considerably according to the algorithmic formulation of the wavelet transform. In general, for the cascade algorithm, $\mathbf{c}_m$ is considered the vector on the finest resolution level. In the *à trous* algorithm, however, the recursion algorithm is easier to delineate if $\mathbf{c}_0$ is denoted as the finest initial level vector.

The inverse *à trous* transform is simply computed by adding the wavelet coefficients from all levels to the final low-resolution signal as $\mathbf{c}_{j-1}[n] = \mathbf{c}_j[n] + \mathbf{d}_j[n]$ for $n = 0, 1, \ldots, L-1$, $j = 1, 2, \ldots, J$.

It is important to point out that for this transformation all decomposition levels contain the same amount of discrete information and therefore all vectors are the same size as the initial resolution level. It should also be noted that the *à trous* algorithm can also be used with other wavelet filter families, for instance, the bi-orthogonal spline wavelets, interpolating wavelets, etc.

2.2. The Missing Boundary Neighbors Issue

The equations for the direct wavelet transform (DWT) (1), (3) and (4), independently of the chosen algorithm and for the inverse transform in the case with decimation, all require discrete values from the initial vector for indexes j beyond the finite range $j = 0, 1, \ldots, 2^m - 1$ in order to carry out the proper calculations, which constitutes the missing boundary neighbors issue. For the direct transform, the absent positions occur only at the right boundary, beyond the last vector position. The lacking positions for the inverse transform of the cascade algorithm are at the left boundary from both $\mathbf{c}_{m-1}$ and $\mathbf{d}_{m-1}$ vectors, considering a wavelet transform defined by four-point filters $\mathbf{a}$ and $\mathbf{b}$. Naturally, the larger the filter length, the greater the number of missing points needed on both boundaries vicinities.

The same kind of circumstance occurs when the *à trous* algorithm is considered for the direct wavelet transform, only that, in this case, missing data points occur on both exterior boundary vicinities. Furthermore, as the level of the transform increases, even more absent points will be necessary for the transformation due to the scaling factor, as schematically shown in Fig. 2 of [11].

2.3. Boundary Extensions and Related Effects

In order to deal with the missing points issue and calculate the discrete wavelet transform at the boundary vicinities of a given data set two alternatives are possible: either different wavelets filters are constructed for the boundary regions, as proposed by [5] where the entire wavelet family was adjusted to the interval or, else, ghost values for the missing positions (see Fig. 2 in [11]) have to be obtained via any extrapolation procedure, independently of the considered algorithm, Cascade [17] or *à trous* [24].

Even though the data extrapolation may cause some kind of distortion at the boundaries for one reason or another, some known and widely used approaches to extend the original data set for $i = 1, 2, \ldots$ are: the *periodic extension*: $\mathbf{c}_j[0-i] = \mathbf{c}_j[L-1-i]$; the *null extension*: $\mathbf{c}_j[0-i] = \mathbf{c}_j[L-1+i] = 0$; the *linear extrapolation*; $\mathbf{c}_j[0-i] = \mathbf{c}_j[0] + i(\mathbf{c}_j[0] - \mathbf{c}_j[1])$, $\mathbf{c}_j[L-1+i] = \mathbf{c}_j[L-1] + i(\mathbf{c}_j[L-1] - \mathbf{c}_j[L-2])$; the *continuity extension*: $\mathbf{c}_j[0-i] = \mathbf{c}_j[0]$, $\mathbf{c}_j[L-1+i] = \mathbf{c}_j[L-1]$; and the *mirror extension*: $\mathbf{c}_j[0-i] = \mathbf{c}_j[0+i]$, $\mathbf{c}_j[L-1+i] = \mathbf{c}_j[L-1-i]$. The periodic extension is the way periodized wavelet transform is carried out, avoiding the construction of new wavelet basis adapted to boundary conditions. If the considered data is non-periodic itself, the region affected by the periodic continuation depends on the size of the wavelet filter, which is related to the vanishing moments of the wavelet family. The null extension is frequently used in the context of the Fourier transform as an attempt to keep the region of analysis free of the Gibb's phenomenon which also occurs at the boundaries of the Fourier transform. The linear extrapolation as well as the continuity and the mirror extensions will be noticed by the wavelet coefficients around the boundary positions and, due to the decomposition levels, this perturbation will be dragged to all levels of the wavelet transform since the discontinuities in any of the derivatives of the function are detected by the wavelet transform.

3. Wavelet Extrapolation

The aim of the current section is to provide a self-contained presentation of the extrapolation procedure initially proposed in [35] and adapted in [11] for 1D data analysis. The level by level computed extrapolation procedure enables the efficient application of the *à trous* algorithm for the discrete wavelet transform, since its undecimated property is relevant for the final data-driven proposed algorithm. By efficiency we mean the capability of diminishing as much as possi-

ble the boundary effects and distortions occurring in the traditional approaches discussed above and consequently increasing the trusted region of the signal analysis.

The alternative approach we propose for the *à trous* wavelet transform with spline filters is to construct the missing boundary values through an adaptation of the extrapolation strategy presented by [35] where, originally, the extrapolation was developed for the Daubechies wavelet transform and presented in a matricial form associated to the the Cascade Algorithm. Here, no matricial form is considered and the extrapolation obtained through Daubechies wavelet filters is performed as an auxiliary process. Thus the extrapolation is performed level by level in order to generate all missing points necessary to keep consistent the *à trous* formulation. This means that the spacing considered for the *à trous* transform at each level will be preserved in order to pick up points inside the domain to construct the Daubechies extrapolation. For the *à trous* transform, Spline-Wavelet filters are considered.

The fact of considering two different families of wavelets, Daubechies for the extrapolation and Spline-Wavelets for the wavelet transformation itself does not compromise the final result. Since the cubic splines considered for the *à trous* transform are piecewise polynomials functions of order three, at least locally, they can be considered as belonging to the Daubechies scaling functions span spaces. This means that no perturbations are introduced when extrapolating data, avoiding the increase of the wavelet coefficients associated to boundary positions. In fact, spline wavelets belongs to the family of the bi-orthogonal wavelets, i.e., although not orthogonal to its translations, spline wavelets are orthogonal to dual functions, constructed through filters and retaining the same general properties of the primal functions. Cohen et al. [4] present this construction in great detail. One interesting aspect of this bi-orthogonal family is the freedom of choosing different dual functions for the same primal spline function, implying in different possibilities in forming the direct and inverse transforms associated to each spline filter. Another characteristic pointed out by [4] is the fact that Spline wavelet filters and its dual filters are numerically close to Daubechies wavelet filters, expressing how similar these families of wavelets are to each other.

A noticeable advantage of the present *à trous* transform over the Cascade algorithm used by [35] is the fact that the inverse transform is computed in a straightforward manner by simply adding up all components obtained in each decomposition level. This is a remarkable property of the *à trous* algorithm

as opposed to the Cascade algorithm in view of the inverse transform. When extrapolated data is incorporated to the vectors obtained by the wavelet transform, the Cascade algorithm looses its dyadic structure causing also the necessity of recomputing the transform in order to avoid the storage of redundant data (see [35] for more details).

In order to systemize and analyze the core of the proposed extrapolation procedure some free parameters need to be chosen. We consider the initial resolution level m with L points and an orthonormal wavelet function with $p = N/2$ vanishing moments. Therefore, to be able to compute the wavelet transform at these L discrete values independently of the transform algorithm, $N-3+1 = 2(p-1) = N-2$ points need to be extrapolated on the right boundary as well as on the left boundary before the transform can be performed. This implies that for each transformation level $L+2N-4$ function values have to be available. The main assumption for the construction of a polynomial extrapolator is the fact that when a wavelet family with $p = N/2$ vanishing moments is considered, polynomials with degrees up to $p-1$ can be exactly generated as linear combinations of the scaling functions $\phi_{j,k}(x) = 2^{j/2}\phi(2^j x - k)$, at a certain level j. Consequently, the extrapolation function itself can be obtained as a linear combination of the wavelet basis.

As starting point, let the sequence of the scaling coefficients $\mathbf{c}_m[n]$, $n = 0,1,\ldots,L-1$ at the finest resolution level be given as the discrete values of the analyzed function $F(x)$, discretized in a uniform grid $\Gamma : \mathbf{c}_m[n] = F(x_n)$, $x_n \in \Gamma$. Let the scaling functions of the orthonormal wavelet family for the same level m be denoted as $\phi_{m,k}(x) = 2^{m/2}\phi(2^m x - k)$, $k \in \mathcal{Z}$, spanning a subspace $V = \{\phi_{m,k}\}$ of the space of the square-integrable functions, $L^2(\mathbb{R})$. The projection P of $F(x)$ onto V is then given by $PF(x) = \sum_{k\in\mathcal{Z}} \mathbf{c}_m[k]\,\phi_{m,k}(x) = 2^{m/2}\sum_{k\in\mathcal{Z}} \mathbf{c}_m[k]\,\phi(2^m x - k)$. Even though the variable k runs for all values in $\mathcal{Z}$, we are interested just in finite dimensional applications and therefore we are concerned only with coefficients for the positions of the original data, $k = 0,\ldots,L-1$, the positions of the extrapolation for the left boundary at level m, $k = (-N+2)\times 2^m, (-N+2)\times 2^m + 1,\ldots,-1$, and the positions of the extrapolation for the right boundary also at level m, $k = L,\ldots,L-1+(N-3)\times 2^m$.

Under the assumption that $PF(x) \in V$ has a polynomial representation of order $p-1$ in the vicinity of the left and right boundaries, respectively at $x = 0$ and $x = x_{L-1}$, the following expressions defines the relations necessary for the

construction of the extrapolation polynomials on the left and right sides:

$$PF(y) = \sum_{l=0}^{p-1} \boldsymbol{\lambda}_l^{\dagger}\, y^l, \qquad \text{(left boundary)} \tag{6}$$

$$PF(y) = \sum_{l=0}^{p-1} \boldsymbol{\lambda}_l^{\ddagger}\, (y-y_m)^l, \qquad \text{(right boundary)} \tag{7}$$

where $y = 2^m x$. The polynomial coefficients $\boldsymbol{\lambda}_l^{\dagger}$ and $\boldsymbol{\lambda}_l^{\ddagger}$ above can be determined from a system of equations obtained by taking the inner product of (6) and (7) with the M orthonormal scaling functions $\phi(y-j)$ for $j = 0, 1, \ldots, M-1$:

$$\begin{aligned} < PF(y), \phi(y-j) > &= 2^{m/2} \sum_{k \in \mathcal{Z}} \mathbf{c}_m[k] < \phi(y-k), \phi(y-j) > \\ &= \begin{cases} \displaystyle\sum_{l=0}^{p-1} \boldsymbol{\lambda}_l^{\dagger} < y^l, \phi(y-j) >, & \text{(left boundary)} \\ \displaystyle\sum_{l=0}^{p-1} \boldsymbol{\lambda}_l^{\ddagger} < (y-y_m)^l, \phi(y-j) >. & \text{(right boundary)} \end{cases} \end{aligned}$$

The inner product $< y^l, \phi(y-j) >$ (or $< (y-y_m)^l, \phi(y-j) >$) is known as the $\boldsymbol{\mu}[j,l]$ moment of the scaling function ϕ and can be exactly evaluated [35] by the following relations, where $\mathbf{a}$ provides the filter coefficients for the scaling function:

$$\boldsymbol{\mu}[0,0] = \int_{-\infty}^{+\infty} y^0 \phi(y-0)\, dy = 1, \tag{8}$$

$$\boldsymbol{\mu}[0,l] = \int_{-\infty}^{+\infty} y^l \phi(y-0)\, dy = \frac{1}{2\,(2^l-1)} \sum_{i=0}^{l-1} \binom{l}{i} \left[\sum_{k=0}^{N-1} \mathbf{a}[k]\, k^{l-i} \right] \boldsymbol{\mu}[0,i], \tag{9}$$

$$\boldsymbol{\mu}[j,l] = \sum_{i=0}^{l} \binom{l}{i} j^{l-i}\, \boldsymbol{\mu}[0,i]. \tag{10}$$

Since we are considering an orthonormal wavelet basis, scaling functions and wavelets are orthogonal, i.e., $<\phi(y-k), \psi(y-l)> = 0$, $<\phi(y-k), \phi(y-l)> = \delta_{k,l}$ for each $k, l \in \mathcal{Z}$. Wavelets are also orthogonal across scales, i.e., $<\psi(2^i y-k), \psi(2^j y-l)> = \delta_{i,j}\delta_{k,l}$, for each $i, j, k, l \in \mathcal{Z}$. Besides, this wavelet family has the property of p vanishing moments, which implies that polynomials

with degree up to $p-1$ are spanned only by scaling functions, i.e., $<y^l, \psi(y-j)> = 0$ or $<(y-y_m)^l, \psi(y-j)> = 0$, for $l = 0, 1, \ldots, p-1$. Therefore, no additional equations are required and the subsequent systems of equations for the left boundary follows:

$$\mathbf{c}_m[j \times 2^m] \;=\; 2^{-m/2} \sum_{l=0}^{p-1} \boldsymbol{\lambda}_l^{\dagger}\, \boldsymbol{\mu}[j,l]\,, \tag{11}$$

for $j = 0, 1, \ldots, M-1$, and for the right boundary:

$$\mathbf{c}_m[L-1+j \times 2^m] \;=\; 2^{-m/2} \sum_{l=0}^{p-1} \boldsymbol{\lambda}_l^{\ddagger}\, \boldsymbol{\mu}[j,l]\,, \tag{12}$$

for $j = 0, -1, \ldots, 1-M$.

The corresponding systems of equations in the matrix form $2^{-m/2}\mathbf{A}\,\mathbf{X} = \mathbf{B}$ for the polynomial coefficients $\boldsymbol{\lambda}_l^{\dagger}$ and $\boldsymbol{\lambda}_l^{\ddagger}$ are obtained by applying equations (11) and (12) to the listed j values, i.e., for the first and last M points of $\mathbf{c}_m$ with spacing 2^m. Therefore, for the left boundaries we have:

$$\begin{pmatrix} \boldsymbol{\mu}[0,0] & \ldots & \boldsymbol{\mu}[0,p-1] \\ \boldsymbol{\mu}[1,1] & \ldots & \boldsymbol{\mu}[1,p-1] \\ \vdots & \ddots & \vdots \\ \boldsymbol{\mu}[M-1,0] & \ldots & \boldsymbol{\mu}[M-1,p-1] \end{pmatrix} \begin{pmatrix} \boldsymbol{\lambda}_0^{\dagger} \\ \boldsymbol{\lambda}_1^{\dagger} \\ \vdots \\ \boldsymbol{\lambda}_{p-1}^{\dagger} \end{pmatrix} \;=\; 2^{m/2} \begin{pmatrix} \mathbf{c}_m[0\times 2^m] \\ \mathbf{c}_m[1\times 2^m] \\ \vdots \\ \mathbf{c}_m[(M-1)\times 2^m] \end{pmatrix}, \tag{13}$$

and for the right boundary we have:

$$\begin{pmatrix} \boldsymbol{\mu}[0,0] & \ldots & \boldsymbol{\mu}[0,p-1] \\ \boldsymbol{\mu}[-1,0] & \ldots & \boldsymbol{\mu}[-1,p-1] \\ \vdots & \ddots & \vdots \\ \boldsymbol{\mu}[1-M,0] & \ldots & \boldsymbol{\mu}[1-M,p-1] \end{pmatrix} \begin{pmatrix} \boldsymbol{\lambda}_0^{\ddagger} \\ \boldsymbol{\lambda}_1^{\ddagger} \\ \vdots \\ \boldsymbol{\lambda}_{p-1}^{\ddagger} \end{pmatrix} \;=\; 2^{m/2} \begin{pmatrix} \mathbf{c}_m[L-1-0\times 2^m] \\ \mathbf{c}_m[L-1-1\times 2^m] \\ \vdots \\ \mathbf{c}_m[L-1-(M-1)\times 2^m] \end{pmatrix}. \tag{14}$$

There is a certain flexibility in choosing the parameter M. For $M \neq p$ the above set of equations can be solved using a minimum least squares approach by transforming the systems (13) and (14) into square systems through $2^{-m/2}(\mathbf{A}^{\mathrm{T}}\mathbf{A})\,\mathbf{X} = \mathbf{A}^{\mathrm{T}}\mathbf{B}$. The resulting set of equations can then be solved such that $\mathbf{X} = 2^{m/2}(\mathbf{A}^{\mathrm{T}}\mathbf{A})^{-1}\mathbf{A}^{\mathrm{T}}\mathbf{B}$. According to [35], one suitable choice for the extrapolation parameter M is $M = N = 2p$ and in this work we adopt the same choice for the M parameter.

Denoting $\boldsymbol{\xi}^{\dagger}[l,i]$ and $\boldsymbol{\xi}^{\ddagger}[l,i]$ the elements of the corresponding $p \times M$ matrices $(\mathbf{A}^{\mathrm{T}}\mathbf{A})^{-1}\mathbf{A}^{\mathrm{T}}$ from $\mathbf{X} = 2^{m/2}(\mathbf{A}^{\mathrm{T}}\mathbf{A})^{-1}\mathbf{A}^{\mathrm{T}}\mathbf{B}$, we obtain the following relations for the polynomial coefficients $\boldsymbol{\lambda}_l^{\dagger}$ and $\boldsymbol{\lambda}_l^{\ddagger}$, i.e., the solution of systems (13) and (14):

$$\boldsymbol{\lambda}_l^{\dagger} = 2^{m/2} \sum_{i=0}^{M-1} \boldsymbol{\xi}^{\dagger}[l,i]\, \mathbf{c}_m[i \times 2^m], \tag{15}$$

$$\boldsymbol{\lambda}_l^{\ddagger} = 2^{m/2} \sum_{i=0}^{M-1} \boldsymbol{\xi}^{\ddagger}[l,i]\, \mathbf{c}_m[L-1-i \times 2^m]. \tag{16}$$

for $l = 0, 1, \ldots, p-1$.

Considering all the above relations, we are now able to extrapolate the function F to obtain discrete approximations for positions beyond the left boundary of $\mathbf{c}_m$. Using (15) and (16) respectively into (11) and (12), the exterior scaling functions coefficients $\mathbf{c}_m[k]$ on level m (2^m spacing) for the left boundary are given by:

$$\mathbf{c}_m[j \times 2^m] = \sum_{l=0}^{p-1} \sum_{i=0}^{M-1} \boldsymbol{\mu}[j,l]\, \boldsymbol{\xi}^{\dagger}[l,i]\, \mathbf{c}_m[i \times 2^m], \tag{17}$$

for $j = -N+2, -N+1, \ldots, -1$, and for the right boundary by:

$$\mathbf{c}_m[L-1+j \times 2^m] = \sum_{l=0}^{p-1} \sum_{i=0}^{M-1} \boldsymbol{\mu}[j,l]\, \boldsymbol{\xi}^{\ddagger}[l,i] \times \mathbf{c}_m[L-1-i \times 2^m], \tag{18}$$

for $j = 1, 2, \ldots, N-2$.

4. Analysis of the Extrapolation Procedure

Prior to merging the extrapolation scheme presented in the previous section with the *à trous* transform, we illustrate the extrapolation scheme functionality and verify its accuracy with respect to the error in euclidean norm by applying it to three different sources of discrete data sets: 1) a polynomial function for which extrapolation values are expected to be exact; 2) a sine function as a basic example of continuous periodic function and 3) an arbitrary scale blackbody spectral energy distribution function per unit of wavelength f_λ given by the Planck's law $f_\lambda = \alpha/[\lambda^5 (e^{\beta/\lambda} - 1)]$, where α is a normalization constant and

$\beta = hc/k_B T_{\text{eff}}$ is a parameter dependent on the black-body effective temperature T_{eff} (c is the speed of light, h is the Planck constant and k_B is the Boltzmann constant), as a basic continuum tracer for the spectrum of stars, star clusters and normal galaxies. This sort of data, added with Gaussian noise, will be further analyzed in the following sections where the extrapolation procedure will be performed in association to the *à trous* wavelet transform in an iterative way in order to minimize the border effects during the decompositions in scale (level).

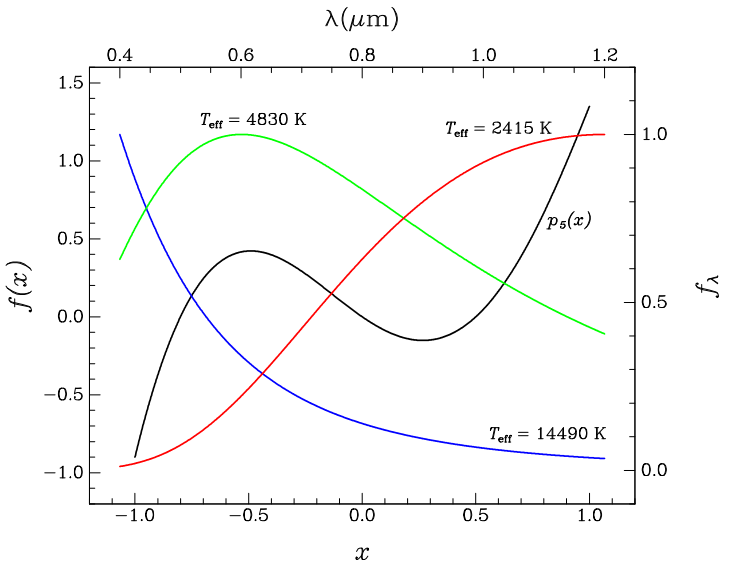

Figure 1. Display of the data sets used to test the extrapolation algorithm. The 5$^{\text{th}}$ order polynomial function $p_5(x)$ used in Example 1 is shown by the black solid for the lower$-x$ and left$-y$ scales while the black-body spectral energy distributions used in Examples 3, 4 and 5 are shown by the solid blue, green and red lines as a function of the wavelength λ from 0.4 μm to 1.2 μm for the upper$-x$ and right$-y$ scales. These curves correspond to energy distributions with maximum flux $f_\lambda^{\max}$ at 0.2 μm (blue line), 0.6 μm (green line) and 1.2 μm (red line), respectively for black-body effective temperatures T_{eff} of 14490 K, 4830 K and 2415 K. For visualization purposes, the flux f_λ has been normalized with respect to the maximum relative flux within the wavelength range displayed.

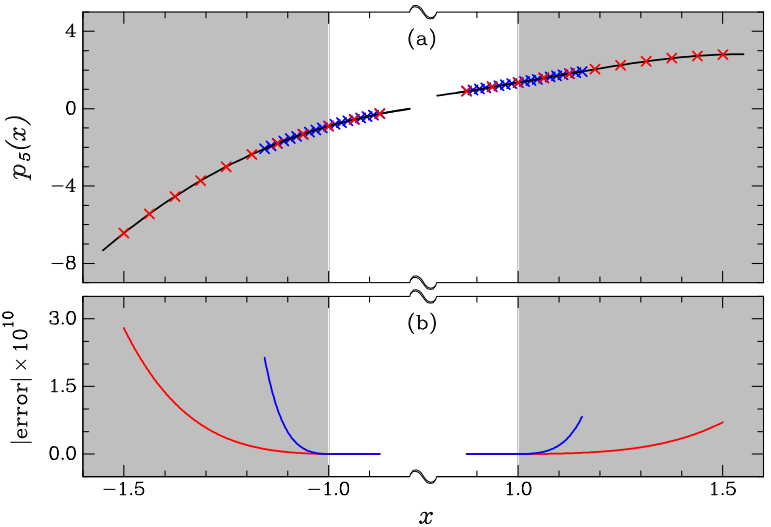

Figure 2. Extrapolation results for the Example 1 case ($p_5(x)$). Only the regions around left and right boundaries at $x = -1$ and $x = 1$ are displayed. Panel (a): the black line is the original $p_5(x)$ data set and the points obtained by the extrapolation procedure for the number of vanishing moments $p = 6$ are shown by blue times symbols ($\times$) for the scale parameter $j = 3$ (2^3 spacings) and in red for $j = 5$ (2^5 spacings). The zones where the extrapolation actually occurs are outlined by gray backgrounds as opposed to white background zones where points displayed are the original data set points. In panel (b) the blue and red lines display the absolute difference between the results obtained and the original data set, respectively for $j = 3$ and $j = 5$. As expected for a pure polynomial function with degree less or equal to p, the absolute errors are negligible, in the order of 10^{-10}, and increase monotonically with distance to the boundary.

The number of points at the starting (finest) resolution level for all the examples will be given by $L = 2^{10}$. We point out that when applying the extrapolation equations, the M known point values considered to construct the systems (13) and (14) must all be interior points in order to avoid seeking data points beyond the opposite boundary (see $\mathbf{c}_m$ indexes in (13) and (14)). This imposes a constraint to the maximum number of decomposition levels η one can consider depending on the number of data points L and on the chosen wavelet (since

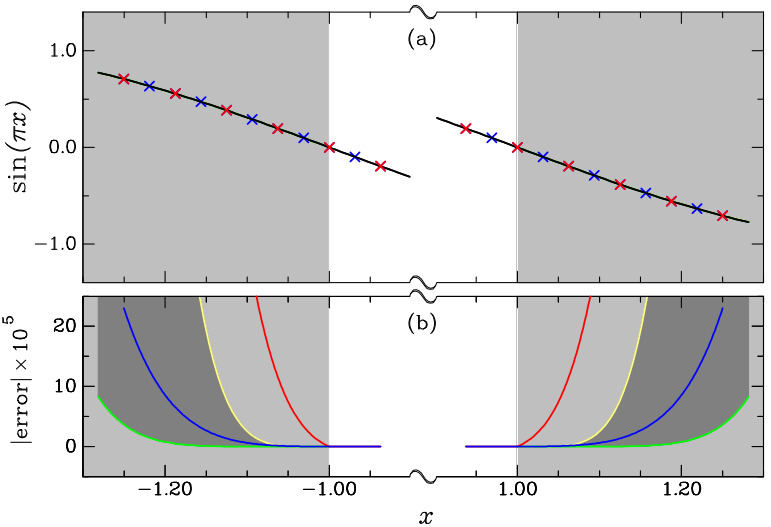

Figure 3. Same as Fig. 2 for the Example 2 case ($\sin(\pi x)$). In addition to the extrapolation points obtained using $p = 8$ and $j = 4$ (blue $\times$ points) and $j = 5$ (red $\times$ points), we also show in panel (a), for comparison, Taylor polynomial approximations of degree 3 (yellow line) and 5 (green line) for the $\sin(\pi x)$ function around points $x = -1$ and $x = 1$. In panel (b) the errors with respect to the original data set (black line in panel (a)) are shown by blue and red lines, respectively for $j = 4$ and $j = 5$, and in yellow and green lines for the 3 and 5 degree polynomial approximations. The darker gray background regions, delimited by the errors curves from the Taylor approximations, show clearly that the absolute errors for the $j = 4$ spacings case, corresponding to extrapolation polynomials of degree $p - 1 = 3$, are comparable to the expected errors for the Taylor polynomials of degree 3 and 5, in the order of 10^{-5}.

$M = 2p$) such that $L \geq 1 + (2p - 1) \times 2^{\eta - 1}$. In the present case, for $p = 3$ and $L = 1024$, we have $\eta \leq 8$. Therefore, the extrapolations are performed according to a given scale parameter $j \leq \eta = 8$ which, in turn, sets the spacing 2^j between stencil points considered in the extrapolation procedure. This scale parameter j allows one to easily determine where the necessary extrapolated values (missing points) occur beyond the boundaries for any given stencil spacing, which is an essential piece of information, particularly when the extrapolation is associated

to the *à trous* transform. Besides the value of the scale parameter j, we also analyze in this section the influence of the choice of the number of vanishing moments p of a wavelet function which determines the polynomial order $p-1$ of the data projection onto the V space (equations (6) and (7)).The data sets used in this section (except for the obvious $\sin(\pi x)$ function) can be visualized in Fig. 1 which shows the polynomial function $p_5(x)$ used in Example 1 (black line) and the black-body energy distribution functions used in Examples 3, 4 and 5, corresponding to effective temperatures T_{eff} of 2415 K (blue line), 4830 K (green line) and 14490 K (red line), respectively.

4.1. Example 1

In this first example of the extrapolation procedure we have taken an arbitrary 5^{th} order polynomial $p_5(x) = 0.25\,x\,(x-0.5)\,(x+0.8)\,(2.0-x)\,(x+5.0)$ for $x \in [-1,1]$ as the source for the data set with 1024 discrete points. Fig. 2 presents the extrapolation results (panel (a)) and the corresponding relative errors (panel (b)) on both boundaries considering a wavelet function with $p=6$ vanishing moments. The data points (extrapolated or not) are shown by times symbols ($\times$) while the $p_5(x)$ curve is shown by black lines. Results for two choices of the scale parameter j are presented: $j=3$ (blue points) and $j=5$ (red points), corresponding to stencil spacings of 8 and 32 points, respectively. The zones where the extrapolation actually occur are marked by gray backgrounds whereas in the white background zones the original data set points are displayed. As expected for a polynomial data set with degree less or equal to the number of vanishing moments p, the absolute errors shown in panel (b) are negligible, in the order of 10^{-10}, and increase monotonously with the distance of the extrapolated point to the boundary.

4.2. Example 2

In this case the source of the discrete data set is taken from a $\sin(\pi x)$ function for $x \in [-1,1]$. The extrapolated results for $p=8$ vanishing moments and scales $j=4$ and $j=5$ (2^4 and 2^5 stencil spacings, respectively) are shown in panels (a) and (b) of Fig. 3. In addition to the blue ($j=4$) and red ($j=5$) points, we present for comparison Taylor polynomial approximations of degree 3 (yellow line) and 5 (green line) for the $\sin(\pi x)$ function around points $x=-1$ and $x=1$, i.e., around the corresponding boundary points. The absolute errors presented in panel (b), in the order of 10^{-5}, show that the results obtained for the $j=4$ choice

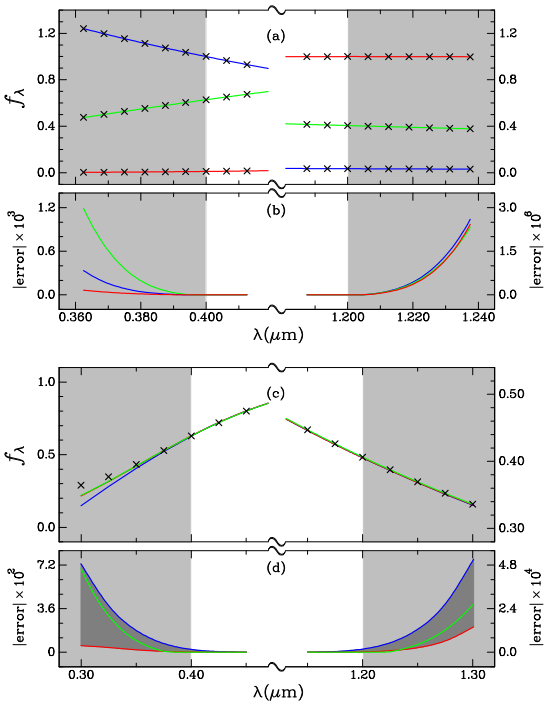

Figure 4. Same as Fig. 2 for the Examples 3, 4 and 5 cases, namely, black-body energy distribution functions from 0.4 μm to 1.2 μm. The extrapolation procedure was applied using $p = 4$. In panels (a) and (b) we show the extrapolation results (black $\times$ points) for the $j = 3$ scaling for the 3 cases of effective temperatures T_{eff}: 14490 K (blue line), 4830 K (green line) and 2415 K (red line). The corresponding absolute errors in panel (b) are in the order of 10^{-3} in the left boundary and in the order of 10^{-6} in the right boundary. In panels (c) and (d) we present the results for $j = 5$ scaling for the $T_{\text{eff}} = 4830$ K black-body case (green line). As in Fig. 3, we also present, for comparison, Taylor polynomial approximations of degree 4 (blue line) and 5 (red line) for the black-body energy distribution function f_λ around $\lambda_0 = 0.5$ μm for the left boundary and around $\lambda_0 = 1.1$ μm for the right boundary. The errors of the extrapolation points in panel (d) (green line) occur right within the darker background region delimited by the blue and red error lines from the Taylor approximations.

are comparable to the Taylor approximations presented – the errors occurring within the region delimited by the error curves from the 3rd and 5th order Taylor polynomials (darker gray background).

4.3. Examples 3, 4 and 5

The last examples used to verify the extrapolation algorithm functionality refer to 3 cases where source of data is taken from the spectral energy distributions f_λ of a black-body at a given effective temperature T_{eff} for $\lambda(\mu m) \in [0.4, 1.2]$, as illustrated in Fig. 1. This set of numerical experiments probe the performance of the extrapolation procedure when the source of data is neither a polynomial nor a periodic function, testing to the limit the capacity of the algorithm to emulate the behavior of the data function beyond the original data domain. The results for the Daubechies functions with $p = 4$ and $j = 3$ scaling (2^3 spacings) are presented in panels (a) and (b) of Fig. 4 for $T_{\text{eff}} = 14490$ K (blue line), 4830 K (green line) and 2415 K (red line). The absolute errors shown in panel (b) are quite small, in the order of 10^{-3} in the left boundary and 10^{-6} in the right boundary, considering that the number of vanishing moments $p = 4$ is not so large, i.e., extrapolation polynomials of degree 3. The worst result among these three data sets is for the black-body function with $T_{\text{eff}} = 4830$ K (green line), mostly because the spectral energy distribution in this case is not a strictly increasing or decreasing function of λ as for the other two cases (See Fig. 1) – circumstances which would favor the extrapolation. Results for a more demanding situation are presented in panels (c) and (d) of Fig. 4 for this $T_{\text{eff}} = 4830$ K case for which the extrapolated points have been taken even further away from the boundaries by a $j = 5$ scaling or 2^5 spacings. Even though the absolute errors are somewhat larger than the corresponding $j = 3$ case, in the order of 10^{-2} in the left boundary and 10^{-4} in the right boundary, they are comparable to the expected errors from Taylor expansions of degree 4 and 5 for the black-body function f_λ around $\lambda_0 = 0.5$ μm for the left boundary and around $\lambda_0 = 1.1$ μm for the right boundary, as can be seen in Fig. 4d, being in fact smaller than the errors from the 4th order Taylor expansion (blue line).

4.4. Discussion

The effect of the scale parameter j and the number of null moments p on the value of the extrapolated points can be outlined by the content of Table 1 which shows the negative log of the absolute error (i.e., the magnitude of the error)

in the euclidean norm for the first extrapolated point on both boundaries as a function of j and p for all five data sets analyzed. We point out that 'first extrapolated point' does not necessarily mean a close point to the border once its distance depends on j by 2^j spacings. In general, the errors on Table 1 increase as j increases and decreases as p increases as expected, reaching minimum values at $p = 6$. The error values for $p = 8$, on the other hand, should be taken with some skepticism. In fact, results free of systematic errors for values of $p > 7$ can be quite difficult to obtain using the extrapolation equations (17) and (18) due to the existence of very large numbers in the matrices $\mathbf{A}^{\mathrm{T}}\mathbf{A}$ (coming from the moment matrices $\boldsymbol{\mu}$) which need to be inverted in the calculation of matrices $\boldsymbol{\xi}^{\dagger}$ and $\boldsymbol{\xi}^{\ddagger}$. The conditional number of matrix $\mathbf{A}^{\mathrm{T}}\mathbf{A}$ can be as low as 10^{-15} for $p \geq 8$. This difficulty persists even if equations (13) and (14) are solved without explicit matrix inversion as in a LU decomposition. The presence of systematic errors in the results of Table 1 is evidenced by the increase of the error values when p increases from 6 to 8, specially for the $p_5(x)$ case.

The examples above show that, even though we are not looking for an extrapolation method *per se* but rather a viable mechanism capable to provide missing data beyond boundaries so that a wavelet transform can be carried out on the entire data set without special filters for the boundaries, the extrapolation algorithm proposed in Sect. 3 has proven to be effective and can produce quite acceptable results when the number of null moments p is properly set. The assumption made there that the projection of the data set onto V_m has a polynomial representation is fully supported by the results for the $p_5(x)$ data set and the comparison between the data from the other examples and the corresponding Taylor approximations. In addition to that, the results for the $\sin(\pi x)$ and $T_{\mathrm{eff}} = 4830$ K black-body cases show that the extrapolation values are comparable to corresponding Taylor approximations (Figs. 3b and 4d).

5. Wavelet Extrapolated *à trous* Transform

The construction presented in the previous sections took into account the orthonormal Daubechies wavelet family and its capacity to exactly represent polynomials in scaling function bases (vanishing moments property) in order to devise an extrapolation procedure to generate points beyond both data set boundaries. With this procedure in hand, we now turn our attention to the *à trous* wavelet transform. Even though the filters for the *à trous* wavelet transform are not the Daubechies filter family but rather the Bi-orthogonal Spline wavelet

Table 1. Negative log of the absolute euclidean errors for the first extrapolated point on the left and right boundaries as a function of the number of vanishing moments p and scale parameter j for the five data sets analyzed

data	j	$-\log(\lvert\text{error}\rvert)$, left boundary				$-\log(\lvert\text{error}\rvert)$, right boundary			
p		2	4	6	8	2	4	6	8
	1	5.55	8.10	11.72	9.65	5.52	7.40	12.27	10.13
$p_5(x)$	3	4.10	6.19	10.97	8.64	4.08	5.47	11.57	9.13
	5	2.45	4.09	10.08	7.49	2.45	3.32	10.68	7.99
	1	5.34	8.67	11.89	10.41	5.34	8.67	11.91	11.46
$\sin(\pi x)$	3	3.89	6.28	8.40	9.28	3.89	6.28	8.40	10.18
	5	2.25	3.67	4.74	5.85	2.25	3.67	4.74	5.85
black-body	1	6.27	8.01	10.20	10.17	8.20	10.16	13.81	12.31
$T_{\text{eff}} =$	3	4.81	6.22	7.40	8.74	6.74	8.21	10.87	11.25
2415 K	5	3.15	4.49	4.57	5.32	5.08	5.99	7.49	8.60
black-body	1	5.68	7.09	10.08	9.83	7.71	9.83	12.61	11.27
$T_{\text{eff}} =$	3	4.25	5.17	7.36	8.46	6.26	7.85	9.98	10.46
4830 K	5	2.66	3.06	6.00	4.97	4.63	5.56	6.62	8.17
black-body	1	6.27	8.43	11.13	11.44	6.97	9.75	12.47	10.04
$T_{\text{eff}} =$	3	4.82	6.35	7.95	9.27	5.51	7.89	9.67	9.05
14490 K	5	3.20	3.97	4.70	5.87	3.87	6.22	6.37	8.04

family as considered in [24], splines are polynomials (at least piecewise) and therefore they can be exactly represented by the Daubechies basis used in the extrapolation procedure, regarded that the number of vanishing moments p should be greater than the degree of the spline in consideration. As the smoothness of the polynomial functions generating extrapolated points is also determined by p, data at the boundaries should be smooth enough not to drag perturbations inside the domain for the entire set of decomposition levels. Therefore, once the extrapolation is carried out level by level, the *à trous* transform would neither be biased by the spline wavelet filters nor be affected by spurious errors for the analyzed data, which characterizes an harmonious match between the two heuristics where border effects are diminished in an optimized way.

As already mentioned, one of the characteristics of the *à trous* formulation is the simple way direct and inverse transforms are calculated. This simplic-

Algorithm 1 Iterative *à trous* coarsening algorithm via a wavelet extrapolation boundary extension. The input parameters are the input data vector $\mathbf{c}_{0,0}$, the input data size $L_m = 2^{J_{max}}$, the spline wavelet filter $\mathbf{h}$, the wavelet filter size $r = 2 \times s + 1$, the maximum number of decomposition levels η and the trend tolerance tol. The output parameters are the family of decomposition levels $\mathbf{d}_{\eta,k}$, the family of the coarsest levels (trends) $\mathbf{c}_{\eta,k}$ and the sum of trends $\mathbf{st}$.

1: $\mathbf{st} \leftarrow 0$; $\mathbf{d}_{\eta,0} \leftarrow 0$; $k \leftarrow 0$
2: $variation \leftarrow 2 \times tol$; $\mathbf{residue}[0] \leftarrow 0$
3: **while** $variation > tol$ **do**
4: **for** $n = 1, 2, \ldots, \eta$ **do**
5: $scale \leftarrow 2^{n-1}$
6: boundary_extrapolation($\mathbf{c}_{n-1,k}, scale, n$)
7: **for** $j = 0, 1, \ldots, L_m - 1$ **do**
8: $\mathbf{c}_{n,k}[j] \leftarrow 0$
9: **for** $i = -s, -s+1, \ldots, s$ **do**
10: $\mathbf{c}_{n,k}[j] \leftarrow \mathbf{c}_{n,k}[j] + \mathbf{h}[i] \times \mathbf{c}_{n-1,k}[j + i \times scale]$
11: **end for**
12: $\mathbf{d}_{n,k}[j] \leftarrow \mathbf{c}_{n-1,k}[j] - \mathbf{c}_{n,k}[j]$
13: **end for**
14: **end for**
15: $\mathbf{c}_{0,k+1} \leftarrow \mathbf{c}_{0,k} - \mathbf{c}_{\eta,k}$
16: $\mathbf{st} \leftarrow \mathbf{st} + \mathbf{c}_{\eta,k}$
17: $\mathbf{residue}[k+1] \leftarrow max(|\mathbf{d}_{\eta,k} - \mathbf{d}_{\eta,k-1}|)$
18: $variation \leftarrow |\mathbf{residue}[k+1] - \mathbf{residue}[k]|$
19: $k \leftarrow k + 1$
20: **end while**

ity is preserved in the case of the extrapolation procedure considering that it requires just one additional step to the basic *à trous* routine as outlined by Algorithm 1 in lines numbered 4–14. The additional step is the call to the procedure boundary_extrapolation ($\mathbf{c}_{n-1,k}, scale, n$) in line 6 with proper parameters to calculate the extrapolation points needed for the *à trous* transform at level n on both boundaries, as described in Sect. 3. The parameter *scale* is used to control the 'holes' of the *à trous* transform according to the level n, as well as the spacing between points sorted out inside the data domain to build the stencil for the

construction of the extrapolation. Regarding the size of the Daubechies filters $N = 2p$ and the size of the Spline filters $r = 2s+1$, we claim (Sect. 3) that the choice for the number of vanishing moments for the Daubechies wavelet should be $p \geq (s+2)/2$, since the number of extrapolated values on each boundary is $N-2 = 2p-2$ and this would be enough for covering the s values required for the *à trous* transform on the boundaries.

The Algorithm 1 as a whole has been coded based on [31] to obtain the sum **st** of the coarsest *à trous* levels η by an iterative loop (indexed by k) which removes each coarsest level $\mathbf{c}_{\eta,k}$ from the current input data $\mathbf{c}_{0,k}$ until the maximum absolute difference (residue) between two consecutive decomposition levels is smaller than a given tolerance *tol*, i.e., until no significant variation of the details $\mathbf{d}_{\eta,k}$ can be found in the coarsest level. The sum **st** converges to a smooth featureless data array, or mean trend, corresponding to the convolution between the input data and a broadband filter.

This mean trend **st** can be quite useful, for example, to identify low frequencies components in data or to obtain the continuum of a spectrum. For instance, an important application in bio-medical signal analysis is the removal of the 'baseline' component from ECG [12, 21], which allows a better understanding of the high frequency contributions. In the case of the input data being a stellar like spectrum, the **st** trend would closely resembles the continuum of the spectrum. In fact, as shown by [31], this is a very effective approach to the often arduous problem of obtaining the continuum of noisy spectra in comparison to polynomial fitting or filter smoothing techniques, particularly when the spectrum shows emission lines or broad absorption bands. These features are usually blanked out prior to the fitting when their presence is conspicuous enough or ignored when they are too shallow to be distinguished from the continuum background, resulting in error in the continuum determination on both cases.

6. Numerical Simulations

In order to verify the performance of our boundary treatment strategy we present in this section results obtained from applying the *à trous* coarsening Algorithm 1 to simulated spectra for which the efficacy of the extrapolation procedure can be evaluated in the case of determining the continuum of the spectra over the entire data set available.

6.1. Featureless Noisy Spectra

As a simple first test to determine the continuum we have taken the three blackbody spectral energy distributions presented in Sect. 4 ($T_{\text{eff}} = 2415$ K, 4830 K and 14490 K) with $L = 2^{10} = 1024$ points as input data $\mathbf{c}_0[0,\ldots,L-1]$ and added gaussian noise to obtain simulated spectra with signal-to-noise ratios (SNR) of 100, 150 and 50, respectively.

As featureless noisy spectra, this sort of data is ideal to test the performance of the extrapolation procedure since the effects from spectral characteristics like strong emission and/or absorption lines or broad-band features will not be present, particularly when the extrapolation scheme is to be compared with other (traditional) boundary extension conditions. Fig. 5 presents in panel (a) the simulated spectra (black lines) and the continua obtained by Algorithm 1 with $p = 3$ and $tol = 0.01$ using three usual extensions discussed in Sect. 2.3, namely, a null boundary extension (light gray lines), a mirror extension (green lines) and a continuity extension (blue lines), as well as the continuum obtained with the wavelet extension from the extrapolation procedure (red lines). The number of decompositions levels η used in each case was chosen according the amount of noise present in the simulated spectra: $\eta = 6$ for SNR $= 150$ ($T_{\text{eff}} = 4830$ K case) and $\eta = 7$ for SNR $= 50$ and 100 ($T_{\text{eff}} = 14490$ K and 2415 K cases). The corresponding errors, i.e., the difference between the true and the obtained continuum, are shown in panel (b) of Fig. 5. Apart from the results for the null extension (light gray lines) which can be quite bad near the boundaries, the errors found for all other cases are considerably small, in the order of 0.2 per cent or less.

6.2. Discussion

The first noticeable aspect in Fig. 5 is that, depending on the behaviour of the continuum near the edges, a simple boundary extension can indeed produce a convincing result over a wide range of data points, as long as the proper type of boundary extension has been selected. For instance, the null extension choice (light gray lines) only works well when the data obviously approach small values near the boundaries, as in the cases $T_{\text{eff}} = 2415$ K and 14490 K for the left and right boundaries, respectively. It is also evident that an extension type can work well for one edge and not so well for the other edge as seen in the results for the continuity (blue lines) and mirror (green lines) extensions choices for the $T_{\text{eff}} = 4830$ K and 14490 K cases. Therefore, a suitable single choice of one of

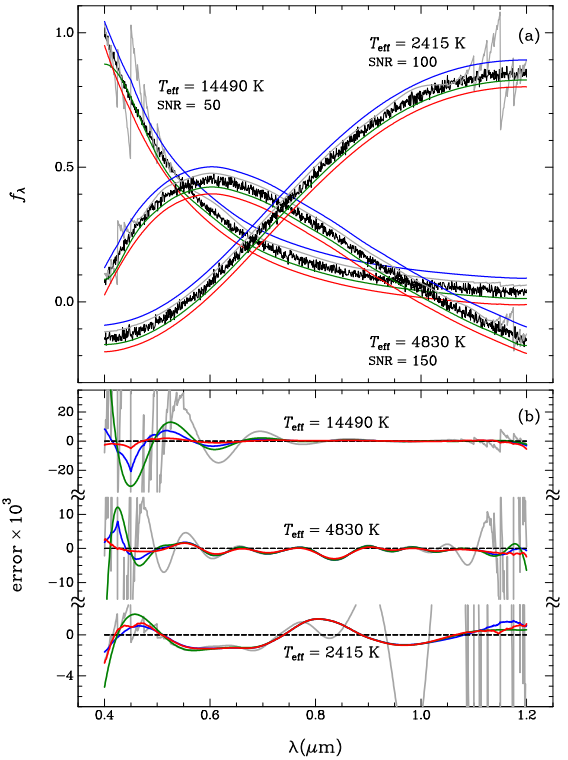

Figure 5. Continua results for simulated featureless spectra obtained using the *à trous* coarsening Algorithm 1 with distinct boundary extension conditions. The input data used were the black-body spectral energy distributions from Examples 3, 4 and 5 of Sect. 4 added with Gaussian noise with different signal-to-noise ratios (SNR), resulting in the black lines shown in panel (a), as indicated. The continua obtained are shown by light gray curves for the null extension, green curves for the mirror extension, blue curves for the continuity extension and red curves for the wavelet extrapolation extension. The curves in panel (a) have been arbitrarily moved up or down to help visualizing the data. The difference (error) between the true continua and the obtained continua are shown in panel (b) with the corresponding color. A black dashed line marks the zero of the scale for each of the three cases.

those boundary extensions or a combination of extensions, i.e., a different one for each boundary, that would lead to an acceptable continuum for the entire data array may not exist at all for a given spectrum.

The effects of a poor boundary extension choice can extend to points distant from the edges as shown in the results for the null, mirror and continuity extensions for the $T_{\text{eff}} = 14490$ K case (SNR = 50) in the left half of the spectra. This is due to a 'dragging effect' over data values caused by the iterative nature of the *à trous* coarsening algorithm. For a data array of size $L = 1024$ and filter size $r = 5$ (cubic spline wavelet) one can apply the *à trous* transform for the center half of the points up to 8 levels of decomposition prior to using data from extrapolated points. In the case of the coarsening algorithm, this is true only for the first iterative step of the process as subsequent steps will perform the *à trous* transform over a data array that has been subtracted from its coarsest level whose points near the edges were calculated using values provided by the boundary extension.

Thus, contrary to what one might expect, rather than minimize or being compensated by, the dragging effect is actually enhanced by the iterative process when the boundary extension is not appropriate. So, the effect can propagate itself far away from the edges into region that one may naively perceive as a wavelet transformed safe zone. The net outcome will depend on the various parameters involved in the whole iterative coarsening process like the number of data points L, the maximum number of decompositions η, the number of vanishing moments p of the wavelet family, the type and size r of the wavelet filters and choice of boundary extension, not to mention noise and shape of the data array. For instance, for the $T_{\text{eff}} = 4830$ K and 2415 K cases that have better signal-to-noise ratios (SNR = 150 and 100, respectively) the dragging effect is less intense even though it occurs on both edges.

The results obtained with the wavelet extension (red lines) are quite reasonable and justify our proposition of carrying out an extrapolation scheme per level of the *à trous* transform to generate missing points beyond data boundaries. The curves provide an overall best fitting for the continuum in all three cases on both boundaries and are much less affected by the dragging effect. The average error is very consistent, in the order of 0.1 per cent, independent of the amount of noise present in the input data. This is particularly evident in the $T_{\text{eff}} = 14490$ K case for which SNR = 50 is relatively low.

The parameters p and tol were found to have only a marginal influence over the qualitative and quantitative character of the results above. No apparent

improvement could be obtained by using a value for p larger than the required minimum of 3. The tolerance value $tol = 0.01$ used for all the tests would induce a relatively small number of iterations, around 15 on average. The choice of the maximum number of decomposition levels η, though, is more subtle, being a trade-off between a high value, enough to remove the noise signature (details) from the resulting continuum, and a low value, desirable in order to minimize the dragging effect. Hence, in the above examples we have used $\eta = 6$ for the $T_{\text{eff}} = 4830$ K case (SNR= 150) and $\eta = 7$ for the $T_{\text{eff}} = 14490$ K and 2415 K cases (SNR= 50 and 100).

6.3. Noisy Spectra with Features

The presence of features in the spectrum may influence considerably the determination of the continuum through wavelet decomposition techniques since features, contrary to noise, contain a very distinct curve shape characterized by the presence of low frequency components (large scale information) around its location in the spectrum. This kind of signal is detectable in all wavelet transform scales and remains perceptible through the scaling coefficients of the lowest scale of the wavelet transform, affecting the continuum determination [31]. To trace a parallel with ECG signals, features are comparable to QRS complexes which, in certain analysis, have also to be removed in order to allow the recognition of other data components. The obvious approach in this situation is to identify the features, obtain fitting models to the corresponding data points and then subtract them from the data, all that prior to the continuum determination. This implies in arbitrarily choosing several additional parameters like the overall shape of the fitting model for each feature, the number of features in case of wide bands, constraints between modeling parameters and so on, not to mention the shape of the continuum itself around the features. Even though one may find many sophisticated algorithms to executed this task [1], we propose here an alternative to feature removal prior to continuum determination, considering the interpolating properties of the wavelet transform when the details involved are null.

By analyzing wavelet transform steps one notes that, essentially, the main step is to predict function values on a finer resolution level using values one level below. In this sense the predicted approximation is the one obtained by the convolution with the wavelet filters and the function values – the wavelet coefficient being the difference between the original value and the predicted one.

Nevertheless, the prediction procedure can be used instead to produce values in even finer resolution levels, without introducing any extra variations to the original data (in the sense of wavelet variations) since wavelet coefficients are all assumed to be zero. Therefore the wavelet transform can also be used as a tool for locally producing smooth values in regions where features need to be removed. Therefore we execute a very simple yet efficient iterative procedure as follows: 1) replace the data points around each feature with an initial continuum approximation; 2) execute Algorithm 1; 3) use the results from the previous step to define new continuum for the features; 4) repeat steps 2–3 until two consecutive continuum approximations for the features differ less than a given tolerance. This loop converges first because any possible discontinuities for the continuum approximation of the features occur at their edges, being captured by the details in different levels until their contribution no longer counts for the scaling coefficients in the last levels of the transform, and second because the absence of details in the feature's continuum approximations will force an interpolation for the data points with their surroundings, providing a self-consistent continuum approximation for the features. This heuristic requires no information about the (possible) features other than their location in the spectrum.

In Fig. 6 we illustrate the effects of strong line features in the continuum determination and the results obtained when the iterative procedure described above is employed. As input data we have used the spectral energy distribution from Example 4 (Sect. 4, $T_{\text{eff}} = 4830$ K case) added with gaussian noise with a signal-to-noise ratio of 200 and gaussian profiled features with relative intensity 0.3 and -0.4, respectively at 0.50 μm and 0.65 μm, as well as a shallow wide band built from the superposition of 10 gaussian profiles with relative intensity of -0.02 spread evenly from 0.985 μm to 1.030 μm. The gaussian profiles were made with FWHM = 0.001 μm. In panel (a) it is shown the simulated spectrum (black curve) and the resulting continua obtained using Algorithm 1 for $p = 3$, $\eta = 6$ and $tol = 0.001$ with and without feature removal, respectively, by the red and blue lines. In panel (b) the corresponding errors with respect to the true continuum are displayed. The blue curve show a typical outcome for the continuum (feature's residues and symmetric wings) when no data treatment for presence of strong or wide features in the spectrum is attempted. Even a shallow feature like the wide absorption band at 1.0 μm can have a significant impact on the resulting continuum. The red curve show the results for the same input data when features are treated as described above. The orange line segments show the initial continua approximations used to replace the data around each feature.

The green curve shows the input data with the final continua obtained for each feature (noiseless segments). The resulting errors are quite negligible, less than 0.3 per cent, and no systematic effects can be found in the residues, not even for the strong features for which a rough constant initial continuum approximation was used. These results were obtained using an absolute tolerance of 0.001. The number of iterations was around 80 for the above procedure and around 10 for Algorithm 1.

6.4. Final Remark

During the construction and analysis of the numerical simulations for this work it became clear that continuum results near boundaries for any extension type used could be improved if a local average between the first few data points was carried out prior to the first level of wavelet decomposition. This average would diminish the impact of noise on the boundary analysis – in particular for those cases (not shown) of low signal-to-noise ratios (SNR < 30) – by promoting a softer transition between the extrapolated smooth data in the extension side of the boundary and the noisy data in the other side.

Conclusion

In this work we have applied an alternative approach to the boundary extension problem by means of an extrapolation technique for one-dimension data sets using orthonormal wavelets from the Daubechies family. The extrapolation approach has been combined with the *à trous* wavelet transform from the Bi-orthogonal Spline family, providing an efficient wavelet tool to analyze data, capable to avoid Gibb's phenomenon in the data boundary vicinities and expand the region of confidence and applicability of the transform. Analysis from data sets made with known functions show the quality of the wavelet extrapolation in terms of data precision and the perfect amalgam between the two wavelet families. An iterative *à trous* coarsening algorithm was then proposed, where an iterative undecimated wavelet transform is used in conjunction with the wavelet extrapolation procedure to determine the continuum of simulated featureless noisy spectra of stars. In comparison with other boundary treatments, the wavelet extrapolation has proven to be a robust and reliable alternative, independent of noise level, decomposition level and continuum shape near boundaries. Relative errors were found to be in the order of 0.2 per cent or less for the entire set

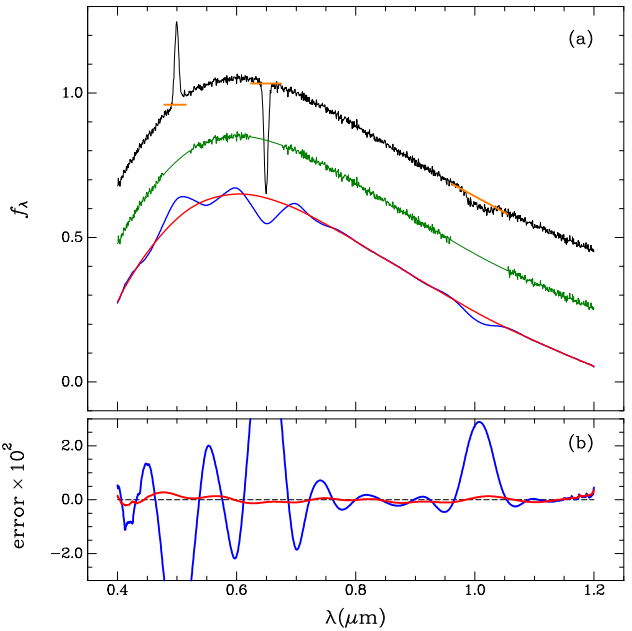

Figure 6. Continuum results for a simulated spectrum with noise and features. Panel (a): the input data (black curve) from Example 4 (Sect. 4, $T_{\text{eff}} = 4830$ K case) with added gaussian noise (SNR = 200), two gaussian profiled features, at 0.50 μm and 0.65 μm, with relative intensity 0.3 and -0.4 and a shallow wide band constituted by 10 Gaussian profiles with relative intensity -0.02 spread evenly from 0.985 μm to 1.030 μm. All Gaussian profiles have FWHM = 0.001 μm. The continua obtained using Algorithm 1 ($p = 3$, $\eta = 6$, $tol = 0.001$) and wavelet extrapolation extension with and without prior removal of features are shown respectively by the red and blue curves. The orange line segments display the initial local continuum approximation used for each feature when considering feature removal. The green curve shows the input data with the final continuum approximation for each feature (noiseless segments; see text for more details). All curves have been arbitrarily moved up or down for a better visualization. Panel (b): the corresponding errors (difference) between the true and the obtained continuum shown in panel (a).

of points of each spectrum. In the case of spectra with features, numerical simulations have shown that one can take advantage of the interpolatory properties of the wavelet transform in an iterative algorithm to determine local continuum approximations without the need of model fitting and feature removal, greatly simplifying data treatment due to the presence of strong features and/or wide bands. Although not discussed in the text, the techniques presented in this work can be applied to two-dimension data sets (images) straightforwardly.

Acknowledgments

The authors would like to thank the Brazilian supporting agencies CNPq (grants 304854/2009-3, 476447/2010-0, 201457/2010-5) and FAPERGS (grants 1017481 and PG 1873-25.51/13-0). Numerical calculations were performed at LANA (CCNE, UFSM, Brazil).

References

[1] Albert Bijaoui and Frédéric Rué. A multiscale vision model adapted to the astronomical images. *Signal Process*, 46(3):345–362, October 1995.

[2] W. Cai and M. Adjouadi. Boundary artifact minimization on best matching blocks in wavelet-based video compression. *WSEAS Trans. on Comp.*, 3:1361–1366, 2004.

[3] C. K. Chui. *An Introduction to Wavelets*. Wavelet Analysis and its Applications. Academic Press, first edition, Jan 1992.

[4] A. Cohen, Ingrid Daubechies, and J.-C. Feauveau. Biorthogonal bases of compactly supported wavelets. *Commun. on Pure and Appl. Math.*, 45(5):485–560, 1992.

[5] Albert Cohen, Ingrid Daubechies, and Pierre Vial. Wavelets on the interval and fast wavelet transforms. *Appl. and Comp. Harmon. Anal.*, 1(1):54–81, December 1993.

[6] I. Daubechies. Where do wavelets come from? a personal point of view. *Proc. of the IEEE*, 84(4):510–513, Apr 1996.

[7] M. Feil and A. Uhl. Real-time image analysis using mimd parallel a trous wavelet algorithms. *Real-Time Imaging*, 7(6):483–493, 2001.

[8] A. Grossmann and J. Morlet. Decomposition of hardy functions into square integrable wavelets of constant shape. *SIAM J. on Math. Anal.*, 15(4):723–736, 1984.

[9] M. Holschneider, R. Kronland-Martinet, J. Morlet, and Ph. Tchamitchian. A real-time algorithm for signal analysis with the help of the wavelet transform. In Jean-Michel Combes, Alexander Grossmann, and Philippe Tchamitchian, editors, *Wavelets, inverse problems and theoretical imaging*, pages 286–297. Springer Berlin Heidelberg, 1990.

[10] Norden E. Huang, Zheng Shen, Steven R. Long, Manli C. Wu, Hsing H. Shih, Quanan Zheng, Nai-Chyuan Yen, Chi Chao Tung, and Henry H. Liu. The empirical mode decomposition and the hilbert spectrum for nonlinear and non-stationary time series analysis. *Proc. of the R. Soc. of Lond. A: Math., Phys. and Eng. Sci.*, 454(1971):903–995, 1998.

[11] Alice Kozakevicius and Alex A. Schmidt. Wavelet transform with special boundary treatment for 1d data. *Comput. and Appl. Math.*, 32(3):447–457, 2013.

[12] Alice J. Kozakevicius, C. R. Rodrigues, R. C. Nunes, and R. G. Filho. Adaptive ecg filtering and *qrs* detection using orthogonal wavelet transform. *Biomedical Engineering*, 3(458):1–5, 2005.

[13] R. Kronland-Martinet, J. Morlet, and A. Grossmann. Analisys of sound patterns through wavelet transforms. *Int. J. of Pattern Recognit. and Artif. Intell.*, 1(2):273–302, 1987.

[14] Andrew Laine, Iztok Koren, Wuhai Yang, and Fred Taylor. A steerable dyadic wavelet transform and interval wavelets for enhancement of digital mammography. In *Wavelet Applications II, H. H. Szu, Editor*, volume 2491, pages 736–749. SPIE, 1995.

[15] Wei Siong Lee and A.A. Kassim. Signal and image approximation using interval wavelet transform. *IEEE Trans. on Image Proc.*, 16(1):46–56, Jan 2007.

[16] Cuiwei Li, Chongxun Zheng, and Changfeng Tai. Detection of ecg characteristic points using wavelet transforms. *IEEE Trans. on Biomed. Eng.*, 42(1):21–28, Jan 1995.

[17] S.G. Mallat. A theory for multiresolution signal decomposition: the wavelet representation. *IEEE Trans. on Pattern Anal. and Mach. Intell.*, 11(7):674–693, Jul 1989.

[18] Boaz Ophir, Michael Lustig, and Michael Elad. Multi-scale dictionary learning using wavelets. *IEEE Journal of Selected Topics in Signal Processing*, 5(5):1045–1057, 2011.

[19] Miriam Primbs. New stable biorthogonal spline-wavelets on the interval. *Results. Math.*, 57:121–162, 2010.

[20] Ron Rubinstein, Alfred M. Bruckstein, and Michael Elad. Dictionaries for sparse representation modeling. *Proceedings of the IEEE*, 98(6):1045–1057, 2010.

[21] Limin Shao and Peter R. Griffiths. Automatic baseline correction by wavelet transform for quantitative open-path fourier transform infrared spectroscopy. *Environ. Sci. & Tech.*, 41(20):7054–7059, 2007.

[22] Chen Shao-hui, Hongbo Su, Zhang Renhua, and Tian Jing. Fusing remote sensing images using à trous wavelet transform and empirical mode decomposition. *Pattern Recognit. Lett.*, 29:330–342, 2008.

[23] Y.U. Sheng-Sheng, H. Xiao-cheng, Z. Jing-li, and C. Jia-zhong. The boundary processing of wavelet based image compression. *Wuhan Univ. J. of Nat. Sci.*, 3:296–302, 2004.

[24] M. Shensa. The discrete wavelet transform: wedding the a trous and mallat algorithms. *IEEE Trans. on Signal Process.*, 40(10):2464–2482, Oct 1992.

[25] Zhuoer Shi, Donald J. Kouri, G.W. Wei, and David K. Hoffman. Generalized symmetric interpolating wavelets. *Comput. Phys. Commun.*, 119(2-3):194 – 218, 1999.

[26] Priyanka Singh, Priti Singh, and Rakesh Kumar Sharma. Jpeg image compression based on biorthogonal, coiflets and daubechies wavelet families. *Int. J. of Computer Appl.*, 13(1):1–7, January 2011.

[27] J. Starck and F. Murtagh. *Astronomical Image and Data Analysis*. Astronomy and Astrophysics Library. Springer-Verlag Berlin Heidelberg, second edition, 2006.

[28] J. L. Starck, D. L. Donoho, and E. J. Candès. Astronomical image representation by the curvelet transform. *Astron. & Astrophys.*, 398(2):785–800, 2003.

[29] J.-L. Starck, Y. Moudden, P. Abrial, and M. Nguyen. Wavelets, ridgelets and curvelets on the sphere. *Astron. & Astrophys.*, 446(3):1191–1204, 2006.

[30] Jean-Luc Starck, Fionn Murtagii, and Albert Bijaoui. Multiresolution support applied to image filtering and restoration. *Graph. Models and Image Proc.*, 57(5):420 – 431, 1995.

[31] Jean-Luc Starck, R. Siebenmorgen, and R. Gredel. Spectral analysis using the wavelet transform. *The Astrophys. J.*, 482(2):1011–1020, 1997.

[32] H. Su, Q. Liu, and J. Li. Boundary effects reduction in wavelet transform for time-frequency analysis. *WSEAS Trans. on Signal Process.*, 8(4):169–179, 2012.

[33] Wim Sweldens. The lifting scheme: A custom-design construction of biorthogonal wavelets. *Appl. and Comp. Harmon. Anal.*, 3(2):186 – 200, 1996.

[34] Sofia Tapani and Alice Kozakevicius. Wavelet change-point analysis for non-stationary time series. *Journal of Wavelet Theory and Applications*, 5(1):22–44, 2012.

[35] John R. Williams and Kevin Amaratunga. A discrete wavelet transform without edge effects using wavelet extrapolation. *J. of Fourier Anal. and Appl.*, 3(4):435–449, 1997.

In: Wavelets: Principles, Analysis and Applications ISBN: 978-1-53613-374-5
Editor: Joseph Burgess

Chapter 6

WAVELETS IN PROCESSING OF NEUROPHYSIOLOGICAL DATA RELATED TO AMBIGUOUS IMAGES PERCEPTION

***A. N. Pisarchik*[1,2], *A. N. Pavlov*[1,*], *A. E. Hramov*[1], *V. A. Maksimenko*[1], *A. E. Runnova*[1] *and M. O. Zhuravlev*[1]**
[1]Yuri Gagarin State Technical University of Saratov, Russia
[2]Center for Biomedical Technology,
Technical University of Madrid, Spain

Abstract

Noninvasive brain research is extensively used in modern neuroscience for studying human cognitive behavior and intellection mechanisms. One of the important technologies for recording brain dynamics is the electroencephalography (EEG). This method is very convenient for monitoring brain activity in a wide frequency range with a relatively high spatial resolution. The EEG data of psychophysiological experiments are usually processed for detecting characteristic patterns associated with various cognitive functions, as well as for other types of brain activity. In this chapter, we show that the wavelet transform has several advantages and benefits over classical methods of spectral analysis and other approaches.

We demonstrate the success of wavelet processing on the example of psychophysiological data registered in the experiment with visual perception of ambiguous objects. Nowadays, ambiguous images are extensively

*Corresponding Author Email: pavlov.lesha@gmail.com.

explored for studying visual perception and decision making [1, 2, 3]. However, despite high efforts of many researchers, the main mechanisms of image interpretation are not yet well understood. Although it is known that perception is a result of nonlinear processes in a distributed neural network of occipital, periental and frontal regions of brain cortex [4, 5], further detailed investigation of these processes is required.

PACS: 87.85.D-, 87.19, 42.66.Si

Keywords: brain, EEG, data processing, wavelet

AMS Subject Classification: 92F, 92C, 68W, 42C40, 65T60

Introduction

The brain is likely the most convoluted and enigmatic object for comprehensive studies attracting the burning interest of the broad scientific community [6, 7, 8, 9, 10, 11]. Nowadays, the brain is the subject of intensive research of diverse areas of science and technology, including neurophysiology, medicine, physics, engineering, mathematics, and nonlinear dynamics. The multidisciplinary approach providing insight into the brain mystery and a deeper understanding of mechanisms underlying its dynamics, opens promising opportunities for humanity in medicine and neurotechnology in the near future. Different types of complex brain dynamics are resulted from many kinds of cognitive activity, such as the formation of memory traces [12, 13], information processing [14, 15], spatial orientation [16, 17], intelligence [18, 19], etc. Due to their great importance, different brain activities were the research subject of many scientists [12, 13, 14, 15, 16, 17, 18, 19]. Modern studies of cognitive processes are usually based on the analysis of the brain dynamics using neurophysiological data noninvasively recorded by electroencephalography (EEG) and magnetoencephalography (MEG).

The registration of a large number of experimental data requires qualitative and automated processing. Today, neuroscience uses a variety of mathematical methods for the analysis of experimental data representing brain activity, based on modern approaches of nonlinear physics, radiophysics and mathematics, such as spectral analysis, time-frequency analysis, various modifications of wavelet and bi-coherent wavelet analyses [6], Hilbert-Huang transform [20, 21], statistical analysis, linear and nonlinear correlation analyses [22, 23].

The processing based on the wavelet analysis has advantages and benefits in comparison with classical spectral approaches and other methods. To demonstrate the wavelet methods efficiency, we focus on the problem of ambiguous images perception. These objects were extensively explored because they are good models for studying cognitive brain functions and decision-making processes [1, 2, 3]. However, despite high interest of many researchers, the main mechanisms of image interpretation are not yet well understood. Nowadays, it is only known that perception is the result of nonlinear processes taking place in the distributed neural network of occipital, parietal and frontal regions of brain cortex [4, 5]. However, which of the brain processes are responsible for perception decision-making still remains unknown.

Along with fundamental significance, the solution of the problem under consideration has clear practical application. From this point of view, the proposed approach is aimed on the development of methods for studying different measurable brain activity recordings (EEG, MEG, and diffusive tensor visualization) with accompany cognitive processes of ambiguous images interpretation under objective and subjective factors influence. Clarification of regularities and understanding of ambiguous images perception mechanisms can be applied to the development of test software for studying adaptation capabilities and stress tolerance, i.e., preservation of personal working properties in the presence of external stimuli. This software type can find application in training and testing high-class specialists of various professions, where specific personal characteristics, like attention, monotonous process of concentration in the presence of external disturbances, fast response and fast adaptation ability to stress are important. Traditionally, examples of such professional niches are pilots, police, special forces as well as more rare professions in politics, intelligence, etc.

Furthermore, a study of the mechanisms of cognitive activity arbitrary regulation in the presence of stress factors is one of the perspective trends in applied sciences. It is established that the ability disturbance in controlling cognitive activity at stress situations is one of the main causes of cognitive and behavioral malfunctions, typical for persons with emotional disorders [24, 25], alcohol and drug addiction [26], feeding behavior disorders [27, 28], and other types of neuropsychic disorders. Therefore, understanding of the mechanisms underlying cognitive regulation dysfunctions plays a key role in the development of new branches of diagnostics, treatments, and prevention of neuro-psychical diseases.

For a better understanding of the wavelet processing capabilities, we provide a brief description of our experiment work on data recording during the perception of an ambiguous image. In our experiments, we used the Necker cube [29] (Fig. 1), the popular object of many psychological experiments [30, 31, 32, 33, 34, 35] and theoretical models [32, 36, 37]. This ambiguous image is a 2D geometric figure which looks as a cube with transparent faces and visible ribs. An observer without any perception abnormalities sees the Necker cube as a 3D-object due to the specific position of the cube's ribs. Bistability in perception consists in the interpretation of this image as to be either left-oriented or right-oriented depending on the contrast of different inner ribs. The contrast $I \in [0,1]$ of three middle lines centered in the left middle corner is used as a control parameter. The values $I = 1$ and $I = 0$ correspond, respectively, to 0 (black) and 255 (white) pixels' luminance of the middle lines. Therefore, we can define a contrast parameter as $I = y/255$, where y is the brightness level of the middle lines using the 8-bit grayscale palette.

Experiment Description

Forty healthy subjects, males and females, between 20 and 30 years old with normal visual acuity participated in the experiments. All of them provided informed written consent before their participation in the experiment. The experimental studies were performed in accordance with the Declaration of Helsinki and approved by the Local Research Ethics Committee of the Yuri Gagarin State Technical University of Saratov.

The most ambiguous image is the cube with equally contrast inner ribs, i.e., with $I = 0.5$. While observing the most ambiguous image (central cube in Fig. 1) for a prolonged time, the mean duration of a particular interpretation of the cube orientation (left or right) is known to vary from one second to several minutes depending on the observer and stimulus conditions (see, e.g. [38]), whereas the mean response time is rather consistent and varied only by a few hundred milliseconds (see, e.g. [39]). In order to fix the first impression of the person and avoid switches between two possible percepts, we presented the Necker cube images with different wireframe contrasts (as those shown in Fig. 1) for short time intervals, each lasting between 1.0 and 1.5 seconds. Such short durations of the stimuli presentation were chosen to reduce the stabilization effect [40, 41], because the probability of the image interpretation,

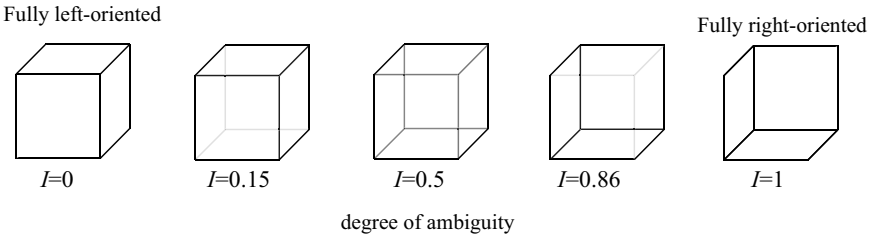

Figure 1. Examples of Necker cube images. The ambiguity of the Necker cube is controlled by contrast parameter I. The left-hand image with $I = 0$ corresponds to the fully left-oriented cube, whereas the right-hand image with $I = 1$ to the fully right-oriented cube. The middle image with $I = 0.5$ has the highest ambiguity.

persisting until the subsequent presentation, strongly depends on the duration of the previously observed image. There was a high probability for a perceptual configuration to persist to the next stimulus presentation only when it was seen consistently for a relatively long time until the stimulus disappeared. For the Necker cube, the required time of the consistent observation is known to be about 1 second [40, 41]. Although the "memory" effect cannot be completely avoided, it can be significantly diminished by making the length of the stimulus exhibition ν shorter than 1.5 seconds. Moreover, a random variation of the control parameter I also prevents the perception stabilization. Lastly, to draw away the observer's attention and make the perception of the next Necker cube independent of the previous one, different abstract pictures were exhibited for about $\eta = 5.0 - 5.5$ seconds between subsequent demonstrations of the Necker cube images.

All participants were instructed to press either the left or right key depending on their first impression about the cube orientation at each presentation. The whole experiment lasted around 45–50 minutes for each participant, including short recordings of the brain background activity before and after the stimuli presentation. During experimental sessions, the cubes with different I were randomly presented (each configuration for about 100 times) and the electrical brain activity was recorded using the EEG recorder Encephalan–EEGR–19/26 ("Medikom MTD", Taganrog, Russia) with a two–button input device. The recorder provided simultaneous registration of neurophysiological data from 19 – 31 EEG channels. The monopolar registration method and the classical ten-

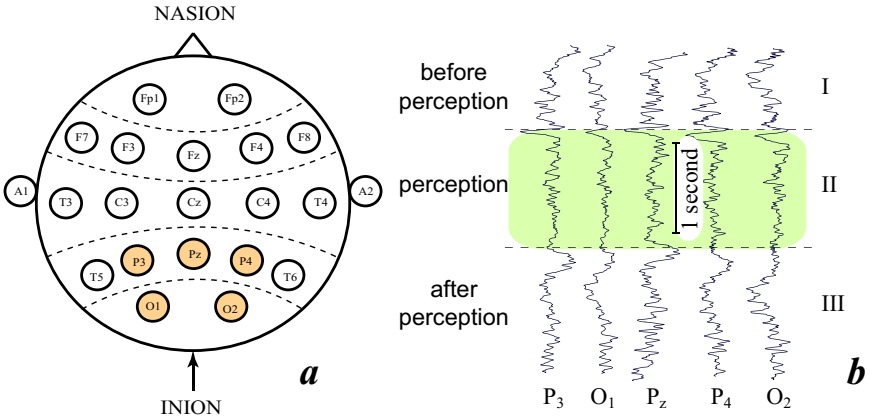

Figure 2. ***a*** Scheme of electrodes' positions and ***b*** typical set of registered EEG traces. Different segments of the EEG recording are named I, II, III, which correspond, respectively, to a 1-sec time interval preceding the cube presentation (*before perception*), $\sim$ 1-sec interval during the cube observation (*perception*), and 1-sec interval after the cube observation (*after perception*).

twenty electrode system were used (see Fig. 2 ***a***). The gray-scale images were demonstrated on the 24" BenQ LCD monitor with resolution of 1920×1080 pixels and a 60-Hz refresh rate. The subject was located at a 70–80-cm distance from the monitor with an approximately 0.25-rad visual angle.

Wavelet Processing of EEG Data

Wavelet Approaches to Estimation of Wave Components Dynamics of EEG Signals

In order to process EEG signals, we focused on the channels in the projection zone of primary and secondary visual analyzers, where, as is commonly assumed [4, 5, 42, 43], visual stimulus perception is concentrated. We analyzed the EEG signals recorded by five electrodes (O_1, O_2, P_3, P_4, P_z) placed on standard positions of the ten-twenty international system [44], using continuous wavelet transformation. In Fig. 2 ***a*** these electrodes are highlighted. The wavelet energy spectrum $E^n(f,t) = \sqrt{W_n(f,t)^2}$ was calculated for each EEG channel $X_n(t)$ in the frequency range $f \in [1,45]$ Hz. Here, $W_n(f,t)$ is the

complex-valued wavelet coefficients calculated as [6]

$$W_n(f,t) = \sqrt{f} \int_{t-4/f}^{t+4/f} X_n(t)\psi^*(f,t)dt, \tag{1}$$

where $n = 1,...,N$ is the EEG channel number ($N = 5$ being the total number of occipital channels used for the analysis) and "$*$" defines the complex conjugation. The mother wavelet function $\psi(f,t)$ is the Morlet wavelet, often used for the analysis of neurophysiological data, defined as [45, 6, 46]

$$\psi(f,t) = \sqrt{f}\pi^{-1/4} e^{j\omega_0 f(t-t_0)} e^{-f(t-t_0)^2/2}, \tag{2}$$

where $\omega_0 = 2\pi$ is the wavelet parameter.

We estimated the value of frequency $f_{max}(t)$ corresponding to the maximum energy in the wavelet spectrum using Eq. (1), at every time moment. The whole experimental series were split into number N_{tr} 3-sec trials associated with perception of each individual stimulus. Each trial consisted of three subsequent segments: (I) before image presentation, (II) during presentation, and (III) after presentation, as illustrated in Fig 2 ***b***. Then, every trial was split into $N_{\delta_t} = 15$ time intervals of $\delta_t = 0.2$ sec long, and its power spectrum was split into $N_{\delta_f} = 15$ bands of $\delta_f = 0.2$ Hz width each. For the considered time-frequency plane ($t \in [0,3]$ s, $f \in [1,40]$ Hz) the distribution of frequency f_{max} corresponding to the maximum energy was calculated as follows

$$L(f,t) = \sum_{N_{tr}} \sum_{N_{\Delta_t}} \sum_{N_{\Delta_f}} \gamma, \gamma = \begin{cases} 1, & f_{max}(t) \in \delta f \quad \wedge \quad t \in \delta t \\ 0, & \text{otherwise.} \end{cases} \tag{3}$$

In order to quantitatively characterize the distribution $L(f,t)$ for each participant, the ratios $L^I_\alpha / L^{II}_\alpha$ and L^I_β / L^{II}_β were calculated as

$$L^{I,II}_{\alpha,\beta} = \int_{\Delta t_{I,II}} \int_{\Delta f_{\alpha,\beta}} L(f',t')df'dt', \tag{4}$$

where $\Delta f_{\alpha,\beta}$ is the range of alpha and beta activities and $\Delta t_{I,II}$ is the duration of segments I and II.

Depending on the values $L^I_\alpha / L^{II}_\alpha$ and L^I_β / L^{II}_β two different scenarios were identified. The first scenario (**Sc. 1**) was characterized by a significant decrease

in the alpha energy during the segment II (perception) with a simultaneous relatively high increase in the beta energy. The second scenario (**Sc. 2**) was distinguished by a strong contribution of alpha-rhythm and much lower pronounced generation of beta-rhythm during all segments. A more detailed analysis of the spectral properties associated with the first and second scenarios was performed for three frequency bands: $\Delta f_\delta = [1-4]$ Hz (δ-rhythm), $\Delta f_\alpha = [8-12]$ Hz (α-rhythm), and $\Delta f_\beta = [20-30]$ Hz (β-rhythm), corresponding to typical patterns of the human cognitive activity. The EEG power spectrum was characterized by the location of the dominant (most pronounced) spectral components. In particular, the first (maximal) spectral component in the n-th EEG channel occurred at frequency $f_1^n(t)$ at which the global maximum $E^n(f_1^n(t),t)$ took place. Respectively, the second, third, ..., M-th spectral components appeared at frequencies $f^n_{2,\ldots,M}(t)$, where $E^n(f^n_{2,\ldots,M}(t),t)$ exhibited subsequent local maxima.

Using the values $f^n_{2,\ldots,M}(t)$ the EEG spectral properties were characterized by spectral coefficients $F^n_{\alpha,\beta,\delta}(t)$ calculated for each channel at every time moment

$$F^n_{\alpha,\beta,\delta}(t) = \sum_{j=1}^{M} \Theta^n_{\alpha,\beta,\delta}(j,t), \quad \Theta^n_{\alpha,\beta,\delta}(j,t) = \begin{cases} 1/j, & \text{if} \quad f_j^n \in \Delta f_{\alpha,\beta,\delta}, \\ 0, & \text{if} \quad f_j^n \notin \Delta f_{\alpha,\beta,\delta}. \end{cases} \tag{5}$$

The obtained spectral coefficients $F^n_{\alpha,\beta,\delta}(t)$ were averaged over all channels and time intervals for each segment (I, II, III) as follows

$$\langle F_{\alpha,\beta,\delta}\rangle_{\Delta t_{\mathrm{I,II,III}}} = \frac{1}{N}\sum_{n=1}^{N} \int\limits_{\Delta t_{\mathrm{I,II,III}}} F^n_{\alpha,\beta,\delta}(t')dt'. \tag{6}$$

Then, for every subject the values of $\langle F_{\alpha,\beta,\delta}\rangle_{\Delta t_{\mathrm{I,II,III}}}$ were averaged over $K = 400$ trials associated with individual perceptions:

$$\langle \overline{F}_{\alpha,\beta,\delta}\rangle_{\Delta t_{\mathrm{I,II,III}}} = \frac{1}{K}\sum_{i=1}^{K} \langle F_{\alpha,\beta,\delta}\rangle_{\Delta t^i_{\mathrm{I,II,III}}}, \tag{7}$$

where Δt^i_{I}, Δt^i_{II}, $\Delta t^i_{\mathrm{III}}$ are the time intervals of segments I, II, III, associated with the i-th perception event and $\overline{F}$ defines the averaging over all presentations. Finally, the coefficients defined by Eq. (7) were averaged over the subjects demonstrated **Sc. 1** and **Sc. 2** scenarios, as follows

$$|\langle \overline{F}_{\alpha,\beta,\delta}\rangle_{\Delta t_{\mathrm{I,II,III}}}|_{Sc.1,2} = \frac{1}{N_{Sc.1,2}}\sum_{N_{Sc.1,2}} \langle \overline{F}_{\alpha,\beta,\delta}\rangle_{\Delta t_{\mathrm{I,II,III}}}, \tag{8}$$

where $N_{Sc.1}$ and $N_{Sc.2}$ are the number of participants with prevailing scenario **Sc. 1** or **Sc. 2**, respectively.

Multifractal Formalism for EEG Signals

Besides the discussed time-frequency analysis of experimental data which includes investigations of rhythmic contributions of EEG signals, the continuous wavelet-transform represents a preliminary processing stage within more complicated algorithms, such as the multifractal formalism, revisited with wavelets [47, 48]. Although other approaches to estimate the singularity spectrum have been successfully applied in earlier studies [49], the wavelet-transform modulus maxima (WTMM) method proposed by Muzy et al. [47] is a more universal approach. Its advantages consist in the possibility to characterize both large and small fluctuations in complex signals (the structure-function method [49] does not allow analysis of weak singularities) and the ability to ignore slow nonstationarity (a polynomial trend) typically presented in physiological processes of different origin.

To simplify further characterization of singularities in terms of the Hölder exponents, the continuous wavelet-transform is written as follows

$$W_n(s,t) = \frac{1}{s}\int_{-\infty}^{\infty} F_n(u)\psi\left(\frac{t-u}{s}\right)du, \tag{9}$$

where s is the analyzed time scale, $F_n(u)$ is the distribution function of the EEG signal $X_n(t)$, and ψ is a real valued wavelet function. A particular feature of the considered analysis is that the estimated singularity spectrum does not depend on the basic wavelets (theoretically, if we do not take into account a finite length of time series and finite precision of data recording). In practice, one typically deals with wavelets constructed on the base of derivatives of the Gaussian function, among which the MHAT-function

$$\psi(t) = (1-t^2)\exp\left(-\frac{t^2}{2}\right), \tag{10}$$

one of the most widely used wavelets. It represents the second derivative of the Gaussian function and possesses two vanishing moments, although wavelets with $m > 2$ vanishing moments can be selected while considering singularities in higher derivatives of the distribution function. In particular, when $F_n(u)$ represents a sum of a regular part $P_n^k(u-t^*)$ obtained by the expansion of the

distribution function into the Taylor series up to degree k around singularity point t^*, and an irregular part described by the Hölder exponent h as

$$F_n(u) = P_n^k(u-t^*) + C|u-t^*|^h, \tag{11}$$

then the first part will be ignored for $m > k$, and the Hölder exponent is estimated using the equation

$$W(s,t^*) = C\int_{-\infty}^{\infty} \psi(u)|su|^{h(t^*)}du \sim s^{h(t^*)}. \tag{12}$$

Although this equation enables us to compute $h(t^*)$, such approach is feasible due to interferences produced by nearby singularities. Muzy et al. [47, 48] proposed a robust method which uses partition functions. It includes extraction of skeleton $L(s)$ of the wavelet-transform, i.e., all lines of local maxima and minima, and the construction of functions

$$Z(q,s) = \sum_{l\in L(s)} |W(s,t_l(s))|^q \sim s^{\tau(q)}, \tag{13}$$

where $t_l(s)$ denotes the position of the local maximum (or minimum) at line l.

The scaling exponents $\tau(q)$ are computed from the power-law dependence of $Z(q,s)$ versus q. The Legendre transform is then applied to estimate singularity spectrum $D(h)$

$$D(h) = qh(q) - \tau(q) \tag{14}$$

and Hölder exponents $h(q)$

$$h(q) = \frac{d\tau(q)}{dq}. \tag{15}$$

The singularity spectrum quantifies the Hausdorff dimension D of data subsets with different Hölder exponents h. The most frequently occurred singularity $h(0)$ associated with $q = 0$ is characterized by the largest D-value. The Hausdorff dimension takes smaller values for seldom singularities related to large fluctuations ($q > 0$) and small fluctuations ($q < 0$), and the singularity spectrum decreases up to zero when h is far from the mean value $h(0)$.

The shape of $D(h)$-spectrum is often used to compare complex organization of physiological signals related to different organism's states [50, 51, 52].

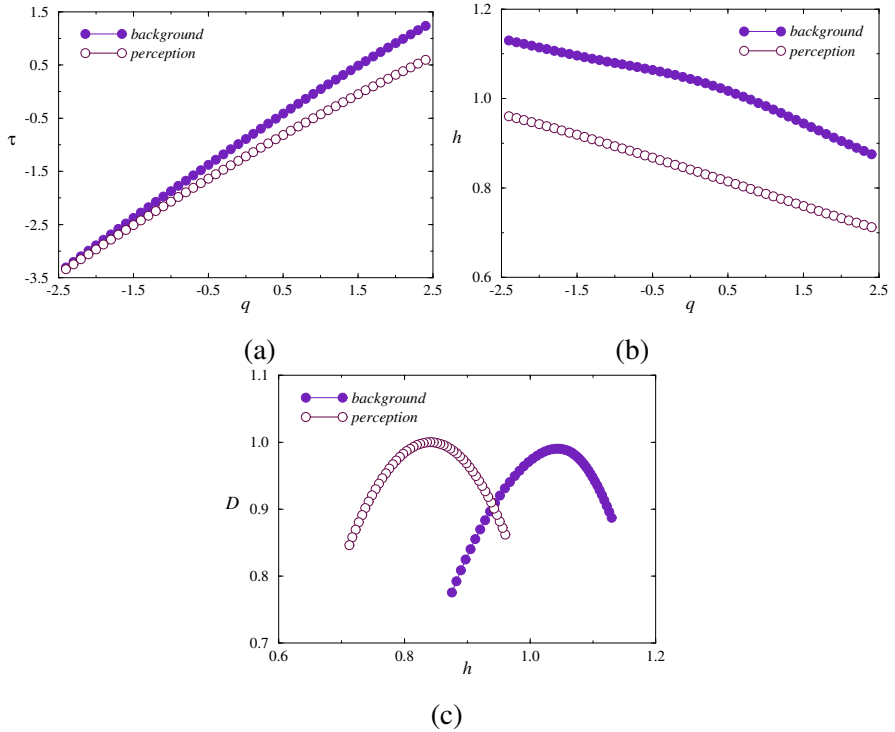

Figure 3. Typical changes in multiscale properties of EEG signals observed during the cube observation. (a) Spectrum of scaling exponents $\tau(q)$, (b) Hölder exponents $h(q)$, and (c) singularity spectrum. Here, the recording from the P4-channel is considered.

Nevertheless, few numerical measures characterizing this shape need to be introduced for diagnostic-related studies. Among measures which quantify the $D(h)$-spectrum geometry, its position $h(0)$ and width $\beta = h_{max} - h_{min}$ are the most important quantifies. The position of the singularity spectrum along the h-axis characterizes correlation features of experimental data and has a relation to scaling exponents quantifying the decay of the correlation function or the spectral power. The width of $D(h)$ reflects the degree of inhomogeneity of complex processes and is used as a complexity measure. Thus, the singularity spectrum consisting of a single point is associated with monofractal processes (e.g., $1/f$-

noise) being simpler as compared with multifractal processes that require many quantities to describe scaling features for different data subsets. It should be noted that these quantities can be computed independently on the degree of stationarity; this circumstance is an advantage of the WTMM method over many standard techniques for data processing.

Results and Discussion

The perception of an ambiguous image is associated with an increase in the electrical neuronal activity in the occipital lobe [53, 54]. Therefore, in the present work we analyze the EEG recordings from five channels (P_3, O_1, P_z, P_4, and O_2) taken from the occipital lobe according to the scheme shown in Fig 2 ***a***.

In order to study the perception process, the EEG signals corresponding to each image presentation were partitioned into three segments: I, II, and III, as shown in Fig 2 ***b***. Segment I represents the EEG during the time interval preceding the cube presentation. Segment II corresponds to the time interval during the cube presentation until the observer presses a button on the joystick. Finally, segment III starts immediately after the subject presses the button and lasts for about 1 second. All EEG recordings were processed using the continuous wavelet transformation with the Morle wavelet function (for details see section "EEG analysis"). The wavelet power spectra were calculated for each segment in the frequency band $\Delta f \in [1, 40]$ Hz.

The wavelet analysis of the time-frequency EEG space showed that the perception of ambiguous images can follow two different scenarios depending on the relationship between α-, β-, and δ-rhythms dynamics. In order to reveal selection criteria for one or another scenario, we analyzed the EEG data separately for each subject and found that all perception trials can be classified into two groups of events with distinct spectral relationships, referred to as type-1 and type-2 events, belonging to the first (**Sc. 1**) and second (**Sc. 2**) scenarios, respectively.

In the experimental data, the location of the spectral component corresponding to the maximal value of the wavelet energy was estimated for every segment (I, II, III) and averaged over the whole session. Similar to the method of the event-related potential [55], the 3-sec traces of EEG (the structure of the trace is shown in Fig 2 ***b***) were extracted from the whole recording. For each trace the coefficient describing the location of the maximal spectral component was calculated by Eq. (3). The obtained dependencies calculated for each segment were

then lined up in time and averaged to diminish any brain activity unrelated to the stimulus. As a result, for each subject the dependence $L(f,t)$ reflecting the dynamics of the main spectral component induced by the stimulus perception was obtained. In order to quantitatively characterize the obtained 2-D dependencies $L(f,t)$, the coefficients L^I_α/L^{II}_α and L^I_β/L^{II}_β describing the variation of the spectral properties in alpha and beta bands during visual perception were calculated by Eq. (4).

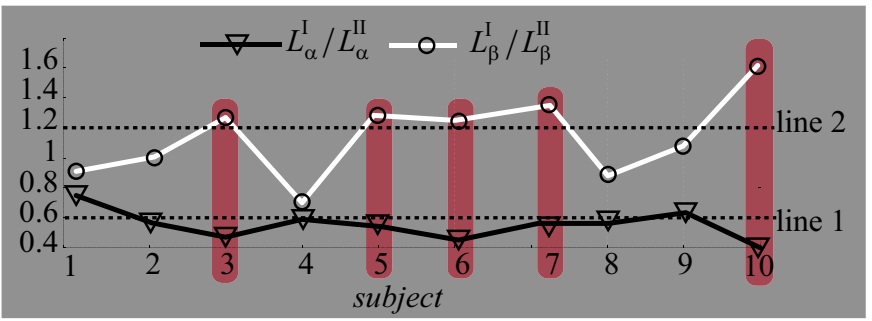

Figure 4. ***a*** Values of L^I_α/L^{II}_α (triangles) and L^I_β/L^{II}_β (circles) illustrating the relation between the power of alpha and beta waves in intervals I and II obtained by the statistical analysis of the 40-min experimental session of 10 subjects from all 40 participants in the experiment. The horizontal dashed lines indicate threshold values defining a $> 40\%$ decrease in alpha-activity (line 1) and a $> 20\%$ increase in beta-activity (line 2) used to identify different perception scenarios **Sc. 1** and **Sc. 2**. The red (gray) boxes highlight subjects 3, 5, 6, 7, and 10 which followed the first scenario **Sc. 1**. Other subjects were associated with the second scenario **Sc. 2**.

In Fig. 4 we plot the coefficients L^I_α/L^{II}_α and L^I_β/L^{II}_β by circles and triangles, respectively, for the group of 10 subjects. Having analyzed the obtained values, we found that the subjects can be divided into two groups, according to two different scenarios of the perception process. Each subject was classified into one or another group based on a set of threshold values (dashed lines in Fig. 2) defined by a $> 40\%$ decrease in alpha activity (line 1) and a $> 20\%$ increase in beta activity (line 2). The solid red boxes in Fig. 4 highlight five subjects (3, 5, 6, 7 and 10) for which L^I_α/L^{II}_α and L^I_β/L^{II}_β satisfy the threshold values. These subjects were associated with the first scenario, while other subjects belonged to the second scenario. In the studies based on wavelet analysis, we have identified

two different scenarios of brain activity in the perception of ambiguous images (Necker cubes) for all participants.

Thus, simultaneous singularity spectra obtained by the multifractal analysis enable separation between the background EEG and the EEG signals acquired during the cube observation (*perception*). A typical example is illustrated in Fig. 3. According to Fig. 3a, the analyzed signal is characterized by a multiscale structure, because the dependence of scaling exponents $\tau(q)$ is a nonlinear function and its slope varies depending on the parameter q, i.e., on the considered range of scales. The latter is illustrated in Fig. 3b, where the Hölder exponents $h(q)$ being the local slopes of the function $\tau(q)$ are shown. The perception process is characterized by reduced values of $h(q)$ as compared with the background activity, i.e., by changes in correlation properties of the EEG data during the cube observation. Changes in the complexity measure β are insignificant and comparable with variations in the characteristics for repeated cube observations by the same subject. Figure 1c confirms that the singularity spectrum is translated along the h-axis, but its width does not change. This illustrative example reflects main features of the perception process consisting in the reduced Hölder exponents. This effect may be interpreted as a transition to a less "smooth" signal, in which the probability of alternation between the large and small values increases.

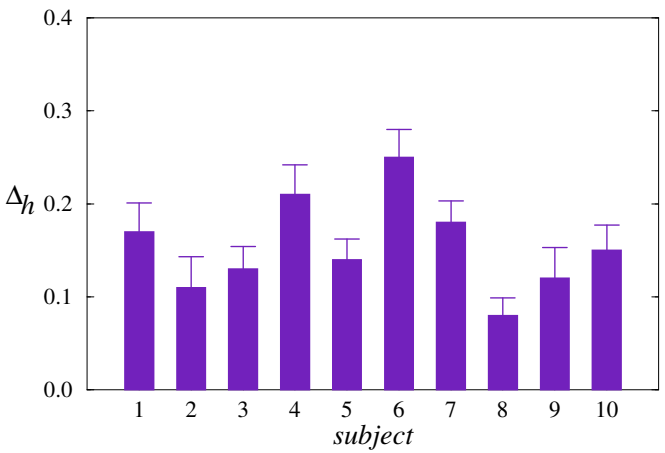

Figure 5. Statistical analysis of distinctions in EEG signals during background activity and cube observation.

Figure 5 provides the results of the performed statistical analysis. Here, we show the difference $\Delta_h = h_{backgroud}(0) - h_{perception}(0)$. The authentic separation between the perception process and the background electrical activity of the brain is confirmed, although the revealed translation of the singularity spectrum varies among subjects and, moreover, among different cube observations by the same subject. Due to this fact, the appropriate selection of the EEG channel is important to improve the characterization of the perception process.

Conclusion

The use of wavelet methods for processing experimental and model neurophysiological data is very promising for further development of neuroscience. This chapter has introduced the reader into the time-frequency analysis of brain activity signals and showed recent results on a study of their structure and complexity. Our experimental research on the perception of ambiguous objects have demonstrated the progress in wavelet mathematics for the EEG data analysis. In particular, the conducted studies allowed us to reliably distinguish the periods of the perception of the stimulus object and the background state of passive wake with open eyes. The use of the continuous wavelet transform made possible to divide all subjects into two groups demonstrating different scenarios of brain dynamics in the perception process.

The success of the wavelet methods for the analysis of neurophysiological data provides great optimism for the prospects in the application of the wavelet approaches to the development of diagnostic systems and analysis of human EEG behavior, as well as similar recordings of cerebral brain activity. In addition, the achievements of modern computational algorithmization suggest an early possibility of full wavelet real-time signal processing, which will allow the active use of wavelet approaches to develop systems based on a brain-computer interface.

Acknowledgment

This work has been supported by the Russian Science Foundation (grant 16-12-10100).

References

[1] Leopold D. A., Logothetis N. K. Multistable phenomena: changing views in perception. *Trends in Cognitive Sciences*. 1999; 3(7):254–264.

[2] Long G. M., Toppino T. C. Enduring interest in perceptual ambiguity: alternating views of reversible figures. *Psychological Bulletin*. 2004; 130(5):748–768.

[3] Kornmeier J., Hein C. M., Bach M. Multistable perception: When bottom-up and top-down coincide. *Brain and Cognition.* 2009; 69(1):138–147.

[4] Tong F., Meng M., Blake R. Neural bases of binocular rivalry. *Trends in Cognitive Sciences.* 2006; 10(11):502–511.

[5] Sterzer P., Kleinschmidt A., Rees G. The neural bases of multistable perception. *Trends in Cognitive Sciences*. 2009; 13(7):310–318.

[6] Hramov A. E., Koronovskii A. A., Makarov V. A., Pavlov A. N., Sitnikova E. *Wavelets in Neuroscience.* Springer Series in Synergetics. Springer, Heidelberg, New York, Dordrecht, London; 2015.

[7] Bear M. F., Connors B. W., Paradiso M. A. *Neuroscience. Exploring the brain.* Woters Kluwer; 2015.

[8] Chavez M., Valencia M., Navarro V., Latora V., Martinerie J. Functional Modularity of Background Activities in Normal and Epileptic Brain Networks. *Physical Review Letters.* 2010;104:118701.

[9] Bick C., Rabinovich M.I. Dynamical origin of the effective storage capacity in the brain's working memory. *Physical Review Letters.* 2009; 103:218101.

[10] Wolf F. Symmetry, multistability, and long-range interactions in brain development. *Physical Review Letters.* 2005; 95:208701.

[11] van Luijtelaar E. L. J. M., Hramov A. E., Sitnikova E. Y., Koronovskii A. A. Spikewave discharges in WAG/Rij rats are preceded by delta and theta precursor activity in cortex and thalamus. *Clinical Neurophysiology.* 2011; 122:687–695.

[12] Spuler M. A high-speed brain-computer interface (BCI) using dry EEG electrodes. *PLOS ONE.* 2017; 12(2): 1–12. doi:10.1371/journal.pone.0172400.

[13] Bowsher K., Civillico E. F., Coburn J., Collinger J., Contreras-Vidal J. L., Denison T., et al. Brain-computer interface devices for patients with paralysis and amputation: a meeting report. *Journal of Neural Engineering*. 2016; 13(2):023001.

[14] Chen X., Wang Y., Nakanishi M., Gao X., Jung T. P., Gao S. High-speed spelling with a noninvasive brain-computer interface. *Proceedings of the National Academy of Sciences.* 2015;112(44):E6058–E6067. doi:10.1073/pnas.1508080112.

[15] Palmeri T. J., Gauthier I. Visual object understanding. *Nat Rev Neurosci.* 2004; 5:291–303.

[16] Sargolini F., Fyhn M., Hafting T., McNaughton B. L., Witter M. P., Moser M. B., et al. Conjunctive representation of position, direction and velocity in entorhinal cortex. *Science.* 2006; 312:754–758.

[17] Wolpaw J. R., McFarland D. J. Control of a two-dimensional movement signal by a noninvasive brain-computer interface in humans. *Proceedings of the National Academy of Sciences of the United States of America.* 2004;101(51):17849–17854. doi:10.1073/pnas.0403504101.

[18] Birbaumer N., Ghanayim N., Hinterberger T., Iversen I., Kotchoubey B., Kübler A., et al. A spelling device for the paralysed. *Nature*. 1999; 398: 297 – 298.

[19] Ma T., Li H., Deng L., Yang H., Lv X., Li P., et al. The hybrid BCI system for movement control by combining motor imagery and moving onset visual evoked potential. *Journal of Neural Engineering.* 2017; 14(2): 026015.

[20] Huang N. E., Shen Z., Long S. R., Wu M. C., Shih H. H., Zheng Q., et al. The empirical mode decomposition and the Hilbert spectrum for nonlinear and non-stationary time series analysis. *Proc R Soc London Ser A.* 1998;454:903–995.

[21] Pavlov A. N., Filatova A. E., Hramov A. E. Digital filtering and time-and-frequency analysis of nonstationary signals on the basis of wavelets and empirical modes. *Journal of Communications Technology and Electronics.* 2011; 56(9):1098–1104.

[22] Sitnikova E., Van Luijtelaar E. L. Cortical and thalamic coherence during spike-wave seizures in WAG/Rij rats. *Epilepsy Res.* 2006; 71:159–180.

[23] Westmijse I., Ossenblok P., Gunning B., Luijtelaar van G. Onset and propagation of spike and slow wave discharges in human absence epilepsy: A MEG study. *Epilepsia*. 2009; 50:2538.

[24] Williams J. M., Watts F. N., MacLeod C., Mathews A. *Cognitive psychology and emotional disorder.* Chichester, England: Wiley; 1997.

[25] Clark D. A., Beck A. T. Cognitive theory and therapy of anxiety and depression: Convergence with neurobiological findings. *Trends in Cognitive Science.* 2010; 14:418–424.

[26] Robinson T. E., Berridge K. C. Addiction. *Annual Review of Psychology.* 2003; 54(1):25–53. doi:10.1146/annurev.psych.54.101601.145237.

[27] McManus F., Waller G., Chadwick P. Biases in the processing of different forms of threat in bulimic and comparison women. *Journal of Nervous and Mental Disease.* 1996; 184:547–554.

[28] Trincas R., Bilotta E., Mancini F. Specific beliefs about emotions are associated with different emotion-regulation strategies. *Psychology.* 2016; 7(13):25–53. doi:10.4236/psych.2016.713159.

[29] Necker L. A. Observations on some remarkable optical phenomena seen in Switzerland; and on an optical phenomenon which occurs on viewing a figure of a crystal or geometrical solid. *The London, Edinburgh, and Dublin Philosophical Magazine and Journal of Science.* 1832; 1(5):329–337. doi:10.1080/14786443208647909.

[30] Mathes B., Struber D., Stadler M.A., Basar-Eroglu C. Voluntary control of Necker cube reversals modulates the EEG delta- and gamma-band response. *Neuroscience letters.* 2006; 402(1-2):145149. doi:10.1016/j.neulet.2006.03.063.

[31] Jurgen K., Miriam P., Michael B. Necker cube: Stimulus-related (low-level) and percept-related (high-level) EEG signatures early in occipital cortex. *Journal of Vision*. 2011; 11(9):12.

[32] Pisarchik A. N., Jaimes-Reátegui R., Magallón-García C. D. A., Castillo-Morales C. O. Critical slowing down and noise-induced intermittency in bistable perception: bifurcation analysis. *Biological Cybernetics*. 2014; 108(4):397–404. doi:10.1007/s00422-014-0607-5.

[33] Runnova A. E., Hramov A. E., Grubov V., Koronovsky A. A., Kurovskaya M. K., Pisarchik A. N. Theoretical background and experimental measurements of human brain noise intensity in perception of ambiguous images. *Chaos, Solitons & Fractals*. 2016; 93:201–206.

[34] Grubov V. V., Runnova A. E., Zhuravlev M. O., Maksimenko V. A., Pchelintseva S. V., Pisarchik A. N. Perception of multistable images: EEG studies. *Cybernetics And Physics*. 2017; (6):108–113.

[35] Hramov A. E., Maksimenko V. A., Pchelintseva S. V., Runnova A. E., Grubov V. V., Musatov V. Y., et al. Classifying the perceptual interpretations of a bistable image using EEG and artificial neural networks. *Frontiers in Neuroscience*. 2017; 11:674. doi:10.3389/fnins.2017.00674.

[36] Pisarchik A. N., Bashkirtseva I. A., Ryashko L. B. Controlling bistability in a stochastic perception model. *The European Physical Journal Special Topics*. 2015; 224(8):1477–1484. doi:10.1140/epjst/e2015-02473-0.

[37] Pisarchik A. N., Bashkirtseva I., Ryashko L. Stochastic sensitivity of a bistable energy model for visual perception. *Indian Journal of Physics*. 2017; 91(1):57–62. doi:10.1007/s12648-016-0881-2.

[38] Pastukhov A., Garcia-Rodriguez P. E., Haenicke J., Guillamon A., Deco G., Braun J. Multi-stable perception balances stability and sensitivity. *Frontiers in Computational Neuroscience*. 2013; 7:17.

[39] Carpenter R. H. S. Analysing the detail of saccadic reaction time distributions. *Biocybernetics and Biomedical Engineering*. 2012; 32(2):49–63.

[40] Merk I., Schnakenberg J. A stochastic model of multistable visual perception. *Biological Cybernetics*. 2002; 86:111–116.

[41] Leopold D. A., Wilke M., Maier A., Logothetis N. K. Stable perception of visually ambiguous patterns. *Nature Neuroscience*. 2002; 5(6):605–609.

[42] Kornmeier J., Bach M. The Necker cube – an ambiguous figure disambiguated in early visual processing. *Vision Research.* 2005; 45(8):955–960.

[43] Grossberg S., Swaminathan G. A laminar cortical model for 3D perception of slanted and curved surfaces and of 2D images: development, attention and bistability. *Vision Research.* 2004; 44:1147–1187.

[44] Niedermeyer E., da Silva F. L. *Electroencephalography: Basic Principles, Clinical Applications, and Related Fields, Nonlinear Dynamics.* Lippincot Williams & Wilkins; 2014.

[45] Grossman A., Morlet J. Decomposition of Hardy function into square integrable wavelets of constant shape. *SIAM J Math Anal.* 1984; 15(4):273.

[46] Ferrante A., Gavriel C., A. F. Data-efficient hand motor imagery decoding in EEG-BCI by using Morlet wavelets & common spatial pattern algorithms. *Neural Engineering (NER), 7th International IEEE/EMBS Conference*, 2015;948.

[47] Muzy J. F., Bacry E., Arneodo A. Wavelets and multifractal formalism for singular signals: Application to turbulence data. *Phys Rev Lett.* 1991; (67):3515–3518.

[48] Muzy J. F., Bacry E., Arneodo A. The multifractal formalism revisited with wavelets. *International Journal Bifurcation Chaos.* 2010; 4(2):245–302.

[49] Frish U., Parisi G. *Fully developed turbulence and intermittency.* Ghil M., Benzi R., Parisi G., editors. Amsterdam: North-Holland; 1985.

[50] Ivanov P. C., Amaral L. A. N., Goldberger A. L., Havlin S., Rosenblum M. G., Struzik Z. R., et al. Multifractality in human heartbeat dynamics. *Phys Rev Lett.* 1999; (399):461–465.

[51] Pavlov A. N., Sosnovtseva O. V., Ziganshin A. R., Holstein-Rathlou N. H., Mosekilde E. Multiscality in the dynamics of coupled chaotic systems. *Physica A*. 2002; 316:233–249.

[52] Pavlov A. N., Semyachkina-Glushkovskaya O. V., Lychagov V. V., Abdurashitov A. S., Pavlova O. N., Sindeeva O. A., et al. Multifractal characterization of cerebrovascular dynamics in newborn rats. *Chaos, Solitons and Fractals*. 2015; (77):6–10.

[53] Mulckhuyse M., Kelley T. A., Theeuwes J., Walsh V., Lavie N. Enhanced visual perception with occipital transcranial magnetic stimulation. *Eur J Neurosci.* 2011; 34(8):1320–1325.

[54] Gleiss S., Kayser C. Acoustic noise improves visual perception and modulates occipital oscillatory states. *Journal of Cognitive Neuroscience.* 2014; 26(4):699–711.

[55] Eimer M. Sensory gating as a mechanism for visuospatial orienting: electrophysiological evidence from trial-by-trial cutting experiments. *Percept Psychophys.* 1994; (55):667–675.

INDEX

A

à trous transform, 91, 92, 94, 97, 99, 103, 107, 110, 111, 113, 116, 117
adaptive filtering process, 92
amalgam, 119
amplitude, 3, 5, 70
anomalies, 56, 63, 71, 81
application(s), vii, viii, ix, x, 1, 2, 9, 16, 18, 19, 21, 22, 23, 24, 27, 29, 31, 35, 39, 44, 46, 50, 52, 55, 75, 76, 77, 78, 79, 81, 82, 83, 85, 87, 88, 89, 90, 91, 92, 93, 94, 98, 100, 113, 121, 122, 124, 125, 127, 139, 144

B

bandwidth, 11, 61
benefits, vii, x, 92, 125, 127
beta wave, 137
brain, x, 125, 126, 127, 129, 136, 137, 139, 140, 141, 143
brain activity, x, 125, 126, 127, 129, 136, 137, 139

C

circulation, 71, 76
classical methods, vii, x, 125
climate, vii, viii, ix, 19, 55, 56, 57, 58, 59, 62, 70, 71, 73
climate change, vii, viii, 55, 56
climatic data, 56
cognitive activity, 126, 127, 132
cognitive function, x, 125
cognitive process, 127
complexity, 23, 30, 31, 34, 37, 38, 39, 40, 41, 43, 49, 135, 138, 139
composition, 31, 34, 35, 38, 39, 41, 42, 47, 48, 49
compression, 4, 22, 23, 24, 28, 30, 31, 44, 45, 46, 50, 121, 123, 124
computation, 25, 26, 28, 29, 31, 32, 34, 46, 52, 60
conjugation, 79, 131
construction, 23, 93, 94, 98, 99, 100, 101, 110, 113, 119, 124, 134
continuous WT (CWT), 17, 57, 59, 61, 63, 66, 67, 68, 69, 71, 72, 78, 79
correlation, 7, 17, 58, 70, 74, 79, 80, 85, 86, 88, 89, 126, 135, 138
correlation analysis, 17, 74, 85
correlation coefficient, 79
correlation function, 135
cortex, x, 126, 127, 140, 142
cycles, 56, 67

D

data analysis, 18, 73, 87, 92, 94, 95, 98, 139
data processing, 126, 136
data set, ix, 44, 59, 61, 63, 73, 91, 97, 98, 104, 105, 106, 107, 109, 110, 111, 114, 121
data-driven analysis, vii, ix, 91, 92
decomposition, ix, 17, 18, 23, 31, 32, 33, 34, 35, 36, 37, 38, 39, 40, 41, 42, 43, 45, 47, 48, 49, 50, 51, 52, 61, 83, 84, 91, 93,

94, 95, 96, 97, 98, 99, 106, 110, 111, 112, 113, 116, 117, 119, 121, 122, 123, 141
degenerate, 25, 28
denoising, ix, 51, 54, 77, 83
derivatives, 98, 133
detection, 57, 60, 74, 75, 87, 88, 122
dilation, 9, 79
discharges, 140, 142
discrete data, 95, 103, 107
distortions, ix, 92, 99
distribution function, 103, 107, 108, 133, 134

E

ECG, 45, 113, 117
electrodes, 130, 140
electroencephalography (EEG), x, 125, 126, 127, 129, 130, 131, 132, 133, 135, 136, 138, 139, 140, 142, 143, 144
electromagnetic fields, 18, 89
emission, 95, 113, 114
emotional disorder, 127, 142
energy, 58, 78, 79, 82, 94, 103, 104, 107, 108, 109, 114, 115, 118, 130, 131, 132, 136, 143
energy density, 78, 82
entorhinal cortex, 141
equilibrium, 11, 17
error analysis, 22, 47, 52
ethylene oxide, 75, 89, 90
event-related potential, 136
evoked potential, 141
evolution, viii, 1, 10, 11, 16, 79, 81
execution, 30, 41, 43, 46
extraction, 76, 88, 94, 134
extreme precipitation, 75
extreme weather events, 56

F

filters, 31, 32, 33, 34, 35, 38, 39, 41, 54, 61, 92, 93, 94, 96, 97, 98, 99, 110, 111, 113, 116, 118
fluctuations, 133, 134
force, 11, 13, 118
Fourier analysis, 4, 57
Fourier transform, vii, viii, 1, 3, 4, 7, 8, 19, 57, 58, 78, 92, 93, 98, 123
frequency resolution, 9
FTIR, 17, 74, 88
function values, 96, 100, 118

G

galaxies, 92, 104
global warming, 70

H

Haar Wavelet Transform, vii, 22, 30
Hausdorff dimension, 134
hydrologic regime, 56

I

image analysis, 122
image interpretation, x, 126, 127, 129
image(s), viii, x, 22, 23, 27, 28, 45, 46, 51, 53, 77, 80, 83, 87, 92, 94, 121, 122, 123, 124, 125, 126, 127, 128, 129, 131, 136, 137, 143, 144
interface, 139, 140, 141
interval arithmetics, 22, 24, 30

L

laminar, 144
light, vii, ix, 77, 86, 89, 114, 115
light scattering, 89
localization, 3, 57, 61
lysozyme, 82

M

magnetoencephalography (MEG), 126, 127, 142
mass, vii, viii, 1, 3, 11, 13, 15, 16, 17, 73, 88
matrix, 27, 29, 35, 36, 37, 38, 42, 43, 47, 49, 50, 70, 73, 79, 102, 110
measurements, 13, 49, 50, 143
metric spaces, 26

models, 56, 73, 75, 117, 127, 128
modifications, 126
modulus, 14, 45, 133
motivation, 23, 26
multifractal formalism, 133, 144

N

neural network, x, 127, 143
neurophysiology, 126
neuroscience, x, 125, 126, 139
nonlinear dynamics, 126
normalization constant, 103
numerical computations, 24

O

oligomers, 75, 90
operations, 25, 26, 32, 33, 34, 36, 37, 38, 39, 40, 41, 43, 47
oscillation, 10, 11, 12, 13, 14, 15, 16, 80, 81

P

partial differential equations, 51
periodicity, 67, 70, 71, 93
physics, vii, 2, 17, 126
physics education, 1, 2
Planck constant, 103
polymer, 17, 74
polynomial functions, 111
precipitation, ix, 55, 57, 60, 71, 73, 74, 87
probability, 129, 138
propagation, 18, 19, 22, 142
proteins, 18, 89

Q

QRS complex, 117

R

rainfall, 73, 74, 87
reconstruction, 28, 34, 52, 92
regression analysis, 19
remote sensing, 123
researchers, x, 126, 127
residue(s), 112, 113, 118, 119
resolution, x, 3, 9, 18, 32, 34, 40, 75, 76, 90, 92, 97, 100, 105, 118, 125, 129
response, 76, 127, 129, 142
response time, 129

S

scaling, 3, 9, 32, 34, 39, 61, 92, 93, 95, 97, 99, 100, 101, 102, 103, 108, 109, 111, 117, 118, 134, 135, 136, 138
scaling coefficients, 32, 34, 100, 117, 118
scattering, vii, ix, 18, 74, 76, 77, 86, 90
sensor, 13, 15
serum albumin, 88
shape, ix, 57, 58, 91, 116, 117, 121, 122, 134, 135, 144
signals, vii, viii, 1, 2, 3, 7, 9, 23, 45, 55, 57, 59, 60, 61, 79, 83, 96, 117, 130, 133, 134, 135, 136, 138, 139, 141, 144
signal-to-noise ratio, 114, 116, 118, 119
simulation(s), ix, 24, 71, 73, 76, 91, 92, 119, 121
smoothing, 83, 113
smoothness, 61, 83, 111
solution, 12, 14, 18, 22, 31, 89, 103, 127
spectra analysis, 80, 86
spectral component, 16, 132, 136, 137
spectroscopy, 78, 85, 86, 123
speed of light, 103
standard deviation, 46
stars, 94, 104, 121
state(s), 71, 72, 134, 139, 145
stimulus, 129, 131, 137, 139
stimulus perception, 137
stochastic model, 143
stress factors, 127
structure, 88, 92, 94, 100, 133, 136, 138, 139
synthesis, 6, 23, 92

T

techniques, vii, ix, 2, 23, 24, 30, 45, 57, 77, 78, 81, 86, 95, 113, 117, 121, 136
technology(ies), x, 53, 125, 126

temperature, vii, viii, ix, 55, 56, 57, 60, 61, 63, 65, 66, 70, 71, 73, 82, 85, 103, 109
thermal analysis, 18, 74, 90
time series, ix, 55, 57, 58, 59, 60, 61, 70, 71, 76, 90, 122, 124, 133, 141
time signals, 79, 80
transformation(s), 23, 31, 34, 35, 38, 41, 46, 93, 94, 96, 97, 99, 100, 130, 136
translation, 9, 39, 79, 139
treatment, 78, 113, 118, 121, 122
trends, viii, ix, 55, 56, 57, 59, 61, 70, 71, 73, 75, 77, 87, 88, 94, 112, 127, 139, 140, 142

V

vector, 29, 31, 32, 33, 39, 40, 41, 47, 84, 95, 96, 97, 112
visual processing, 144
visual stimulus, 130
visualization, 73, 104, 120, 127

W

wavelet amplitude, 79
wavelet analysis, vii, viii, 1, 17, 18, 55, 56, 57, 58, 60, 61, 70, 73, 74, 75, 78, 87, 88, 93, 127, 136, 137
wavelet extrapolation, vii, ix, 91, 92, 95, 112, 115, 119, 120, 121, 124
wavelet transform, vii, viii, ix, x, 1, 3, 18, 21, 22, 23, 30, 51, 52, 55, 56, 57, 58, 61, 70, 73, 75, 76, 77, 78, 82, 83, 87, 88, 90, 91, 92, 93, 94, 95, 96, 97, 98, 99, 100, 104, 110, 111, 116, 117, 118, 119, 121, 122, 123, 124, 125, 130, 136, 139
WT cross correlation, 79